Modelling of methane and hydrogen enriched methane flames in industrial gas turbine burners

Moell, Daniel

2018

Document Version:
Publisher's PDF, also known as Version of record

Modelling of methane and hydrogen enriched methane flames in industrial gas turbine burners

by Daniel Moëll

LUND
UNIVERSITY

Thesis for the degree of Doctor in Philosophy
Thesis advisors: Prof. Xue-Song Bai, Dr. Daniel Lörstad
Faculty opponent: Dr. Laurent Gicquel, CERFACS, France

To be presented, with the permission of the Faculty of Engineering of Lund University, for public criticism in the lecture hall M:B, M-building, Ole Römers väg 1, Lund at the Department of Energy Sciences on Monday, the 10th of September 2018 at 10:00.

Organization
LUND UNIVERSITY
Department of Energy Sciences
Box 118
SE–221 00 LUND
Sweden

Document name
DOCTORAL DISSERTATION
Date of disputation
2018-09-10
Sponsoring organization
Siemens Industrial Turbomachinery AB and the swedish research council (VR)

Author(s)
Daniel Moëll

Title and subtitle
Modelling of methane and hydrogen enriched methane flames in industrial gas turbine burners

Abstract
The majority of the power production in the world today is based on combustion of coal, oil and natural gas. Most countries have agreed that the amount of CO_2 emitted to the atmosphere will have to be decreased to keep the global warming at sustainable levels. One way of reducing the CO_2 emitted to the atmosphere is by introducing hydrogen co-firing. The hydrogen may be produced from renewable sources and can be used when the solar and wind power are not producing electricity. Another way of reducing the emitted CO_2 is to increase the gas turbine efficiency. The two best ways of increasing the efficiency is to increase the turbine inlet temperature and to reduce the cooling air usage. There are also increasing demands on decreasing emissions toxic to humans, such as nitric oxides (NO_x) and carbon monoxide (CO). The NO_x emissions are increasing exponentially with the firing temperature. To reduce the NO_x emissions lean premixed combustion is used in most modern industrial gas turbines. The gas turbine is operated close to the lean blow out limit, sometimes with stability issues as a result. To keep the NO_x and CO emissions to a minimum and at the same time increase the hydrogen addition and the firing temperature while reducing the cooling air usage, accurate predictive tools are required to give good estimates of the flame shape and position, the wall heat load close to the flame, the turbine inlet temperature profile and if possible the combustion dynamics and emission performance.

This thesis aims to explore the usage of scale resolving turbulence models combined with flamelet based combustion models using both methane and hydrogen enriched methane. The main focus areas are predictions of mean flame shape and position as well as flame dynamics. The burner studied is the Siemens 3^{rd} generation DLE burner. Both scale adaptive simulations (SAS) and large eddy simulations (LES) are applied where stationary flamelets combined with a fractal combustion model is used in the SAS case and flamelet generated manifolds integrated across presumed PDFs are used in the LES case. The simulation results are compared against measurement data including OH-PLIF, dynamic pressure and static pressure drop. The usage of non-scale resolving methods show that the flame location is unaffected by adjusting the combustion model constant, which directly affects the mean reaction rate, making them unsuitable for predictions of flame movements due to different fuels. Both scale resolved methods applied here does a good job in predicting the change in flame shape and location when introducing hydrogen enrichment. The SAS-fractal reaction rate model constants had to be adjusted to get the flame position similar to the measurement data whereas no adjustments were made in the LES-FGM case. The shape of the PDF for the reaction progress variable is investigated in the LES-FGM case with only minor differences in flame shape and position as a result.The combustion dynamics is fairly well predicted using the SAS-fractal model but excellent agreement with measurement data is only achieved using the LES-FGM model.

Key words
Large eddy simulation, Gas turbine combustion, Thermoacoustics, Flamelet generated manifolds, Hydrogen enriched combustion

Classification system and/or index terms (if any)

Supplementary bibliographical information

Language
English

ISSN and key title

ISBN
978-91-7753-746-5 (print)
978-91-7753-747-2 (pdf)

Recipient's notes

Number of pages
106

Price

Security classification

Modelling of methane and hydrogen enriched methane flames in industrial gas turbine burners

by Daniel Moëll

LUND
UNIVERSITY

Cover illustration front: Instantaneous flame in Siemens 3^{rd} generation DLE burner from simulation by Daniel Moëll.

Funding information: The thesis work was financially supported by Siemens Industrial Turbomachinery AB and the Swedish research council (VR).

Faculty of Engineering, Department of Energy Sciences

ISBN: 978-91-7753-746-5 (print)
ISBN: 978-91-7753-747-2 (pdf)
ISSN: <ISSN number>

Printed in Sweden by Media-Tryck, Lund University, Lund 2018

Dedicated to my family

Populärvetenskaplig sammanfattning

I dagsläget står förbränning av kol, olja och gas för en majoritet av all elproduktion i världen. En oundviklig slutprodukt vid eldning av kolbaserade bränslen är koldioxid (CO2). De flesta av världens ledare är överens om att utsläppen av koldioxid behöver minskas kraftigt för att minimera uppvärmningen av jorden, vilken redan ligger på kritiska nivåer. Även om de förnyelsebara källorna till energi är ökande så räcker de inte till för att tillfredsställa världens energibehov, utan förbränning av fossila bränslen kommer att vara en del av världsbilden många år framåt. Ett stort problem med vind och solkraft är att elproduktionen endast är aktiv när det blåser eller när solen skiner, vilket gör att behovet av att lagra energi är stort. Ett sätt att lagra energi är att producera vätgas när elproduktionen är hög, vilken sedan gradvis kan spädas in i naturgasnäten och på så sätt minska åtgången av naturgas och därmed mängden koldioxid i avgaserna, alternativt ersätta naturgasen helt. Ett annat sätt att minska klimatpåverkan är att öka verkningsgraden på elproduktionen. För att omvandla den lagrade energin i t.ex. naturgas och vätgas till mekanisk eller elektrisk energi kan man använda gasturbiner. Det mest effektiva sättet att öka verkningsgraden i en gasturbin är att temperaturen in till turbindelen och därmed även eldningstemperaturen höjs så mycket som möjligt. Både ökad eldningstemperatur och ökad vätgashalt i naturgasen kräver modifieringar av befintliga gasturbiner där noggranna beräkningsmodeller behöver tas fram för att minimera felkällorna.

Förutom utsläppen av koldioxid kan förbränning leda till utsläpp av ämnen som är direkt skadliga för närmiljön, till exempel kolmonoxid (CO), som är giftig för människor och kväveoxider (NOx) som har starkt negativa effekter för luftvägarna, och bidrar till smog och försurning. Kolmonoxid är ofta ett resultat av ofullständig förbränning och kan oftast hanteras i gasturbiner genom att se till så att förbränningsverkningsgraden är hög. Kväveoxiderna är starkt kopplade till förbränningstemperaturen, där den maximala förbränningstemperaturen uppnås vid så kallade stoichiometriska förhållanden, det vill säga, både all syre i luften och allt bränsle förbrukas. Det primära sättet att undvika hög produktion av kväveoxider i moderna gasturbiner är att använda förblandad förbränning med ett överskott på luft, så kallad mager förbränning. Förbränningstemperaturen kan då med fördel hållas så nära turbininloppstemperaturen som möjligt. En nackdel med mager, förblandad förbränning är att oönskad förbränningsdynamik kan uppstå då värmeutvecklingen i flamman inte är tillräcklig för att bibehålla stabiliteten. Förbränningsdynamik kan ge upphov till självsvängningar i bärande strukturer i gasturbinen, vilket kan leda till haveri inom väldigt korta tidsperioder. Både utsläppen av skadliga ämnen och nivån på förbränningsdynamiken påverkas starkt av bränslet som används i gasturbinen. För att hantera och prediktera förbrän-

ningsdynamik och effekter av olika bränslen krävs noggranna mätmetoder och pålitliga beräkningsmetoder.

Den här avhandlingen syftar till att utvärdera beräkningsmodeller som är både tillräckligt noggranna för att resultaten ska vara relevanta och tillräckligt billiga för att metoden ska vara användbar inom industrin. Matematiska modeller används där både luft- och bränsleflödet genom gasturbinens brännkammare beskrivs tillsammans med kemin som ligger till grund för förbränningen av luft och bränsle. Olika modeller för turbulens utvärderas tillsammans med modeller för kemin där den inre strukturen för en flamma antas vara förutbestämd. Turbulens beskrivs oftast som en kaskad av olika skalor där de största turbulenta skalorna är av samma storleksordning som geometrin och de minsta skalorna kan vara många storleksordningar mindre, beroende på balansen mellan konvektiva och viskösa krafter i flödet. Här används så kallade skalupplösande turbulensmodeller, där de största skalorna som har mest rörelseenergi tas med direkt i modellerna och de mindre skalorna tas med genom statistiska samband. Beräkningsmetodiken appliceras på industriella hårdvaror och utvärderas mot experimentellt framtagen data. När metodiken har utvärderats och uppvisat tillräcklig noggrannhet används den för att studera förbränningsdynamik samt påverkan på förbränningen av vätgasinblandning i naturgasen.

Den här avhandlingen ger en utökad insikt i hur förbränningsstabiliseringen i det turbulenta flödet ser ut i en av Siemens gasturbinbrännare. Flammans interaktion med virvelstrukturer i flödet har utforskats och kartlagts. Effekten av vätgasinspädning i naturgas visar att flamman blir mer kompakt och flyttar sig närmare brännarhårdvaran, vilket stämmer väl överens med experimentell mätdata. Metodiken kan därmed användas för att undersöka och utvärdera driftfall och hårdvaror där mätdata inte är tillgängligt. Avhandlingen visar även att det är möjligt att prediktera kopplingar mellan flöde, flamma och akustik med hjälp av modeller där de kemiska reaktionerna endast är statistiskt beskrivna, vilket leder till stora tidsbesparingar för gasturbinutvecklare.

Abstract

The majority of the power production in the world today is based on combustion of coal, oil and natural gas. Most countries have agreed that the amount of CO_2 emitted to the atmosphere will have to be decreased to keep the global warming at sustainable levels. One way of reducing the CO_2 emitted to the atmosphere is by introducing hydrogen co-firing. The hydrogen may be produced from renewable sources and can be used when the solar and wind power are not producing electricity. Another way of reducing the emitted CO_2 is to increase the gas turbine efficiency. The two best ways of increasing the efficiency is to increase the turbine inlet temperature and to reduce the cooling air usage. There are also increasing demands on decreasing emissions toxic to humans, such as nitric oxides (NO_x) and carbon monoxide (CO). The NO_x emissions are increasing exponentially with the firing temperature. To reduce the NO_x emissions lean premixed combustion is used in most modern industrial gas turbines. The gas turbine is operated close to the lean blow out limit, sometimes with stability issues as a result. To keep the NO_x and CO emissions to a minimum and at the same time increase the hydrogen addition and the firing temperature while reducing the cooling air usage, accurate predictive tools are required to give good estimates of the flame shape and position, the wall heat load close to the flame, the turbine inlet temperature profile and if possible the combustion dynamics and emission performance.

This thesis aims to explore the usage of scale resolving turbulence models combined with flamelet based combustion models using both methane and hydrogen enriched methane. The main focus areas are predictions of mean flame shape and position as well as flame dynamics. The burner studied is the Siemens 3^{rd} generation DLE burner. Both scale adaptive simulations (SAS) and large eddy simulations (LES) are applied where stationary flamelets combined with a fractal combustion model is used in the SAS case and flamelet generated manifolds integrated across presumed PDFs are used in the LES case. The simulation results are compared against measurement data including OH-PLIF, dynamic pressure and static pressure drop. The usage of non-scale resolving methods show that the flame location is unaffected by adjusting the combustion model constant, which directly affects the mean reaction rate, making them unsuitable for predictions of flame movements due to different fuels. Both scale resolved methods applied here does a good job in predicting the change in flame shape and location when introducing hydrogen enrichment. The SAS-fractal reaction rate model constants had to be adjusted to get the flame position similar to the measurement data whereas no adjustments were made in the LES-FGM case. The shape of the PDF for the reaction progress variable is investigated in the LES-FGM case with only minor differences in flame shape and position as a result.The combustion dynamics is fairly well

predicted using the SAS-fractal model but excellent agreement with measurement data is only achieved using the LES-FGM model.

List of publications

I. **D. Moëll**, D. Lörstad and X. S. Bai. Numerical investigation of hydrogen enriched natural gas in the SGT-800 burner. *In GT2015-44040, ASME Turbo Expo*, (2015)

II. **D. Moëll**, D. Lörstad and X. S. Bai. Numerical investigation of methane/hydrogen/air partially premixed flames in the SGT-800 burner fitted to an atmospheric rig. *Flow, Turbulence and Combustion*, 96, (2016), 987-1003

III. **D. Moëll**, D. Lörstad, A. Lindholm, D. Christensen and X. S. Bai. Numerical and experimental investigation of the Siemens SGT-800 burner fitted to a water rig. *In GT2017-64129, ASME Turbo Expo*, (2017)

IV. **D. Moëll**, D. Lörstad and X. S. Bai. LES of hydrogen enriched methane/air combustion in the SGT-800 burner at real engine conditions. *In GT2018-67434, ASME Turbo Expo*, (2018)

V. **D. Moëll**, A. Lantz, K. Bengtsson, D. Lörstad, A. Lindholm and X. S. Bai. Large eddy simulation and experimental analysis of combustion dynamics in a gas turbine burner. *Submitted to Journal of Engineering for Gas Turbines and Power*, (2018)

Related work

I. **D. Moëll**, D. Lörstad and X. S. Bai. Large eddy simulation of a gas turbine burner fitted to an atmospheric test rig. *Nordic flame days*, Stockholm, Sweden (2017)

II. **D. Moëll**, A. Lantz, D. Lörstad, A. Lindholm and X. S. Bai. Large eddy simulation and experimental study of hydrogen enrichment in a swirl stabilized gas turbine burner. *Manuscript in preparation* (2018)

Acknowledgements

This work was carried out at the division of Fluid Mechanics at the department of Energy Sciences, Lund University, Sweden. The work was sponsored by Vetenskaps Radet (VR) and Siemens industrial turbomachinery AB.

First of all I would like to thank my Academic supervisor Prof. Xue-Song Bai and my industrial supervisor Dr. Daniel Lörstad for guiding me through this work. Thank you for all valuable discussions and ideas through out this work.

I would also like to thank my managers Hanna Sivervik and Anders Häggmark at Siemens for giving me the opportunity to start this work and their patience for me to finish it. Also thanks to Dr. Jenny Larfeldt for continuous support and encouragement through out the project.

All of my colleagues at Siemens and at Lund are greatly acknowledged for providing a nice working environment. Thank you, it would not have been as fun without you!

I would like to send a special acknowledgement to Dr. Magnus Persson and Dr. Philipp Geipel for encouraging me to start the project and for their support in times when you are just sick and tired of it all.

Last but not least I would like to thank my family for their continuous support and Cristin for having patience with me spending a lot of time in Lund and always believing in me.

Contents

Nomenclature **xi**

1 Introduction **1**
1.1 Background 1
1.2 Thesis objectives 4
1.3 Thesis outline 4

2 Reacting Flows in Gas Turbine Combustors **7**
2.1 Fluid flow of industrial gas turbines 7
2.2 Modes of combustion 8
2.2.1 Non-premixed flames 8
2.2.2 Premixed and partially premixed flames 8
2.3 Lean premixed flames 9
2.3.1 Laminar premixed flames 9
2.3.2 Turbulent premixed flames 13
2.4 Flow and flame interactions 15

3 Modelling of Turbulent Reacting Flows in Gas Turbine Combustors **17**
3.1 Governing equations for turbulent reacting flows 17
3.2 DNS (Direct Numerical Simulation) 19
3.3 RAS (Reynolds Averaged Simulation) 19
3.3.1 Governing equations in RAS 20
3.3.2 Turbulence models for RAS 21
3.3.3 Turbulent mass, scalar and heat flux models for RAS . . 23
3.3.4 Combustion Models for RAS 24
3.4 LES (Large Eddy Simulation) 27
3.4.1 Governing equations in LES 28
3.4.2 Sub grid turbulence models for LES 29
3.4.3 Sub grid combustion models for LES 30
3.5 Chemistry speed-up for finite rate chemistry based combustion models 35
3.5.1 ILDM (Intrinsic Low-Dimensional Manifolds) 36
3.5.2 ISAT (In-Situ Adaptive Tabulation) 36
3.5.3 CCM (Chemistry Coordinate Mapping) 37

4 Results and Discussion **39**
4.1 Siemens gas turbine burner 39
4.2 Flamelet based modelling of an industrial gas turbine burner . 40
4.2.1 Closure considerations 41
4.2.2 Chemistry treatment 42

4.2.3 Numerical procedure 45
4.3 Isothermal Flow Results 47
4.4 Reacting Flow Results 49
4.4.1 Atmospheric Cases 49
4.4.2 High Pressure Cases 62

5 Summary of Publications **69**

6 Conclusions **71**
6.1 Future Work 72

References **73**

Nomenclature

Abbreviations

CCM	Chemistry Coordinate Mapping
CFD	Computational Fluid Dynamics
CFL	Courant Friedrichs Lewy Number
DNS	Direct Numerical Simulation
EBU	Eddy Break Up
EDC	Eddy Dissipation Concept
EMST	Euclidean Minimum Spanning Tree
EOA	Ellipsoid Of Accuracy
FDF	Filtered Density Function
FGM	Flamelet Generated Manifold
FRC	Finite Rate Chemistry
FSP	Forward Stagnation Point
IEM	Interaction by Exchange with the Mean
ILDM	Intrinsic Low-Dimension Manifold
ISAT	In-Situ Adaptive Tabulation
LEM	Linear Eddy Model
LES	Large Eddy Simulation
LHS	Left Hand Side
ODE	Ordinary Differential Equation
PDF	Probability Density Function
PSR	Perfectly Stirred Reactor
PVC	Precessing Vortex Core
PaSR	Partially Stirred Reactor
RAS	Reynolds Averaged Simulation
RHS	Right Hand Side
RMS	Root Mean Square
SAS	Scale Adaptive Simulation
SST	Shear Stress Transport
TFM	Thickened Flame Model
TPDF	Transported PDF
VBD	Vortex Break Down

Latin Symbols

A	Pre-exponential factor
C_R	Reaction rate constant
C_S	Smagorinsky constant
D	Burner Diameter
D_α	Diffusion coefficient of species α
D_c	Diffusion coefficient of reaction progress variable
D_Z	Diffusion coefficient of mixture fraction
E_a	Activation energy
$F_{\Delta,\phi}$	Filtered mass density function of ϕ
$F1$	SST model constant
G_ϕ	Axial flux of tangential momentum
G_x	Axial flux of axial momentum
I_0	Stretch rate
J^α	Molecular flux of species α
J^h	Molecular flux of enthalpy
L	Length scale of modelled turbulence
L_{vK}	von Karman length scale
P_{SST}	SST Production term
P_{SAS}	SAS Production term
P_α	Probability density function of α
R	Burner Radius
R_u	Universal gas constant
S	Swirl Number
S_L	Laminar flame speed
S_T	Turbulent flame speed
S_{ij}	Strain rate tensor
T	Temperature
Z	Mixture fraction
U	Magnitude of velocity
V_K	Kolmogorov velocity
$\dot{Q}$	Heat flux
Y	Mass Fraction
Y_c	Un-normalized reaction progress variable
W	Molecular weight
a	Local speed of sound
b	Temperature dependent exponent
c	Reaction progress
c_α	Concentration of specie α
c_μ	Empirical turbulence constant
f_ϕ	Conventional PDF of ϕ

g	Gravitational force
h	Enthalpy
k	Turbulent kinetic energy
k_r	Forward reaction rate
l_t	Turbulent length scale
p	Pressure
t	Time
x	Position vector
u	Velocity vector
u_r	Burner reference velocity
v	Stoichiometric coefficient

Greek Symbols

Δ	Local filter size
Σ	Flame surface density
α	Diffusion coefficient of heat
α_{SST}	SST model constant
α_{FGM}	FGM model constant
β_{SST}	SST model constant
γ	Heat loss ratio
δ_{ij}	Kronecker delta
δ_L	Laminar flame thickness
ε	Dissipation rate of turbulent kinetic energy
ε_c	Scalar dissipation rate
κ	von Karman constant
μ	Dynamic viscosity
μ_t	Turbulent viscosity
ν	Kinematic viscosity
ϕ	Generic scalar
ρ	Density
σ	Schmidt number
τ	Viscous shear stresses
τ_c	Chemical time scale
τ_k	Kolmogorov time scale
τ_{ij}	Shear stress tensor
τ_l	Integral time scale
ω	Turbulence eddy frequency
$\dot{\omega}_\alpha$	Reaction rate of species α
$\dot{\omega}_{Y_c}$	Reaction rate of reaction progress variable

Superscripts

ϕ'	Reynolds residual of ϕ
ϕ''	Favre residual of ϕ

Subscripts

L	Laminar
T	Turbulent
b	Burnt
i, j or k	Cartesian index
sgs	Sub grid scale
u	Un-burnt
α	Chemical species component

Other Symbols

$\langle\phi\rangle$	Reynolds average of ϕ
$\hat{\phi}$	Favre average of ϕ
$\overline{\phi}$	Filtered ϕ
$\tilde{\phi}$	Favre filtered ϕ

Dimensionless numbers

$Da = \frac{\tau_l}{\tau_c}$	Damkhöler number
$Ka = \frac{\tau_c}{\tau_k}$	Karlovitz number
$Le = \frac{\alpha}{D}$	Lewis number
$Ma = \frac{u}{a}$	Mach number
$Re = \frac{UL}{\nu}$	Reynolds Number
$Re_t = \frac{u' l_t}{\nu}$	Turbulent Reynolds number

1 Introduction

1.1 Background

Controlling fire is probably one of the oldest characteristics of humans and has defined the evolution of the human race. Starting from the stone age, combustion was used for cooking and heating to the industrial age where combustion drove the entire industry through firing of coal to today where combustion is still the back bone of both the industrial but also the transport sector. Today, the majority of the world energy production is produced from combustion related sources such as coal, oil and gas, Figure 1.1. In the World

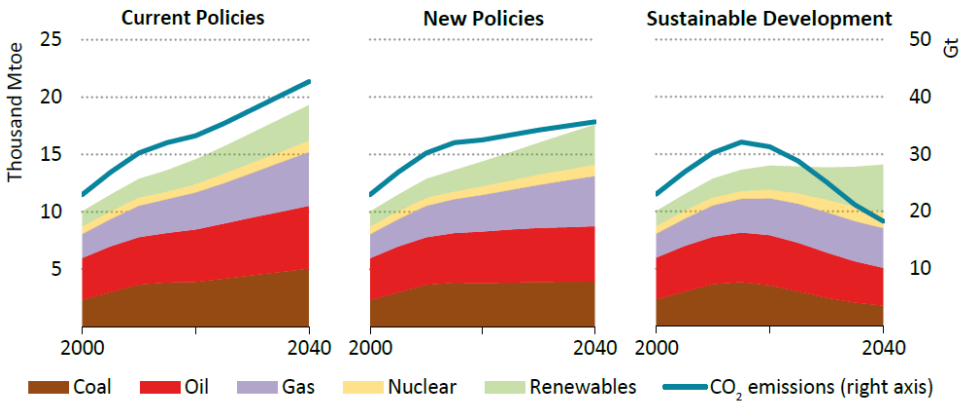

Figure 1.1: Energy demand according to the World Energy Outlook 2017 [52].

Energy Outlook [52], three different scenarios are investigated. One scenario where the current development is simply continued. In this scenario coal, oil and gas keeps increasing with a rapid increase in CO_2 emissions to the atmosphere as a result. The second scenario is the "New policies scenario" where certain political decisions are needed for the CO_2 emissions to at least flatten out after 2017 but still increase slightly. In this scenario the usage of coal and oil stays on the same level between 2017 and 2040 whereas the natural gas usage is increasing. The last scenario is the sustainable scenario where the CO_2 emissions are actually decreasing between years 2017 to 2040 due to a substantial decrease of coal usage. This scenario seems less and less likely due to the global political climate. The usage of natural gas is increasing in all three scenarios and will play a key role in the world energy production for many years to come. Switching from coal and oil based combustion to natural gas combustion have a strong impact on the produced CO_2 emissions. Producing 1 million Btu (approximately 293 kWh) emits 53kg of CO_2 when using natural gas [130]. The corresponding amount of CO_2 from diesel is 73kg

and for anthracite based coal 104kg [130] which is almost twice as much as for natural gas, making natural gas the best option of the fossil fuels. From Figure 1.1 it is also clear that shifting towards renewable fuels is not enough to reduce the overall CO_2 emissions, the total amount of consumed fuel will also have to decrease. Regardless of the scenario it is apparent that a need for increased efficiency for combustion of natural gas is required to preserve a sustainable scenario for the future generations. Increasing the gas turbine efficiency requires even higher turbine inlet temperatures and reduced losses throughout the entire gas turbine. One positive thing in Figure 1.1 is that the share of renewables is increasing in all three scenarios. One potential way of storing power produced by renewable sources such as wind and solar power is through the use of hydrogen co-firing. When the solar and wind plants are producing power the electricity may be used to convert water into hydrogen instead of using the electricity directly on the grid. The hydrogen can then be used in combustion related devices, such as gas turbines, which would reduce the amount of CO_2 emitted to the atmosphere. This way electricity may be produced when there is a need for it rather than when the wind is blowing or the sun is shining.

The predicted natural gas usage according to the "New Policies Scenario" for different regions in the world is shown in Figure 1.2. Here it is seen that the natural gas usage in Europe, Russia and the United States will remain similar to today's levels. All other regions will have a strong increase in natural gas usage where the largest increase, roughly a factor of three, is estimated to take place in China. Many of the regions with a high increase suffer from poor air quality in large parts of the regions. One key emission related to air quality are the nitrogen oxides, NO and NO_2 which are often lumped together as NO_x. The NO_x emissions have a very strong relation to the firing temperature [32]. The most common way of reducing the NO_x emissions in industrial gas turbines is the usage of premixed lean combustion where combustion takes place with an excess of oxidizer. All fuel will be consumed but not all of the oxidizer, where the remaining oxidizer will cool the flame down and thereby reduce the NO_x emissions. Another key issue in gas turbines is the mixing between fuel and air, which plays an important role in the emitted NO_x emissions [38] as well as in how the heat release oscillations will behave. Besides the NO_x emissions other emissions which are harmful to the human health are carbon monoxide (CO), Sulphur oxides (SO_x) and unburned hydrocarbons (UHC). CO is primarily formed in low temperature regions where the combustion may be quenched. Since NO_x and CO are formed in different regions a good combustion system will have to take both NO_x and CO into account during its design phase. UHC is an effect of low efficient combustion where all of the fuel is not fully burnt. This is typically not a large issue in industrial gas turbine where the combustion efficiency is

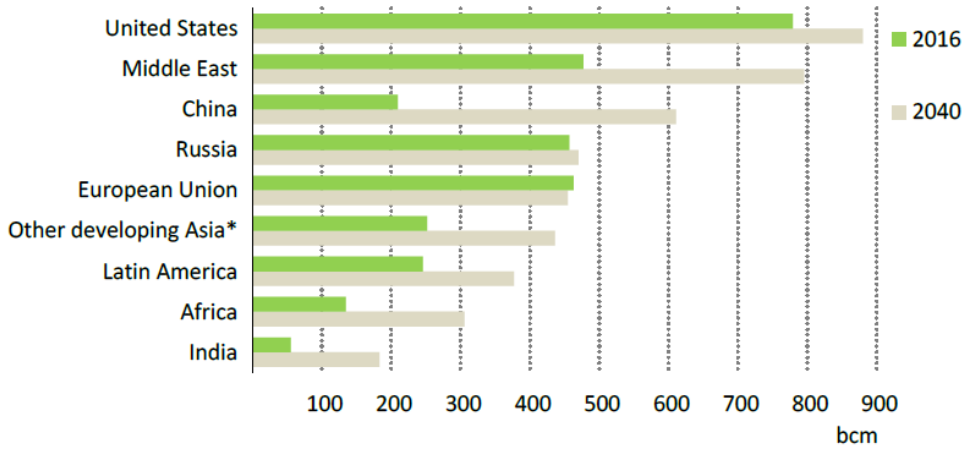

Figure 1.2: World gas demand according to the "New policies scenario", 2016 and forecast 2040.

generally high. SO_x are mainly dependent on the amount of sulphur present in the fuel and the best way to avoid it is to avoid fuel bound sulphur.

One drawback of using lean premixed combustion is the appearance of thermoacoustic instabilities arising due to couplings between flow, acoustic, mixing and heat release perturbations. The thermoacoustic instabilities can increase to devastating levels within seconds if they are not dealt with using active or passive measures. The best way of reducing them is to avoid them when designing the system, but this is not an easy task due to its non-trivial nature. The thermoacoustic instabilities can also be reduced by both passive measures, such as Helmholtz dampers, or by active measures such as adjustable fuel splits or burner staging. Another drawback of lean premixed combustion is the appearance of a flash back. The flash back occurs when the local flame speed is higher than the local flow speed, thus allowing the flame to propagate upstream towards the unburnt mixture. If the flame propagates too far upstream the engine hardware might be damaged with engine failure as the ultimate consequence. The flash back risk is especially pronounced when using highly reactive fuels, such as hydrogen enriched combustion, due to the increased reactivity and sometimes diffusivity.

1.2 Thesis objectives

In this thesis a swirl stabilized, fuel lean, partially premixed gas turbine burner is studied using numerical methods. With the global energy trends the efficiency of the gas turbine as well as the requirements of fuel flexibility are steadily increasing. With the increasing firing temperatures and wider fuel specification, the accuracy of both standard design predictions as well as off design predictions will have to be improved in order for the secondary losses to be acceptable. Knowing how and where your flame stabilizes and how this affects the surrounding environment is crucial when designing new gas turbines as well as when upgrading existing gas turbines. In this thesis, scale resolved turbulence modelling methods are investigated along with flamelet type combustion models. The main goals with this thesis are:

- Increase the understanding of flame stabilization in swirl stabilized, lean premixed gas turbine burners.
- Verify that the usage of scale resolving methods combined with flamelet type combustion is capable of predicting key features of industrial size gas turbine flames, such as flame shape and position.
- Investigate the predictive capabilities of flamelet type combustion models for thermoacoustic instabilities.
- Improve the understanding of flame stabilization using hydrogen enriched fuel in a gas turbine burner.
- Study the model and mesh sensitivity for scale resolving methods on gas turbine burners.

1.3 Thesis outline

Chapter 1

This chapter gives an introduction to the global energy market and the role of the gas turbine in global energy production. The thesis objectives are defined here and a brief outline of the thesis is presented.

Chapter 2

This chapter briefly describes the characteristics of laminar and turbulent premixed flames.

Chapter 3

Here an introduction to modelling of turbulent reacting flows is presented. Modelling approaches for both turbulence and combustion are summarized and their applicability to gas turbine flow /combustion modelling is discussed.

Chapter 4

This chapter summarizes the work done on gas turbine combustion. The chapter goes through background, method and results for reacting and non-reacting flow relevant to gas turbine combustion.

Chapter 5

This chapter presents a summary of the publication on which this thesis is based.

Chapter 6

This last chapter presents the main conclusions from the work.

2 | Reacting Flows in Gas Turbine Combustors

2.1 Fluid flow of industrial gas turbines

The fluid flow through a gas turbine is essential for its function and performance. The operational fluid is air entering the gas turbine and exhaust gases exiting the gas turbine. A gas turbine principally consists of three parts, the compressor, the combustion chamber and the turbine. The compressor increases the pressure and temperature of the air. Fuel is added to the system in the combustion chamber and the mixture between air and fuel is reacting, increasing the temperature of the flow. The flow is then expanded through the turbine section where thermal energy is converted into rotational energy. Some part of the rotational energy is used for powering the compressor, which is linked to the turbine through a shaft, and the remaining energy is available for net usage. In industrial gas turbines the net rotational energy is often used for electricity production or for mechanical drive applications. The power output from an industrial gas turbine is ranging from the small gas turbines with only a few MWs to the largest gas turbine with a power output in the order of 500MW with exhaust mass flows ranging from 20-1000 kg/s. The pressure ratio between different sizes and types of industrial gas turbines is ranging between $\sim 10 - 25$. Given these mass flows and pressure ratios the flow is highly turbulent, often with Reynolds numbers above 1,000,000 at full load conditions.

The combustion chamber is affected by both the compressor, which specifies the engine mass flow, as well as the turbine which specifies the engine pressure. The impact of the combustion chamber on the compressor is mainly in terms of the additional pressure required to overcome the combustor pressure drop. The impact of the combustion chamber on the turbine is more pronounced since the net heat input comes from the combustion chamber. One key design parameter when designing a gas turbine is the turbine inlet temperature, referring to the temperature upstream the nozzle guide vane of the turbine. The magnitude of the turbine inlet temperature plays a key role in the gas turbine cycle and the distribution of the temperature will have a strong impact on the turbine service life, hence it is very beneficial to have good prediction of both magnitude and distribution. The turbine inlet temperature as well as the combustion chamber wall temperatures are dependent on the flame shape and location. The flame shape and location on the other hand rely heavily on local flow parameters upstream the flame such as, velocity distribution and distribution of fuel as well as the local flow and flame dynamics.

2.2 Modes of combustion

2.2.1 Non-premixed flames

Traditionally the most common type of combustion is non-premixed, i.e. the fuel and the oxidizer are introduced separately to the combustion process. Non-premixed combustion is characterised by high stability and high local firing temperatures. Non-premixed flames are controlled by the rate at which fuel and oxidizer can be transported to the flame front. For laminar flames, diffusion will dominate the supply rate which is why non-premixed flames are often referred to as diffusion flames. Once the fuel and air are mixed they tend to burn close to stoichiometric conditions (all fuel and oxidizer are consumed). For turbulent non-premixed flames both diffusion and turbulent mixing may control the supply rate of fuel and oxidizer to the flame front and the mixing rate will depend on the turbulence intensity level. The main drawback of non-premixed combustion is the high production of nitric oxide, NO_x (NO and/or NO_2), emissions associated with the high firing temperatures, [143]. NO_x has been identified as very harmful to humans and the need to reduce the NO_2 worldwide is crucial, [51,125]. One way to reduce the NO_x emissions is to reduce the local firing temperature. This may be achieved by cooling the non-premixed flame using either inert species or water. This will of course require access to additional water and/or inert species for cooling alongside the fuel and oxidizer.

2.2.2 Premixed and partially premixed flames

The opposite of non-premixed flames are premixed flames. In premixed flames the fuel and oxidizer are mixed before the flame zone. One major difference between non-premixed and premixed flames is that in premixed flames the flame will propagate. Imagine a non-premixed flame, on one side you will have combustion products, which will not burn, and on the other side you will have either fuel or oxidizer, which will not burn separately. In the premixed flame you will still have combustion products on one side but on the other side you will have flammable mixture of fuel and oxidizer which will definitely burn and the flame may propagate towards the fresh mixture. As in non-premixed flames the diffusion rate will play an important role in premixed flames as well, but the reaction rate will play an equally important role in the flame stabilization progress. Ideally the fuel and oxidizer should be mixed to a homogeneous mixture for the flame to be perfectly premixed. In real applications this is seldom the case though. Most often fuel is continuously injected to the oxidizer stream, either in a cyclic manner as in reciprocating

engines or continuously as in gas turbine engines. In most cases there are still gradients in the fuel and oxidizer mixture upstream the flame front making the flames partially premixed. The amount of mixedness or rather of unmixedness plays an important role in the behaviour of the flame and will have to be considered when dealing with partially premixed flames.

2.3 Lean premixed flames

Another way to reduce the firing temperature is to use lean premixed combustion, i.e. combustion where the fuel and air are premixed and there is an excess of oxidizer. This way all of the fuel will react but not all of the oxidizer. The remaining oxidizer will cool the flame down from a high firing temperature to a lower temperature, how low will of course depend on the amount of excess oxidizer.

2.3.1 Laminar premixed flames

In laminar premixed flames the fuel and oxidizer are mixed before the flame and there is no presence of turbulence. The ratio between fuel and oxidizer plays an important role in laminar premixed flames, and is often referred to as equivalence ratio. Equivalence ratios less than unity (an excess of oxidizer) is called lean conditions and an equivalence ratio above unity (excess of fuel) is called rich conditions. The stoichiometric condition is defined so that the equivalence ratio is unity at stoichiometric conditions. If the flame becomes too lean the amount of fuel will not be enough to ignite or maintain combustion and if the flame is too rich the amount of oxidizer will not be enough to maintain combustion, this is called flammability limits. The adiabatic flame temperature is also dependent on the equivalence ratio and reaches its maximum at stoichiometric conditions. In lean flames where there is an excess of oxidizer the oxidizer that is not reacting will cool the reacting part down and the overall temperature will be lower and in a rich flame where there is an excess of fuel all of the fuel will not be oxidized and the adiabatic flame temperature will never be reached. The laminar premixed flame is characterised by a propagation velocity, the laminar flame speed, S_L, and a thickness, the laminar flame thickness, δ_L. The laminar flame thickness may be based on the maximum gradient of the temperature across the flame, which is the case in the current work. The laminar flame speed is dependent on the composition of fuel and oxidizer, the equivalence ratio, the pre-heat temperature of the un-burnt mixture and the pressure. Typically the laminar flame speed will be affected by diffusion of both major and minor species as

well as the consumption/production rate of the species involved in the oxidation process. The laminar flame speed and flame thickness for pure methane (CH_4) is visualised in Figure 2.1. The flame properties are calculated using Cantera [42], along with the GRI-3.0 [37] reaction mechanism. The fuel temperature is kept constant at $T_f = 300$ K for all cases. As seen in Figure 2.1 the temperature and the pressure are acting against each other in the case of the laminar flame speed, which is increasing with an increased pre-heat temperature and decreasing with an increased pressure level. The laminar flame thickness however is decreasing with an increase in both pre-heat temperature and pressure so the smallest laminar flame thickness is found at high pressure and high pre-heat conditions. The strongest effect of an increase in pressure is between 1-10 bar, after that the slope of the curves are relaxing towards zero (although not being zero even at pressures as high as 25 bar). Increasing the equivalence ratio from lean to stoichiometric conditions will increase the laminar flame speed but decrease the laminar flame thickness. From the data in Figure 2.1 it may be concluded that a land-based dry low emission (DLE) gas turbine using methane as fuel with a typical pressure level of 15-25bar and air pre-heat of 600-700K operating with an equivalence ratio around 0.5 has a laminar flame speed in the order of 0.1m/s and a laminar flame thickness in the order of 0.2mm. This is of course not directly relevant since most gas turbine flames are highly turbulent, but may become useful when characterising the turbulent gas turbine flames. The same analysis has been done using a methane/hydrogen mixture (20/80%vol) as fuel, Figure 2.2. Here it is noticed that in general the laminar flame speed is increased with a factor of approximately 2.5 whereas the laminar flame thickness decreases with a factor of approximately 2.5. For pure methane/air flames the maximum laminar flame speed is found close to stoichiometric conditions ($\phi = 1.05$) but in the pure hydrogen/air flame case the maximum laminar flame speed is found at rich conditions close to $\phi = 1.9$. This is due to the much higher diffusivity of the light hydrogen molecule as compared to the methane molecule. When there is an excess of hydrogen the hydrogen molecules are diffusing towards the fresh reactant side of the flame making the overall flame speed increase.

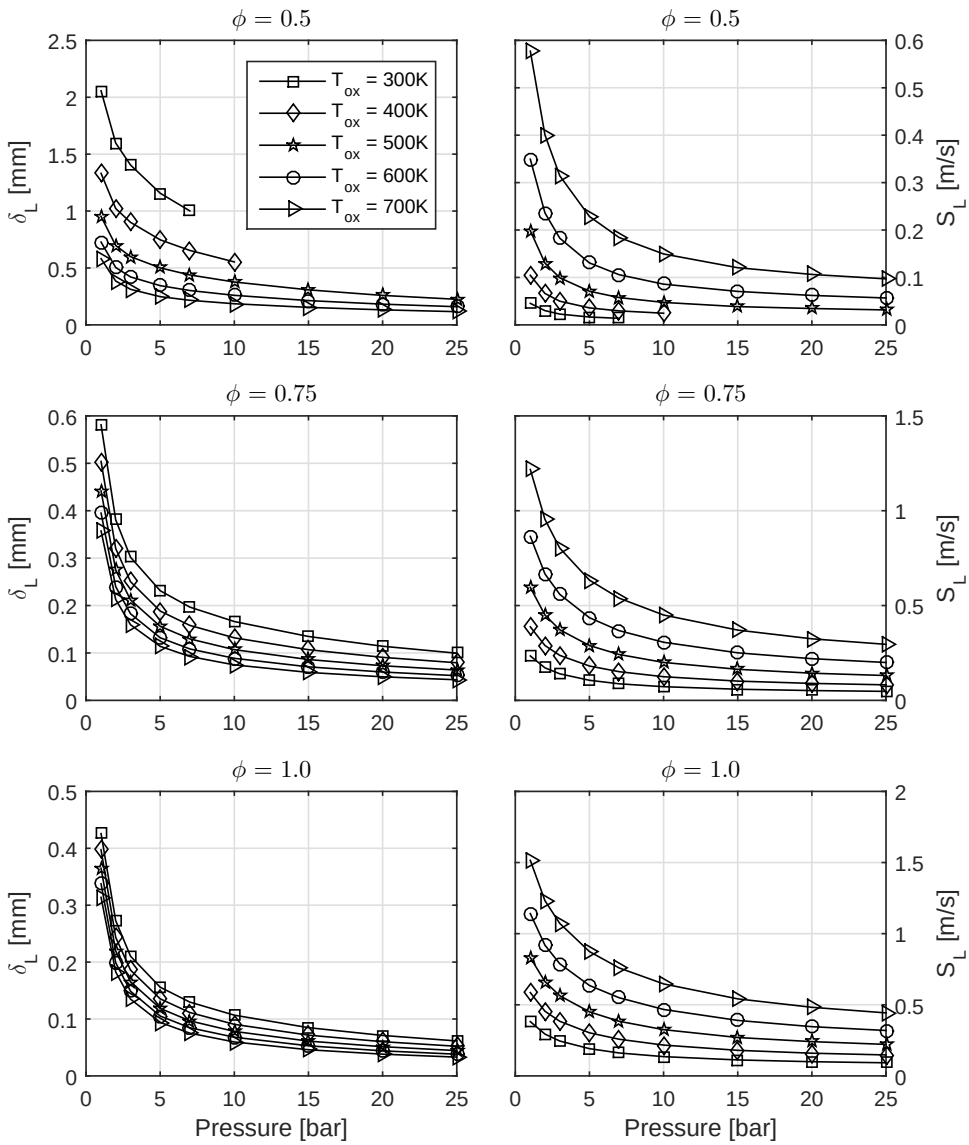

Figure 2.1: Methane/air laminar flame thickness (left) and speed (right) as function of equivalence ratio, pressure and oxidizer temperature.

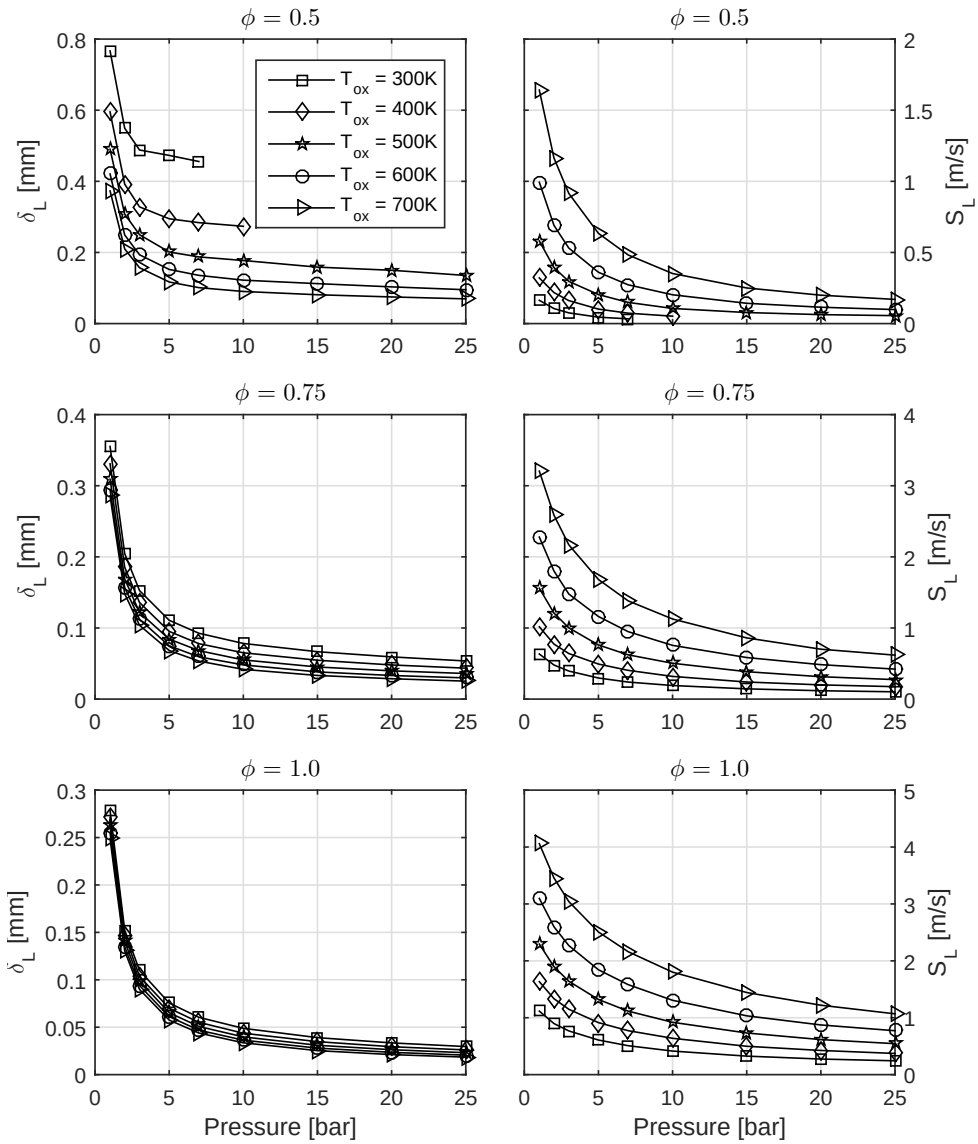

Figure 2.2: Methane(20%vol)/hydrogen(80%vol)/air laminar flame thickness (left) and speed (right) as function of equivalence ratio, pressure and temperature.

2.3.2 Turbulent premixed flames

When discussing turbulent premixed flames it is almost mandatory to introduce dimensionless numbers in order to quantify the properties of the flame. The turbulence is most often quantified by the Reynolds number, Re, which describes the ratio of inertial forces to viscous forces and is defined as $Re = UL/\nu$. The combustion is often related to the turbulence by the use of the Karlovitz and Damkhöler number. The Karlovitz number relates the time scales associated with the smallest turbulent eddies, the Kolmogorov scales, τ_k [68], to the time scales associated with the combustion, τ_c, and is defined as $Ka = \tau_c/\tau_k$. The Damkhöler number on the other hand relates the chemical time scales to the time scales of the largest turbulent eddies, the integral time scale [106] and is defined as $Da = \tau_l/\tau_c$. Knowing these dimensionless numbers, the Borghi diagram [98] is often used to characterize the flame, Figure 2.3. In the laminar flamelet regime the flame is laminar and all reactions

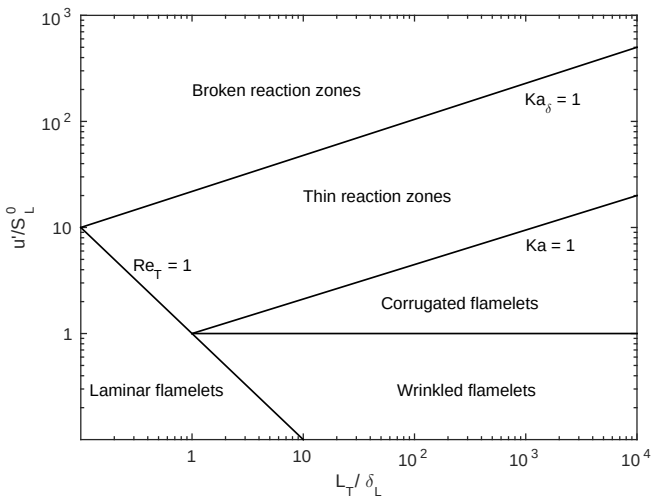

Figure 2.3: The Borghi diagram.

takes place in thin sheets [15]. In the wrinkled and corrugated flamelet regimes the smallest chemical time scales are assumed to be faster than the turbulent time scale. The flames are in fact turbulent but the chemistry still takes place in thin sheets and is most often assumed to be unaffected by the surrounding turbulence. In the thin reaction regime ($Ka \sim 1 - 100$) the turbulent and chemical scales are at least on the same order of magnitude, with the Kolmogorov scale shorter than some of the reaction time scales [23]. The heat release and most reactions still take place in this sheets but the turbulence will most likely affect at least some of the reactions. In the broken reaction zone

regime ($Ka > 100$) the turbulence is believed to have a strong impact on the chemistry. Some reaction fronts may be heavily disturbed and at some point even the heat release will be disturbed by the turbulence. This region of the turbulent combustion still have many question marks and the understanding of combustion with high Karlovitz numbers heavily rely on more advanced laser diagnostics and DNS data. There are recent experimental campaigns of high Karlovits and Reynolds number flows present [138,145,146] and DNS simulations of this regime [20,139]. Both the experimental data and DNS data point towards the fact that even though the Karlovitz number is substantially higher than 100 the inner reaction layer of the flame is still intact, giving very little evidence of distributed combustion in the bordering regime between thin reaction zones and the broken reaction zone regime.

As for laminar premixed flames, turbulent premixed flames are characterised by a propagation speed, the turbulent flame speed. The turbulent flame speed is most often higher than the laminar flame speed and is affected by the same parameters as the laminar flame speed plus quantities related to how the turbulence is affecting the local flame front, such as flame wrinkling and local quenching of the flame [31]. There are many different turbulent flame speed measurements present for hydrocarbon and hydrogen fuels, for example [34, 66, 73, 134, 135, 137, 141]. To separate the effect of turbulence from the effect of changes in laminar flame speed, both the turbulent flame speed and the turbulent velocity fluctuations are usually normalized by the laminar flame speed. All measurements report an increase in the turbulent flame speed with increasing turbulent fluctuations, but the magnitude of the increase depends on the level of turbulence and is affected by the experimental set-up and measurement method. It appears that the most straight forward way of using the experimental data is to compare trends of varied parameters within each measurement campaign, not against each other. The effect of pressure and pre-heat temperature is investigated in [66,134,135,141]. Here it is found that the pre-heat does not have a strong relative impact on the turbulent flame speed if the increase in laminar flame speed is taken into account. The pressure on the other hand seems to have the opposite effect than in the laminar case, i.e. the relative increase in turbulent flame speed is increasing with an increasing pressure. The effect of hydrogen addition (up to 50% by volume) to methane flames and the equivalence ratio dependence is investigated in [34]. It is reported that an increase in hydrogen content increases the relative turbulent flame speed compared to the laminar flame speed. The relative turbulent flame speed is also reported to increase with a decreasing equivalence ratio. Extreme levels of turbulence intensities, $u'/S_L > 150$ is investigated in [137]. Here it is reported that the flame surface density is not increasing after a certain amount of turbulence, instead the turbulent diffusion will play an important role for the increase in consumption speed at extreme

levels of turbulence. It is also concluded that the turbulence should ideally be quantified at the location of the flame front, not at the burner nozzle or centre line which is usually the case when determining global flame characteristics.

2.4 Flow and flame interactions

The Reynolds number in gas turbine combustors is in the order of 1,000,000-2,000,000 at full load and the thermal power in each burner is in the order of several MW. It is natural that there exist interactions between the highly turbulent flow and highly energetic flame. The fundamental flame stabilization process of swirl stabilized flames depends on the interaction between flow and flame. When the swirling flow is expanded a vortex break down occurs [79] with a central and sometimes an outer re-circulation zone as a result. The flame is allowed to stabilized in the shear layers of the re-circulation zones where the local flow speed and flame speed are equal. The vortex break down can also give rise to more complex flow patterns such as precessing vortex cores (PVC) [129] where a local vortex is precessing around the centre axis of the swirling flow. This PVC will also most likely interact with the flame and may play an important role in how the flame is stabilizing during normal operation. There are also un-wanted interactions between flow and flame such as flame flashback and thermoacoustic instabilities. A flame flashback means that the flame is propagating or even stabilizing too far upstream towards the burner hardware, which eventually will cause burner hardware damage. Thermoacoustic instabilities are interactions between perturbations in the flow, flame, fuel/air mixture and acoustic field of the system [47]. The flow perturbations can be generated from large scale un-steady movements (such as the PVC) or from the turbulence present at high Reynolds numbers flows. The flame perturbations are often summarized as heat release fluctuations and are strongly connected to both fluctuations in the flow field as well as in the mixture between fuel and oxidizer. The final step for the fluctuations to be thermoacoustic is interactions with the acoustic properties of the combustion system. The acoustic eigenmodes of the system are dependent on the system geometry and the local speed of sound, which is determined by the local mixture and temperature. The thermoacoustic instabilities can have different modes and are normally divided into two different types, longitudinal and azimuthal [96] modes. The longitudinal modes act along the centre axis of the combustion chamber and in a clear longitudinal mode all burners may oscillate in phase with each other whereas the azimuthal modes act in the cross direction of the flow. The azimuthal modes may be either stationary modes or spinning modes or combinations between stationary and spinning modes [116]. The predictive tools for combustion instabilities range from simple analytical tools

to full scale LES of complete systems [101].

3 Modelling of Turbulent Reacting Flows in Gas Turbine Combustors

3.1 Governing equations for turbulent reacting flows

The governing equations for a turbulent reacting flow without any modelling assumptions are given by the continuity equation, the conservation of momentum equation, the species equations and the conservation of energy [46]:

$$\frac{\partial \rho}{\partial t} + \frac{\partial \rho u_i}{\partial x_i} = 0 \tag{3.1}$$

$$\frac{\partial \rho u_j}{\partial t} + \frac{\partial \rho u_i u_j}{\partial x_i} = -\frac{\partial p}{\partial x_j} + \frac{\partial \tau_{ij}}{\partial x_i} + \rho g_j \tag{3.2}$$

$$\frac{\partial \rho Y_\alpha}{\partial t} + \frac{\partial \rho u_i Y_\alpha}{\partial x_i} = -\frac{\partial J_i^\alpha}{\partial x_i} + \rho \dot{\omega}_\alpha \tag{3.3}$$

$$\frac{\partial \rho h}{\partial t} + \frac{\partial \rho u_i h}{\partial x_i} = -\frac{\partial J_i^h}{\partial x_i} + \frac{Dp}{Dt} + \tau_{ij}\frac{\partial u_j}{\partial x_i} - \dot{Q}_{rad} \tag{3.4}$$

Here i and j are the components of a three dimensional vector ($i, j = 1, 2, 3$) and α denotes chemical species ($\alpha = 1, 2, ...N_S$). u and Y are the velocity vector and chemical species vector respectively. The pressure is p, the mixture mass density is ρ, the mixture enthalpy is h, body forces per unit mass is g, the viscous stress tensor is τ_{ij}, the rate of creation/consumption of species α is ω_α and finally the molecular fluxes of species and enthalpy are J_i^α and J_i^h respectively. To relate the pressure with the density and temperature the ideal gas law is used:

$$p = \rho R_u T \sum_{\alpha=1}^{N_S} \frac{Y_\alpha}{W_\alpha} \tag{3.5}$$

where R_u is the universal gas constant, T is the temperature and W_α is the molecular weight of specie α. So far, no assumptions regarding the flow/fluid has been adopted. However the fluid is often assumed to be Newtonian where the shear stresses are related through the dynamics viscosity, μ, and the strain rate:

$$\tau_{ij} = \mu\left(\frac{\partial u_i}{\partial x_j} + \frac{\partial u_j}{\partial x_i}\right) - \frac{2}{3}\delta_{ij}\mu\frac{\partial u_k}{\partial x_k} \tag{3.6}$$

and the diffusion of mass and heat to follow Fick's and Fourier's law respectively:

$$J_i^\alpha = -\rho D_\alpha \frac{\partial Y_\alpha}{\partial x_j} \tag{3.7}$$

$$J_i^h = -\rho\alpha\frac{\partial h}{\partial x_j} \tag{3.8}$$

where D_α is the species diffusivity and α is the thermal diffusivity. The chemical source/sink term may be written in terms of the net rate of formation of species α:

$$\rho\dot{\omega}_\alpha = \left(\frac{\partial c_\alpha}{\partial t}\right) W_\alpha \tag{3.9}$$

where the net rate of formation of species α may be expressed as the summation of the rate equation of all reactions, R, included in the chemical kinetics mechanism:

$$\left(\frac{\partial c_\alpha}{\partial t}\right)_{chem} = \sum_{r=1}^{R} k_r \left(v_{r\alpha}^{(p)} - v_{r\alpha}^{(e)}\right) \prod_{N_S=1}^{N_S} c_s^{v_{rs}^{(e)}}, \alpha = 1, ..., N_S \tag{3.10}$$

where c_α is the concentration of species α, k_r is the rate coefficient for each reaction r, $v_{r\alpha}^{(p)}$ and $v_{r\alpha}^{(e)}$ are stoichiometric coefficients for products and reactants. The reaction rate coefficients are typically determined using empirical Arrhenius expressions where the forward reaction rate may be expressed as:

$$k_r = AT^b e^{-\frac{E_a}{RT}} \tag{3.11}$$

where A is the pre-exponential factor, b is the temperature dependence exponent and E_a the activation energy. The backwards reaction rate can be related to the forward reaction rate through equilibrium analysis. When simulating premixed flames it is often very convenient to introduce the reaction progress variable. The reaction progress variable may be defined by the temperature in relation to the unburned temperature and the fully reacted temperature:

$$c = \frac{T - T_u}{T_b - T_u} \tag{3.12}$$

or by any major species that is monotonically increasing or decreasing across the flame front. The corresponding transport equations for the reaction progress is:

$$\frac{\partial \rho c}{\partial t} + \frac{\partial \rho u_k c}{\partial x_k} = \frac{\partial}{\partial x_k}\left(\rho D_c \frac{\partial c}{\partial x_k}\right) + \rho\dot{\omega}_c \tag{3.13}$$

In the case of partially premixed flames or flames with gradient in the concentration field an additional variable is required, the mixture fraction, Z. The mixture fraction is based on the assumption that all atoms are conserved across a flame. The mixture fraction may be defined by using Bilger's [7] definition:

$$Z = \frac{Z_C/(mW_c) + Z_H/(nW_H) + 2(Y_{O_2,u} - Z_O)/(v_{O_2}W_{O_2})}{Z_{C,1}/(nW_C) + Z_{H,1}/(mW_H) + 2Y_{O_2,u}/(v_{O_2}W_{O_2})} \tag{3.14}$$

Since the mixture fraction is based on atom conservation it is a passive scalar without chemical source terms. The transport equation for the mixture fraction (assuming unity Lewis number or equal species diffusivities) is:

$$\frac{\partial \rho Z}{\partial t} + \frac{\partial \rho u_k Z}{\partial x_k} = \frac{\partial}{\partial x_k}\left(\rho D_Z \frac{\partial Z}{\partial x_k}\right) \tag{3.15}$$

3.2 DNS (Direct Numerical Simulation)

The most straight forward way of solving the equations described in section 3.1 is to directly discretizise them using the continuum mechanics assumptions, this is called DNS (Direct Numerical Simulation) and by definition no turbulence nor combustion model is used (all though the kinetic theory for the chemistry could be classed as a model, especially if reduced schemes are applied). To solve the complete governing equations for a turbulent reacting flow described in section 3.1 all scales (both turbulent and chemical) in both space and time will have to be resolved. Today DNS is used mainly for generic flows with small physical domains and low Reynolds numbers. This is often very expensive and generates large quantities of data that often requires processing before it becomes useful. The DNS approach is out of reach for most industrial flow cases due to large geometries and often high Reynolds numbers, but it is a very useful tool for investigating fundamental combustion properties such as turbulence chemistry interactions.

3.3 RAS (Reynolds Averaged Simulation)

To avoid resolving all small scales typically present in DNS the flow may be divided into one averaged part and one fluctuating part such as:

$$\phi = \langle \phi \rangle + \phi' \tag{3.16}$$

All small scales are lumped into the fluctuating part and only large bulk flow motions are kept in the averaged part, where the averaged part may be solved for directly and the fluctuating part may be modelled. When dealing with reacting flows it is often convenient to use density weighted averages or Favre averages, [58]:

$$\hat{\phi} = \frac{\langle \rho \phi \rangle}{\langle \rho \rangle} \tag{3.17}$$

3.3.1 Governing equations in RAS

Applying the Reynolds decomposition to the equations described in section 3.1 gives:

$$\frac{\partial\langle\rho\rangle}{\partial t}+\frac{\partial\langle\rho\rangle\hat{u}_i}{\partial x_i}=0 \tag{3.18}$$

$$\begin{aligned}\frac{\partial\langle\rho\rangle\hat{u_j}}{\partial t}+\frac{\partial\langle\rho\rangle\hat{u}_i\hat{u}_j}{\partial x_i}=&-\frac{\partial\langle\rho\rangle\widehat{u_i''u_j''}}{\partial x_i}-\frac{\partial\langle p\rangle}{\partial x_j}\\&+\frac{\partial}{\partial x_i}\left(\mu\left(\frac{\partial\hat{u}_i}{\partial x_j}+\frac{\partial\hat{u}_j}{\partial x_i}\right)-\frac{2}{3}\delta_{ij}\mu\frac{\partial\hat{u_k}}{\partial x_k}\right)+\langle\rho\rangle g_j\end{aligned} \tag{3.19}$$

$$\frac{\partial\langle\rho\rangle\hat{Y_\alpha}}{\partial t}+\frac{\partial\langle\rho\rangle\hat{u}_i\hat{Y_\alpha}}{\partial x_i}=-\frac{\partial\langle\rho\rangle\widehat{Y_\alpha''u_i''}}{\partial x_i}+\frac{\partial}{\partial x_i}\left(\langle\rho\rangle D_\alpha\frac{\partial\hat{Y_\alpha}}{\partial x_i}\right)+\langle\rho\rangle\hat{\dot{\omega}}_\alpha \tag{3.20}$$

$$\begin{aligned}\frac{\partial\langle\rho\rangle\hat{h}}{\partial t}+\frac{\partial\langle\rho\rangle\hat{u}_i\hat{h}}{\partial x_i}=&-\frac{\partial\langle\rho\rangle\widehat{h''u_i''}}{\partial x_i}+\frac{\partial}{\partial x_i}\left(\langle\rho\rangle\alpha\frac{\partial\hat{h}}{\partial x_i}\right)+\frac{D\langle p\rangle}{Dt}\\&+\langle\tau_{ij}\frac{\partial u_j}{\partial x_i}\rangle-\langle\dot{Q}_{rad}\rangle\end{aligned} \tag{3.21}$$

The resulting system of equations are very similar to the original equations with a few exceptions. Three new terms have now appeared, the first term on the RHS of Equation 3.19 representing the Reynolds stress tensor, the first term on the RHS of Equation 3.20 representing Reynolds mass fluxes and the first term of the RHS of Equation 3.21 representing Reynolds heat fluxes. All three new terms will require modelling. Also notice that the formation/destruction of species is now represented by the mean rate of formation/destruction of species. As seen in Equation 3.11 the chemical source term is strongly non-linear and will require a model for the transformation into an average chemical source term. Applying the Reynolds decomposition to the reaction progress and mixture fraction equations, Equation 3.13 and 3.15 gives:

$$\frac{\partial\langle\rho\rangle\hat{c}}{\partial t}+\frac{\partial\langle\rho\rangle\hat{u}_k\hat{c}}{\partial x_k}=-\frac{\partial\langle\rho\rangle\widehat{c''u_k''}}{\partial x_k}+\frac{\partial}{\partial x_k}\left(\langle\rho\rangle D_c\frac{\partial\hat{c}}{\partial x_k}\right)+\langle\rho\rangle\hat{\dot{\omega}}_c \tag{3.22}$$

$$\frac{\partial\langle\rho\rangle\hat{Z}}{\partial t}+\frac{\partial\langle\rho\rangle\hat{u}_k\hat{Z}}{\partial x_k}=-\frac{\partial\langle\rho\rangle\widehat{Z''u_k''}}{\partial x_k}+\frac{\partial}{\partial x_k}\left(\langle\rho\rangle D_Z\frac{\partial\hat{Z}}{\partial x_k}\right) \tag{3.23}$$

The first term on the RHS of Equation 3.22 and Equation 3.23 represents the scalar fluxes and will require modelling and the last term of Equation 3.22 represents the mean reaction rate and will also require modelling.

3.3.2 Turbulence models for RAS

The Reynolds stress tensor that appears as the first term of the RHS of Equation 3.19 represents all the turbulent motions in the flow field. Finding suitable models for the Reynolds stresses is the core issue of all turbulence modelling. Equations may be derived for solving the Reynolds stress tensor as well, but that will yield more unknown therms than available equations that in turns needs modelling and so on. This is often referred to as the closure problem within turbulence modelling [106].

Eddy Viscosity based closures

The basis of all eddy viscosity based turbulence closures is that the Reynolds stress tensor, $\langle\rho\rangle\widehat{u_i''u_j''}$, can be directly related to the strain rate tensor and an artificial turbulent viscosity, μ_t. This is done according to the Boussinesq assumption [114]:

$$-\langle\rho\rangle\widehat{u_i''u_j''} = \mu_t\left(\frac{\partial\hat{u}_i}{\partial x_j} + \frac{\partial\hat{u}_j}{\partial x_i} - \frac{2}{3}\frac{\partial\hat{u}_k}{\partial x_k}\delta_{ij}\right) - \frac{2}{3}\langle\rho\rangle\hat{k}\delta_{ij} \tag{3.24}$$

The turbulence model should then provide values of the turbulent viscosity. This approach is widely used but its applicability to a general flow is questionable. In RAS today the eddy viscosity is often modelled using two equation models where a transport equation is solved for the turbulent kinetic energy, k, defined as half the trace of the Reynolds stresses, $\hat{k} = 1/2\widehat{u_k''u_k''}$, and one for the turbulent eddy dissipation rate or eddy frequency. One of the most commonly recognized models is the $k-\varepsilon$ model, [59]. Here the eddy viscosity is related to the turbulent kinetic energy and to the turbulence eddy dissipation rate:

$$\mu_T = c_\mu\langle\rho\rangle\frac{\hat{k}^2}{\hat{\varepsilon}} \tag{3.25}$$

This model may provide good results for simple flows but often fails to predict the turbulence in swirling flows [62]. Another model very similar to the $k-\varepsilon$ model is the $k-\omega$ model [144]. The basic assumptions are the same but instead of solving a transport equation for the turbulence dissipation rate a transport equation for the turbulence eddy frequency, ε/k, is solved along with a transport equation for the turbulence kinetic energy. A mixture between the $k-\varepsilon$ and the $k-\omega$ model is obtained in the $k-\omega-SST$ model [83,84] where the free stream properties from $k-\omega$ are combined with the wall properties of $k-\varepsilon$:

$$\frac{\partial\langle\rho\rangle\hat{k}}{\partial t} + \frac{\partial\langle\rho\rangle\hat{u_k}\hat{k}}{\partial x_k} = P_{SST} - c_\mu\langle\rho\rangle\hat{k}\hat{\omega} + \frac{\partial}{\partial x_k}\left[\left(\mu + \frac{\mu_t}{\sigma_k}\right)\frac{\partial\hat{k}}{\partial x_k}\right] \tag{3.26}$$

$$\frac{\partial\langle\rho\rangle\hat{\omega}}{\partial t}+\frac{\partial\langle\rho\rangle\hat{u}_k\hat{\omega}}{\partial x_k}=\alpha_{SST}\frac{\hat{\omega}}{\hat{k}}P_{SST}-\beta_{SST}\langle\rho\rangle\hat{\omega}^2+\frac{\partial}{\partial x_k}\left[\left(\mu+\frac{\mu_t}{\sigma_\omega}\right)\frac{\partial\hat{\omega}}{\partial x_k}\right]+2\left(1-F_1\right)\frac{\langle\rho\rangle}{\sigma_{\omega 2}\hat{\omega}}\frac{\partial\hat{k}}{\partial x_k}\frac{\partial\hat{\omega}}{\partial x_k} \tag{3.27}$$

where P_{SST} is a production term. α_{SST} and β_{SST} are calculated according to $\alpha_{SST}=\alpha_1F_1+\alpha_2(1-F_1)$ and $\beta_{SST}=\beta_1F_1+\beta_2(1-F_1)$ where F_1 is a blending function in the SST model and α_1, α_2, β_1 and β_2 are model constants. The blending function F_1 is:

$$F_1=tanh\left(\left[min\left(max\left(\frac{\sqrt{k}}{0.09\omega d},\frac{500\nu}{d^2\omega}\right),\frac{2k}{d^2CD_{k\omega}}\right)\right]^4\right) \tag{3.28}$$

where d is the wall distance and $CD_{k\omega}=max(\frac{1}{\omega}\nabla k\cdot\nabla\omega,10^{-20})$.

Reynolds stress models

The Reynolds stresses may also be modelled directly by solving a transport equation for each of the Reynolds stresses along with one equation for the turbulent eddy dissipation rate or frequency. This way a total of seven different equations are required, each with model constants connected to it. The conservation equations for the variable density flow Reynolds stresses without any modelling assumptions are [58]:

$$\frac{\partial\langle\rho\rangle\widehat{u_i''u_j''}}{\partial t}+\frac{\partial\langle\rho\rangle\hat{u}_k\widehat{u_i''u_j''}}{\partial x_k}=-\frac{\partial}{\partial x_k}T_{kij}+P_{ij}+\Phi_{ij}+\phi_{ij}+\varepsilon_{ij}, \tag{3.29}$$

$$\begin{aligned}
T_{kij}&=\langle\rho\rangle\widehat{u_k''u_i''u_j''},\\
P_{ij}&=-\langle\rho\rangle\left(\widehat{u_i''u_k''}\frac{\partial\hat{u}_j}{\partial x_k}+\widehat{u_j''u_k''}\frac{\partial\hat{u}_i}{\partial x_k}\right),\\
\Phi_{ij}&=-\left(\langle u_i''\rangle\frac{\partial\langle p\rangle}{\partial x_j}+\langle u_j''\rangle\frac{\partial\langle p\rangle}{\partial x_i}\right),\\
\phi_{ij}&=-\left(\langle u_i''\frac{\partial p'}{\partial x_j}\rangle+\langle u_j''\frac{\partial p'}{\partial x_i}\rangle\right),\\
\varepsilon_{ij}&=-\left(\langle\tau_{ik}\frac{\partial u_j''}{\partial x_k}\rangle+\langle\tau_{jk}\frac{\partial u_i''}{\partial x_k}\rangle\right)
\end{aligned}$$

where T_{kij} represents turbulent transport, P_{ij} production due to main strain, Φ_{ij} effects of mean pressure gradients, effects of turbulent pressure strain and ε_{ij} effects of viscous dissipation. In Equation 3.29 there are now three

unknowns, T_{kij}, ϕ_{ij} and ε_{ij}. Since the Reynolds stress tensor is symmetric six equation are required to solve for the Reynolds stresses along with one equation for the turbulent eddy dissipation/frequency. Some common models are the LRR model, [71] and the SSG model [123]. A review of model constants and model performance is given in [104].

Scale resolving methods

To further improve the turbulence modelling one eddy viscosity based model has been extended to a scale resolving method namely the $k\omega - SST - SAS$ [85, 86] method. The aim of this method is to identify regions where the grid is fine enough to resolve the turbulence and then decrease the amount of eddy viscosity in that region. The transport equation for the turbulent kinetic energy is identical to Equation 3.26 and the transport equation for the turbulence eddy frequency is given by:

$$\frac{\partial\langle\rho\rangle\hat{\omega}}{\partial t} + \frac{\partial\langle\rho\rangle\hat{u}_l\hat{\omega}}{\partial x_l} = \alpha_{SST}\frac{\hat{\omega}}{\hat{k}}P_{SST} - \beta_{SST}\langle\rho\rangle\hat{\omega}^2 + \frac{\partial}{\partial x_l}\left[\left(\mu + \frac{\mu_t}{\sigma_\omega}\right)\frac{\partial\hat{\omega}}{\partial x_l}\right] + 2\left(1 - F_1\right)\frac{\langle\rho\rangle}{\sigma_{\omega 2}\hat{\omega}}\frac{\partial\hat{k}}{\partial x_l}\frac{\partial\hat{\omega}}{\partial x_l} + P_{SAS} \tag{3.30}$$

where the only difference compared to Equation 3.27 is the added production term, P_{SAS}. The additional source term P_{SAS} is described as:

$$P_{SAS} = max\left(\zeta_2\bar{\rho}\kappa S^2\left(\frac{L}{L_{vK}}\right)^2 - C\frac{2\bar{\rho}\tilde{k}}{\sigma_\Phi}max\left(\frac{1}{\tilde{\omega}^2}\frac{\partial\tilde{\omega}}{\partial x_l}\frac{\partial\tilde{\omega}}{\partial x_l}, \frac{1}{\tilde{k}^2}\frac{\partial\tilde{k}}{\partial x_l}\frac{\partial\tilde{k}}{\partial x_l}\right), 0\right) \tag{3.31}$$

where L in Equation 3.31 is the length scale of the modelled turbulence and L_{vK} is the von Karman length scale described as:

$$L = \frac{\sqrt{\tilde{k}}}{\tilde{\omega}c_\mu^{\frac{1}{4}}}, L_{vK} = max\left(\kappa\frac{S}{|\frac{\partial^2\tilde{u}_l}{\partial x_l^2}|}, C_S\sqrt{\frac{\kappa\zeta_2}{\frac{\beta_{SST}}{c_\mu} - \alpha_{SST}}}\Delta\right) \tag{3.32}$$

S in both Equation 3.31 and Equation 3.32 is a scalar invariant of the strain rate tensor S_{ij} defined as $S = \sqrt{2S_{ij}S_{ij}}$ and Δ is mesh dependent such as $\Delta = \Omega_{CV}^{1/3}$ where Ω_{CV} is the local control volume size.

3.3.3 Turbulent mass, scalar and heat flux models for RAS

The unknown turbulent mass, scalar and heat fluxes, $\langle\rho\rangle\widehat{Y_\alpha''u_k''}$, $\langle\rho\rangle\widehat{c''u_k''}$ and $\langle\rho\rangle\widehat{h''u_k''}$ present in the RAS governing equations will require modelling. The

most common way is to adopt a gradient diffusion hypothesis similar to the eddy viscosity based closure for turbulence [58]:

$$\langle\rho\rangle\widehat{Y''_\alpha u''_k} = -\frac{\mu_t}{\sigma_{Y_\alpha}}\frac{\partial\hat{Y}_\alpha}{\partial x_k} \tag{3.33}$$

$$\langle\rho\rangle\widehat{c''u''_k} = -\frac{\mu_t}{\sigma_c}\frac{\partial\hat{c}}{\partial x_k} \tag{3.34}$$

$$\langle\rho\rangle\widehat{h''u''_k} = -\frac{\mu_t}{\sigma_h}\frac{\partial\hat{h}}{\partial x_k} \tag{3.35}$$

Here the turbulent viscosity (provided from the turbulence model) is used combined with a Schmidt number for each of the Reynolds flux that needs closure. The Schmidt numbers are often in the order of unity. As for the Reynolds stresses there exist methods within the flamelet theory [15], where the reaction progress scalar flux may be modelled using second moment methods [104] where the governing equation for a reacting scalar is [58]:

$$\begin{aligned}
\frac{\partial\langle\rho\rangle\widehat{c''u''_i}}{\partial t} + \frac{\partial\langle\rho\rangle\hat{u}_k\widehat{c''u''_i}}{\partial x_k} &= \frac{\partial}{\partial x_k}T_{kci} + P_{ic} + \Phi_{ic} + \phi_{ic} + S_{ic} + \langle\rho\rangle\varepsilon_{ic}, \\
T_{kci} &= -\langle\rho\rangle\widehat{u''_k c''u''_i}, \\
P_{ic} &= -\langle\rho\rangle\left(\widehat{u''_k c''}\frac{\partial\hat{u}_i}{\partial x_k} + \widehat{u''_i u''_k}\frac{\partial\hat{u}_i}{\partial x_k}\right), \\
\Phi_{ic} &= -\langle c''\rangle\frac{\partial\langle p\rangle}{\partial x_k}, \\
\phi_{ic} &= -\langle c''\frac{\partial p'}{\partial x_k}\rangle, \\
S_{ic} &= +\langle\rho\rangle\widehat{c''S_c}, \\
\langle\rho\rangle\varepsilon_{ic} &= \left(\langle\tau_{ik}\frac{\partial c''}{\partial x_k}\rangle - \langle J_{ck}\frac{\partial u''_i}{\partial x_k}\rangle\right)
\end{aligned} \tag{3.36}$$

3.3.4 Combustion Models for RAS

Presumed PDF methods

In the presumed probability density functions (PDF) type of models the combustion is often limited to certain regimes where the PDF of the reaction progress variable and often also of the mixture fraction is *assumed* to be known. This way relations for the mean reaction rate may be derived based on local quantities such as flame surface density or scalar dissipation rate.

One common assumption in presumed PDF is that the flame is within the flamelet regime of combustion [15]. The mean reaction rate may be related to the scalar dissipation rate [13]:

$$\hat{\dot{\omega}}_c = \frac{2}{2C_m - 1}\langle\rho_u\rangle\hat{\varepsilon}_c \tag{3.37}$$

One model for the scalar dissipation rate is the model by Kolla et al. [67] which is developed for use in the flamelet regime:

$$\hat{\varepsilon}_c = \frac{1}{\beta'}\left(\left[2K_c^* - \tau C_4\right]\frac{S_L^0}{\delta_L^0} + C_3\frac{\hat{\varepsilon}}{\hat{k}}\right) \tag{3.38}$$

and has been successfully applied to a gas turbine burner fitted to a pressurized rig [111]. The mean reaction rate may also be related to the flame surface density [14]:

$$\hat{\dot{\omega}}_c = \langle\rho_u\rangle S_L^0 I_0 \Sigma \tag{3.39}$$

Here both transport equations and algebraic closures exist for the flame surface density. The transport equations for the flame surface density often contain a number of unknown terms that needs to be modelled. One way of dealing with the flame surface density is to assume that the flamelet geometry is fractal [43]. Following the work of [74] the fractal flame dimension is assumed to be 7/3, the outer cut off scale is the turbulent integral scale and the inner cut off scale is the Kolmogorov scale. This gives an algebraic expression for the mean reaction rate:

$$\hat{\dot{\omega}}_c = C_R\rho_u I_0\frac{S_L^0}{V_K}\frac{\hat{\varepsilon}}{\hat{k}}\hat{c}(1-\hat{c}) \tag{3.40}$$

This model has also been validated for different pressures and fuels [4] and it is shown that the reaction rate constant C_R is probably dependent on both pressure and Lewis number. The mean reaction rate closure may also be directly related to the turbulent flame speed [148]:

$$\hat{\dot{\omega}}_c = \langle\rho_u\rangle S_T|\nabla\hat{c}| \tag{3.41}$$

There are many models for the turbulent flame speed, for example the model by Zimont et al. [148], the model by Peters [98], the model by Mueller et al. [88, 89] and the model by Bradley et al. [11, 12].

Finite Rate Chemistry based models

The key issue when using finite rate chemistry in RAS is how to couple the effect of turbulence to the reaction rate of each species. The simplest model is to ignore the effect of turbulence in the turbulent combustion. This model

assumes that the mean reaction rate is equal to the reaction rate using a mean quantity:

$$\hat{\dot{\omega}}_\alpha = \dot{\omega}_\alpha(\hat{Y}_\alpha) \tag{3.42}$$

which can only be valid if the turbulent time scales are much faster than the chemical time scales. This corresponds to the broken reaction zone regime in the Borghi diagram. This no model approach may also be refereed to as perfectly stirred reactor (PSR) model. The PSR model often leads to unacceptable errors [102] and more sophisticated models are most often required. The eddy break up model (EBU) is a model proposed by Spalding [121, 122] based on phenomenological studies of turbulent combustion. The model relates the mean reaction rate to known mean quantities and requires no additional transport equations:

$$\hat{\dot{\omega}}_\alpha = C_{EBU}\frac{\hat{\tilde{\varepsilon}}}{\hat{k}}\hat{Y}_\alpha(1-\hat{Y}_\alpha) \tag{3.43}$$

The model is only intended to be used along with global reaction schemes where the involved species is either fuel, oxidizer or products. The EBU model has also been modified to handle more complex chemistry, for example the eddy dissipation concept (EDC) model [33].

Transported PDF methods

The transported PDF theory for reacting flows was first developed by Pope [103]. The idea is that instead of solving for the physical variables (velocity, mass fraction etc.) one solves for its probability density function instead. In this work only the joint composition PDF is covered, but there are however both joint velocity-composition TPDF and joint velocity-frequency-composition TPDF formulations available both with different assumptions connected to them. Besides the joint composition PDF equations, equations for mass, momentum and turbulence are required. The transport equation for the joint composition PDF is:

$$\begin{aligned}
&\frac{\partial \rho f_\phi}{\partial t} + \frac{\partial \rho \hat{u}_i f_\phi}{\partial x_i} + \frac{\partial \rho S_\alpha f_\phi}{\partial \psi_\alpha} - \delta_{\alpha(h)}\frac{\partial \dot{Q}_{rad,em} f_\phi}{\partial \psi_\alpha} = \\
&- \frac{\partial}{\partial x_i}\left[\langle u_i''|\psi\rangle \rho f_\phi\right] + \frac{\partial}{\partial \psi_\alpha}\left[\langle \frac{\partial J_i^\alpha}{\partial x_i}|\psi\rangle f_\phi\right] \\
&- \delta_{\alpha(h)}\frac{\partial}{\partial \psi_\alpha}\left[\langle \dot{Q}_{rad,ab}|\psi\rangle f_\phi\right]
\end{aligned} \tag{3.44}$$

The TPDF equations can't be solved using traditional methods for PDEs, instead some kind of statistical method needs to be applied, for example a

Monte Carlo method. The Monte Carlo method typically uses particles to represent the TPDF equations. This method exists both as Lagrangian where the particles are seeded from the inlet and as Eulerian where a fixed number of particles are frozen inside each fluid mechanics cell. The Lagrangian method has higher accuracy than the Eulerian method, but may be very difficult to run due to lack of particles in certain regions. When the joint composition PDF is known the mass fractions may be obtained through integration across the PDF. All terms on the LHS of Equation 3.44 are in closed form, note that this includes the reacting term which is the main advantage of TPDF over other models available. On the RHS the three terms represents turbulent velocity fluctuations, molecular transport and radiative absorption respectively and needs to be modelled. The transport due to turbulent velocity fluctuations are normally closed using the turbulence model and the absorbed radiations is often ignored. The remaining term, molecular transport or micro mixing, is the main modelling focus when it comes to TPDF. Three micro mixing models are frequently used within the framework of transported PDF: the IEM (Interaction by Exchange with the Mean) model [30], modified Curl's model, [56], and the EMST (Euclidean Minimum Spanning Tree) model [127]. The major difference between the first two models and the last model is that the first two models do not fulfil the requirement of being local in composition space [128]. This difference may have significant effects on for example global extinction predictions [128]. A DNS study has been carried out [69], where the three different micro mixing models are compared with each other using DNS data. The study shows that for syngas cases all three models perform equally well with an under-prediction of reignition in the higher Re number cases. For ethylene flames the EMST model over-predicts the reignition at the high Damköler case whereas both IEM and modified Curl's under-predicts reignition at the high Damköler case. All three models are dependent on the scalar mixing time which is dependent on the mechanical to scalar time scale ratio, C_ϕ. The scalar time scale ratio is normally determined before the simulation is started and is often a subject of sensitivity studies. There are models for variable C_ϕ [126] where the mechanical to scalar time scale is determined through the simulation, but this model is not yet fully evaluated for all types of flames and the choice of mechanical to scalar time scale remain an issue for all micro mixing models. Transported PDF has been applied to many different flames including jet flames [109] and gas turbine burners [97].

3.4 LES (Large Eddy Simulation)

When performing Large Eddy Simulations (LES) the flow is filtered. The most common approach is to filter the flow in space only. This way the flow is

divided into one part that is resolved by the computational grid and one part that's left unresolved and thus needs modelling (sub grid part):

$$\phi(x,t) = \bar{\phi}(x,t) + \phi'(x,t) \tag{3.45}$$

Here $\bar{\phi}$ represents the filtered variable and ϕ' the sub grid part. When dealing with reactive flows is it often convenient to introduce density weighted variables:

$$\tilde{\phi} = \frac{\langle \rho\bar{\phi} \rangle}{\langle \rho \rangle} \tag{3.46}$$

which, combined with Equation 3.45 gives:

$$\phi(x,t) = \tilde{\phi}(x,t) + \phi''(x,t) \tag{3.47}$$

3.4.1 Governing equations in LES

The favre filtered governing equations in reacting LES are:

$$\frac{\partial \bar{\rho}}{\partial t} + \frac{\partial \bar{\rho}\tilde{u}_i}{\partial x_i} = 0 \tag{3.48}$$

$$\frac{\partial \bar{\rho}\tilde{u_j}}{\partial t} + \frac{\partial \bar{\rho}\tilde{u}_i\tilde{u}_j}{\partial x_i} = -\frac{\partial \bar{\rho}\tau_{ij}^r}{\partial x_i} - \frac{\partial \bar{p}}{\partial x_j} + \frac{\partial \bar{\tau}_{ij}}{\partial x_i} + \bar{\rho}g_j, \tag{3.49}$$

$$\tau_{ij}^r = \widetilde{u_i u_j} - \tilde{u}_i\tilde{u}_j$$

$$\frac{\partial \bar{\rho}\tilde{Y_\alpha}}{\partial t} + \frac{\partial \bar{\rho}\tilde{u}_i\tilde{Y_\alpha}}{\partial x_i} = -\frac{\partial \left(\widetilde{\bar{\rho}Y_\alpha u_i} - \bar{\rho}\tilde{Y}_\alpha\tilde{u}_i \right)}{\partial x_i} + \frac{\partial}{\partial x_i}\left(\bar{\rho}D_\alpha \frac{\partial \tilde{Y_\alpha}}{\partial x_i} \right) + \bar{\rho}\tilde{\dot{\omega}}_\alpha \tag{3.50}$$

$$\frac{\partial \bar{\rho}\tilde{h}}{\partial t} + \frac{\partial \bar{\rho}\tilde{u}_i\tilde{h}}{\partial x_i} = -\frac{\partial \left(\widetilde{\bar{\rho}hu_i} - \bar{\rho}\tilde{h}\tilde{u}_i \right)}{\partial x_i} + \frac{\partial}{\partial x_i}\left(\bar{\rho}\alpha \frac{\partial \tilde{h}}{\partial x_i} \right) + \frac{D\bar{p}}{Dt} + \overline{\tau_{ij}\frac{\partial u_j}{\partial x_i}} - \overline{\dot{Q}_{rad}} \tag{3.51}$$

It should be pointed out that the term τ_{ij}^r will behave differently compared to the Reynolds stress in a RAS (Reynolds Averaged Solution) case. In RAS where the flow is divided into one mean and one fluctuating part we have that

the average of the average is the average and the average of the fluctuation is zero:

$$\begin{aligned} \hat{\hat{\phi}} &= \hat{\phi} \\ \hat{\phi''} &= 0 \end{aligned} \tag{3.52}$$

which then yields:

$$\tau_{ij}^r = \widehat{u_i u_j} - \hat{u}_i \hat{u}_j = \widehat{u_i'' u_j''} \tag{3.53}$$

However in LES, where the quantities are filtered and not mean values, a filtered variable does not recover the original filtered variable, i.e,

$$\begin{aligned} \tilde{\tilde{\phi}} &\neq \tilde{\phi} \\ \widetilde{\phi''} &\neq 0 \end{aligned} \tag{3.54}$$

Instead τ_{ij}^r will be expanded as, [46]:

$$\tau_{ij}^r = \widetilde{u_i u_j} - \tilde{u}_i \tilde{u}_j = \widetilde{\tilde{u}_i \tilde{u}_j} + \widetilde{\tilde{u}_i u_j''} + \widetilde{u_i'' \tilde{u}_j} + \widetilde{u_i'' u_j''} - \tilde{u}_i \tilde{u}_j \tag{3.55}$$

The same also applies for the first terms on the RHS of Equation 3.50 and Equation 3.51.

$$\begin{aligned} \widetilde{Y_\alpha u_i} - \tilde{Y}_\alpha \tilde{u}_i &= \widetilde{\tilde{Y}_\alpha \tilde{u}_i} + \widetilde{\tilde{Y}_\alpha u_i''} + \widetilde{Y_\alpha'' \tilde{u}_i} + \widetilde{Y_\alpha'' u_i''} - \tilde{Y}_\alpha \tilde{u}_i \\ \widetilde{h u_i} - \tilde{h} \tilde{u}_i &= \widetilde{\tilde{h} \tilde{u}_i} + \widetilde{\tilde{h} u_i''} + \widetilde{h'' \tilde{u}_i} + \widetilde{h'' u_i''} - \tilde{h} \tilde{u}_i \end{aligned} \tag{3.56}$$

In Equation 3.50 the first term on the right hand side represents the sub grid turbulent transport of scalar fluxes and will require modelling. This term may be modelled using a gradient diffusion assumption or by more sophisticated models. The last term in Equation 3.50 represents the filtered reaction rate of species α. This term will require modelling.

3.4.2 Sub grid turbulence models for LES

In Equation 3.49 the term τ_{ij}^r represents the sub grid stress tensor, which will require modelling. One of the simplest models for the sub grid stress tensor is the Smagorinsky model [120] where the sub grid stress tensor is directly related to the strain rate tensor through the sub grid eddy viscosity:

$$\tau_{ij}^r - \frac{1}{3} \tau_{ij}^r \delta_{ij} = -\nu_t \tilde{S}_{ij} = -\nu_t \left(\frac{\partial \tilde{u}_i}{\partial x_j} + \frac{\partial \tilde{u}_j}{\partial x_i} \right) \tag{3.57}$$

where the sub grid eddy viscosity is modelled as:

$$\nu_t = (C_S\Delta)^2|\tilde{S}|, |\tilde{S}| = \sqrt{\tilde{S}_{ij}\tilde{S}_{ij}} \tag{3.58}$$

Here C_S is a model constant and Δ is the local filter size, normally defined as the cubic root of the local control volume. This model is widely used due to its simple formulation and ability to often reproduce sufficiently accurate results. The sub grid stress tensor, τ_{ij}^r, can also be directly related to the sub grid turbulent kinetic energy, $\tilde{k}_{sgs} = 1/2(\widetilde{u_k^2} - \tilde{u}_k^2)$, instead of using the sub grid eddy viscosity [64]:

$$\tau_{ij}^r - \frac{2}{3}\tilde{k}_{sgs}\delta_{ij} = -2C_k\tilde{k}_{sgs}^{1/2}\Delta\tilde{S}_{ij} \tag{3.59}$$

which will require one additional transport equation for the sub grid turbulent kinetic energy:

$$\frac{\partial\tilde{k}_{sgs}}{\partial t} + \frac{\partial\tilde{u}_i\tilde{k}_{sgs}}{\partial x_i} = -\tau_{ij}^r\frac{\partial\tilde{u}_i}{\partial x_j} - C_\varepsilon\frac{\tilde{k}_{sgs}^{3/2}}{\Delta} + \frac{\partial}{\partial x_i}\left(\frac{\mu_t}{\sigma_k}\frac{\partial\tilde{k}_{sgs}}{\partial x_i}\right) \tag{3.60}$$

3.4.3 Sub grid combustion models for LES

Presumed PDF based models

As for RAS the reaction progress variable, c, is often introduced when simulating premixed flames in LES. The filtered transport equation for the reaction progress variable [8], is:

$$\frac{\partial\bar{\rho}}{\partial t} + \frac{\partial\bar{\rho}\tilde{u}_i\tilde{c}}{\partial x_i} = -\frac{\partial}{\partial x_i}\left(\bar{\rho}\widetilde{u_i c} - \bar{\rho}\tilde{u}_i\tilde{c}\right) + \overline{\frac{\partial}{\partial x_i}\left(\rho D_c\frac{\partial c}{\partial x_i}\right)} + \bar{\dot{\omega}}_c \tag{3.61}$$

where $\tilde{c}$ is the Favre filtered reaction progress variable, D_c is the reaction progress diffusivity and $\bar{\dot{\omega}}_c$ is the chemical reaction rate. The chemical reaction rate requires modelling and this is where the major challenge lies when trying to simulate reacting flows through the use of the reaction progress variable. The molecular diffusion and the reaction terms can be expressed together as [8]:

$$+\overline{\frac{\partial}{\partial x_i}\left(\rho D_c\frac{\partial c}{\partial x_i}\right)} + \bar{\dot{\omega}}_c = \langle\rho\omega\rangle_s\Sigma \approx \bar{\rho}_u S_L\Sigma_{gen} \tag{3.62}$$

where Σ_{gen} is the generalised flame surface density. The main issue is thus to find some appropriate representation of the generalised flame surface density. The simplest and most cost efficient closure for Σ_{gen} is to use an algebraic

closure. Different algebraic models for Σ_{gen} has recently been evaluated in [80] using two different test cases; the Volvo test rig case and a rectangular dump combustor with a sudden expansion, the Oracle burner. Four algebraic models are reported to perform consistently well on both test cases. The four models performing well were the models by Charlette et al. [24], Colin et al. [27], Fureby [39] and Muppala et al. [90]. These four models are shown in Equation 3.63-Equation 3.66.

$$\Sigma_{gen} = \left[1 + min\left[\frac{\Delta}{\delta_L}, \Gamma_\Delta\left(\frac{u'_\Delta}{S_L}\right)\right]\right]^{\beta_1} |\nabla \tilde{c}|, \beta_1 = 0.5 \tag{3.63}$$

$$\Sigma_{gen} = \left[1 + \alpha\Gamma_n\left(\frac{u'_\Delta}{S_L}\right)\right] |\nabla \tilde{c}|, \tag{3.64}$$

$$\alpha = \beta \times \frac{2ln(2)}{3c_{ms}(Re_t^{1/2} - 1)}, \beta = 1, c_{ms} = 0.28$$

$$\Sigma_{gen} = \left[\Gamma_n\left(\frac{u'_\Delta}{S_L}\right)\right]^{D-2} |\nabla \tilde{c}| \tag{3.65}$$

$$\Sigma_{gen} = \left[1 + \frac{0.46}{Le} Re_\Delta^{0.25}\left(\frac{u'_\Delta}{S_L}\right)^{0.3}\left(\frac{p}{p_0}\right)^{0.2}\right] |\nabla \tilde{c}| \tag{3.66}$$

Another way of treating the filtered reaction rate is through the use of flamelet generated manifolds [132, 133] where the laminar reaction rate is tabulated based on laminar flame chemistry. The tables are built up based on certain key parameters, such as the progress variable in case of fully premixed combustion. The filtered reaction rate is then obtained from integration of the laminar reaction rate over presumed PDFs for the key input values to the FGM table. When the LES filter size is decreasing the shape of the PDF will become less important and eventually diminish when the border of DNS is approached. Besides the reactive term in Equation 3.61, the first term on the RHS of Equation 3.61 will also require modelling. This term represents the sub grid scalar fluxes. The most common way to close this term is to use a gradient diffusion assumption, similar to the gradient diffusion closures for the Reynolds fluxes is RAS:

$$(\bar{\rho}\widetilde{u_i c} - \bar{\rho}\tilde{u}_i\tilde{c}) = -\frac{\mu_t}{\sigma_{c_t}}\frac{\partial \tilde{c}}{\partial x_i} \tag{3.67}$$

Using a gradient diffusion type of model all counter gradient transport is neglected. It has been shown that for high heat release rate flame the counter gradient transport is promoted, [136], and that magnitudes comparable to its resolved counter part may be obtained for flames of practical size, [72]. Models

to account for counter gradients transport exist, [108], and the sub grid scalar flux term is then expressed as:

$$(\bar{\rho}\widetilde{u_i c} - \bar{\rho}\tilde{u}_i\tilde{c}) = -\bar{\rho_u} S_L((\bar{c} - \tilde{c})N_i) - \frac{\mu_t}{\sigma_{c_t}}\frac{\partial \tilde{c}}{\partial x_i} \tag{3.68}$$

where N is the normal to the iso-surface of the filtered reaction progress variable defined as, $N = -\nabla\tilde{c}/|\nabla\tilde{c}|$. Note that Equation 3.68 does not account for differential buoyancy effects between pockets of cold reactants and hot products which plays an important role in certain type of flames, for example opposed counter flow jet flames. Presumed PDF simulations with LES has been applied to many different flames including premixed jet flames [26] and gas turbine burners with good results [115]. The FGM model has successfully been applied to model gas turbine burners [29].

Instead of defining a reaction progress according to Equation 3.12, a variable describing the flame front, G, can be introduced instead. G-equation withing the LES framework is described in [100], [142]. The G-equation has been applied to a low swirl burner [21,22,93–95] as well as to a gas turbine (LM6000) burner, [65]. The G-equation model is hard to numerically implement and the codes are often Cartesian in order to achieve sufficient order of discretization.

Finite rate chemistry based models

In finite rate chemistry based models the chemistry is solved for at each fluid mechanics time step. Here the equation system, Equation 3.48-Equation 3.51, is the starting point. The use of detailed chemical kinetics schemes is normally out of the question due to the large amount of computational power required to solve the system of ODEs associated with the chemical kinetics reaction scheme. Instead reduced reaction schemes are used, either global schemes where key features of the laminar flame are reproduced using global reaction paths or skeletal schemes where selected elementary reactions are used to reproduce the features of more detailed schemes. The global schemes may be very useful when predicting global flame features such as temperature gradients but are normally insufficient for detailed flame analysis where for example information regarding minor species are required. The skeletal reaction mechanism is more general and may provide detailed information regarding the flame structure, but the computational effort is often rapidly increasing with the amount of output data desired. The major drawback when using FRC together with LES is that the source term in the filtered species equations, Equation 3.50, is the filtered reaction rate for each species. The major challenge in LES of reacting flows is how to transform the actual reaction rate of a species to the filtered reaction rate of that species without a major loss

of information. The simplest possible model for this purpose is to assume that the LES grid is fine enough to resolve all of the chemical scales so that the filtered reaction rate is simply the reaction rate calculated from filtered variables:

$$\tilde{\dot{\omega}}_\alpha \left(Y_\alpha, T\right) = \dot{\omega}_\alpha \left(\tilde{Y_\alpha}, \tilde{T}\right) \tag{3.69}$$

This is often referred to as the PSR model [102] or "no combustion model". The resolution required for this assumption to be valid is often far out of range in LES. One way to avoid this is to artificially thicken the flame to fit the filtered size in the LES. This is known as the thickened flame model (TFM), [24,25]. The TFM has been successfully applied to both simple flames and more complex flames such as gas turbine burners [9, 10, 116, 117, 124]. As for the RAS case the EDC model may be used for LES [33, 82]. In parallel to the PSR and the EDC models there is the partially stirred reactor model (PaSR) [110], based on the assumption that the each cell is not perfectly mixed. This model uses known sub grid quantities to estimate the sub grid reacting volume fraction:

$$\tilde{\dot{\omega}}_\alpha(Y_\alpha, T) = \frac{\tau_c}{\tau_c + \tau_{mix}} \dot{\omega}_\alpha(\tilde{Y}_\alpha, \tilde{T}) \tag{3.70}$$

The PaSR model has been applied and validated against many turbulent flames including gas turbine burners [17, 76, 77]. The PaSR model has advantages over the PSR model since the chemical and turbulent time scales are taken into account when calculating the filtered reaction rate, but high mesh resolution is still required to reproduce the laminar combustion properties from the chemical kinetics scheme where, ideally, all gradients in temperature and species concentrations should be resolved. A more complete model is the Linear Eddy Model (LEM) by Sankaran and Menon [112]. Here the flow and species transport equations are solved on a rather coarse grid. In each of the grid cells the chemistry is solved on a 1D grid sufficiently fine to resolve all concentration gradients across the flame. This method has a very rigorous formulation and does not dependent on micro mixing models as in the case of transported PDF since the mixing is included in the sub grid LEM model. The main drawback is the cost associated with resolving the sub grid concentration and diffusion gradients associated with turbulent combustion. The LEM model has successfully been applied to a gas turbine burner [113].

Transported FDF

In RAS the PDF represents all turbulence chemistry interactions whereas in LES parts of both chemistry and turbulence may be resolved so the PDF now represents the sub grid turbulence chemistry interactions. Transported PDF

is often called Transported FDF (Filtered Density Functions) within the LES framework. As for the RAS case only the joint-composition FDF is covered here, not the joint-velocity-composition FDF. The transport equation for the joint-composition filtered density function, F, is:

$$\frac{\partial F_{\Delta,\phi}}{\partial t} + \frac{\partial \tilde{u}_i F_{\Delta,\phi}}{x_i} + \frac{\partial S_\alpha F_{\Delta,\phi}}{\partial \psi_\alpha} - \delta_{\alpha(h)} \frac{\partial \rho^{-1} \dot{Q}_{rad,em} F_{\Delta,\phi}}{\partial \psi_\alpha} = \tag{3.71}$$
$$\frac{\partial}{\partial x_i} \left[\left(\tilde{u}_i - \langle u_i | \psi \rangle_\Delta \right) F_{\Delta,\phi} \right] +$$
$$\frac{\partial}{\partial \psi_\alpha} \left[\left\langle \rho^{-1} \frac{\partial J_i^\alpha}{\partial x_i} \right\rangle_\Delta F_{\Delta,\phi} \right] -$$
$$\delta_{\alpha(h)} \frac{\partial}{\partial \psi_\alpha} \left[\left\langle \rho^{-1} \dot{Q}_{rad,abs} | \psi_\alpha \right\rangle_\Delta F_{\Delta,\phi} \right]$$

where the terms on the left hand side are in closed form and the terms on the right hand side will require modelling. The main advantage of TPDF is that the chemical source term (Third term on the LHS of Equation 3.71) appears in a closed form and requires no further modelling! This advantage is huge compared to other models. There are however some drawbacks. Although the chemical source term is in closed form the micro mixing term (second term on RHS in Equation 3.71) still requires a model. This mixing rate play a very important role in the TPDF equations so also the model for the micro mixing will be important. The same models or at least very similar as in TPDF within the RAS framework are typically used. In the composition FDF only the filtered velocity appears in closed form, the sub grid turbulent transport (first term on the RHS of Equation 3.71) will require a model or a sufficiently fine grid to resolve it. From a numerical point of view the TPDF equations are not straight forward to solve due to their stochastic nature. Traditionally Lagrangian particle methods are used to statistically solve the TPDF equations. This is typically extremely expensive compared to other finite rate chemistry based models. For example, if one has a grid of 500,000 cells one might need something like 50-100 particles per cell to statistically resolve the TPDF equations. That means that one would have to solve the $50 * N_{species}$ transport equations for the composition PDF combined with solving the stiff chemistry problem in $500,000 * 50$ cells. Another drawback of using particle based methods is that locally one might end up with regions without particles, making the statistics of the PDF very poor. Recently people have started to use Eulerian stochastic fields [131] instead of particle based models for solving the transported PDF equations for reacting flows. They are more practical to use in traditional CFD solvers due to their homogeneous nature. Typically 8-16 stochastic fields are used for each species, making this method still very expensive compared to simpler finite rate chemistry based models. The main drawback of the stochastic fields method is that it is restricted in

the choice of micro mixing model to models who are smooth in space and time, i.e. stochastic models can not be used. For some cases (possibly most cases) this feature of the stochastic fields can have strong negative effects and reducing the benefits of TPDF compared to for example a traditional PaSR model [110].

FDF using particles has been successfully applied to jet flames [63, 140] and to swirl stabilized gas turbine burners [5]. FDF using stochastic fields have been applied successfully to a number of flames including jet flames [55], swirl stabilised flames [60], gas turbine burners on gas operation [16, 18, 19, 35] and gas turbine burners on liquid operation [61].

3.5 Chemistry speed-up for finite rate chemistry based combustion models

When dealing with finite rate chemistry based models and especially transported PDF methods the computational effort of solving the equation system of the chemistry can be enormous. Even for the simplest fuel possible, pure hydrogen, there are still around 20 reaction steps that needs to be taken into account into the equation system for the chemistry. For more complex but still very simple fuels like methane the number of reactions is in the order of hundreds if a detailed chemical scheme is used. Traditionally this issue has been avoided by introducing global chemical kinetics schemes where only a few key species and reactions are present to globally represent the flame. This strategy might be sufficient if only knowledge of global flame parameters is required, such as flame temperature or laminar flame speed, but even here the global schemes are often limited to certain equivalence ratios. To predict more complex phenomenons like quenching or blow off, detailed knowledge of the chemical kinetics is needed. Recently skeletal mechanisms are becoming popular. The skeletal mechanisms are still based on elementary reactions and have the potential to properly reproduce complex chemical behaviours of the flame. For simple fuels like methane the skeletal schemes are often still in the order of 20-40 reactions which will still be very computationally expensive for most engineering cases. To reduce the computational effort of the chemistry solvers different methods have been developed. Three different chemistry speed up models will be discussed in this report, ILDM [81], ISAT [78, 105] and CCM [53, 54]

3.5.1 ILDM (Intrinsic Low-Dimensional Manifolds)

The idea of ILDM is to use a detailed or skeletal reaction scheme to describe the chemistry and then decouple the very fast chemical time scales. Typically the physical time scales (turbulence, molecular transport etc) are in the order of $10^{-5}-10^{-3}s$ [81] whereas the time scales involved in combustion are ranging from approximately $10^{-9} - 10^{0}s$ [81]. If the very fast time scales can be decoupled a low dimensional manifold can be build up that is controlled by only one or a few control variables. This way it is possible to tabulate the results, given a set of control variables the remaining set of state variables are given. This way only a few reaction needs to be solved for to get the temporal development of the chemical state which have the potential to reduce the computational time by orders of magnitude. Given a set of control variables no further treatment is required for the detailed kinetic scheme. The drawback is that it might not be straight forward to determine the control variables in an efficient manner. Another drawback is that not all reactions are solved for directly so detailed chemical kinetic information regarding the flame can not be obtained.

3.5.2 ISAT (In-Situ Adaptive Tabulation)

ISAT is based on the idea that a table can be built up in situ when running the reactive flow calculation. The reaction problem is reduced to determine the mapping $R(\phi)$ which is the solution to the reaction equation,

$$\frac{d\phi(t)}{dt} = S(\phi[t]) \tag{3.72}$$

after a time, Δt from the initial condition. Since the table is built up during the simulation only the region accessed in composition space will be tabulated, reducing the size of the table to a minimum. Each table point will consist of a composition, ϕ^0, the mapping, $R(\phi^0)$, the gradient of the mapping, $A(\phi^0)$ and an ellipsoid of accuracy, EOA. These table entries give the actual mapping to satisfy Equation 3.72 according to:

$$R(\phi^q) \approx R(\phi^0) + A(\phi^0)(\phi^q - \phi^0) \tag{3.73}$$

The main advantage here is that no assumptions are being made regarding the chemical kinetics scheme and that the tables are only build up with data that are actually used in the simulation at some point. The ideal case for this method is flames with very low variations in thermodynamic conditions, such as stable gas turbine flames. The draw back is that the tables may consume very large amounts of memory. If the thermodynamic state of the flame is

varying a lot, like in a reciprocating engine, the time it takes to build up and store the library may be very large and the benefit from using ISAT is decreasing. Another drawback is how to handle massive parallelisation. Here a table would have to be created for each computational node, which may give very uneven load conditions for the cluster, at least during the table build up.

3.5.3 CCM (Chemistry Coordinate Mapping)

CCM also uses detailed or skeletal chemical kinetics reaction mechanisms. The idea here is that the chemistry in different cells can be clustered based on the local thermodynamic state in the cell. The cells are clustered according to $(T, J_H, \sigma, Y_{Fuel})$ with sufficient resolution where T is the temperature, J_H is the specific element mass ratio of the H atom, $\sigma = \nabla J_H \cdot \nabla J_H$ and Y_{Fuel} is the fuel mass fraction. The method is based on DNS studies where the different key parameters were identified. The advantage of this method is if one has large volumes of similar thermodynamics it clusters all those cells into one group and only one set of chemistry equations are needed to be solved for each group of cells. The drawback is that it might not always be sufficient to cluster the thermodynamics using only a few variables making the precision of the model decrease.

4 Results and Discussion

This chapter is dealing with non-reacting and reacting flow related to gas turbine combustion. Flame stabilization of a swirl stabilized, lean premixed gas turbine burner is investigated in detail. The main focus areas are fuel and air mixing, flame stabilization and thermoacoustics. Different methods for treatment of turbulence and chemistry are evaluated for the different key areas and are used to study the physics behind the swirl stabilized burner.

4.1 Siemens gas turbine burner

In this thesis, the Siemens 3^{rd} generation DLE burner, used in the SGT-600, SGT-700 and SGT-800 industrial gas turbines is studied in detail. The 3^{rd} generation DLE burner is a swirl stabilized lean premixed burner with both gas and liquid fuel capability. An overview of the burner is shown in Figure 4.1. The burner consists of four main components, the swirl generator (swirler),

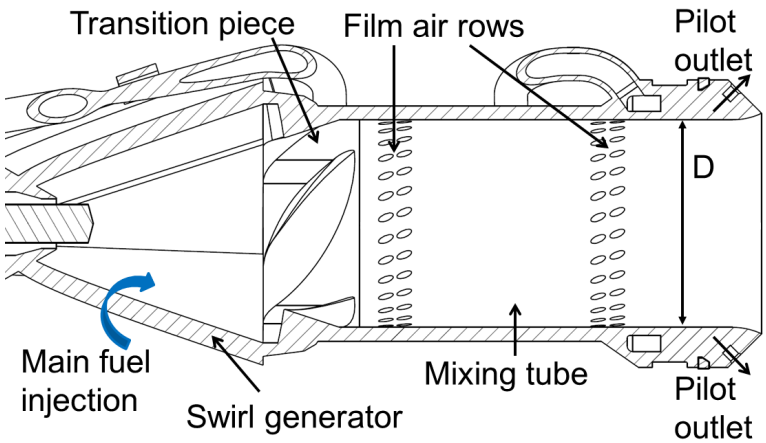

Figure 4.1: Burner overview.

the transition piece, the mixing tube and the pilot flame system. The swirler is made up from four quarter cones (wings) that are shifted from each other, creating four slots where the air is passing. The curvature and alignment of the wings generate the ratio between axial and tangential velocity required for stable operation associated with the burner. The main part of the fuel is injected in the upstream part of the swirler wings through discrete injection points arranged in a jet in cross flow type arrangement carefully designed to achieve the desired fuel and air mixing. The transition piece links the four wings with an annular pipe creating a transition between four air stream into

	Unit	SGT-600	SGT-700	SGT-800
CH_4	%mole	100	100	100
C_2H_6	%mole	100	100*,30	100*,30
C_3H_8	%mole	100	100*,30	100*,30
C_4H_{10} and C_4+	%mole	25	23*,10	15
H_2	%mole	60	60*,30	50*,10
CO	%mole	30	30	30
N_2/CO_2	%mole	40	55*,50	50*,40

Table 4.1: Fuel flexibility chart for Siemens 3^{rd} generation DLE burner. Values with * require special attention such as reduced turbine inlet temperature.

one large bulk flow. The mixing tube allows the fuel and air to further mix before entering the flame region, ensuring that the NO_x emissions are kept at a minimum. The last critical part is the pilot flame system situated at the outer rim of the burner exit. The pilot flame system consists of twelve premixed/partially premixed flames with the main purpose of providing heat and thereby stability to the outer shear layer zone of the burner.

The fuel flexibility capability of this burner in the SGT-600, SGT-700 and SGT-800 are summarized in Table 4.1. All three engines can deal with hydrogen contents up to 50% by volume, which in the case of the SGT-700 and SGT-800 will require special measures, such as reduced turbine inlet temperature. To make operation on 50% hydrogen possible without special measures and to further increase the allowed hydrogen limit without sacrificing operational stability and availability it is very important to have predictive tools that can capture both statistically stationary feature of a flame such as the mean flame shape and flame position as well as non-trivial effects of combustion such as thermoacoustic instabilities and flash back occurrence. The work presented in this thesis aims to explore the usage of scale resolving methods on industrial scale gas turbine burners. The use of flamelet combustion models are evaluated both in terms of mean flame properties but also on time dependent features of the flame.

4.2 Flamelet based modelling of an industrial gas turbine burner

In this study, RAS, LES and hybrid models of them are used for treatment of turbulence. A review of LES for gaseous flames in gas turbine combustors is found in [40], where it is concluded that the maturity of reactive LES for gas turbine combustion is steadily increasing, but more research is needed on full

scale gas turbine components. The computational power is increasing but is and will still be a limiting factor for many years to come. To study the full annular combustion chamber, where the numbers of burners may range from $\sim 8-30$, would imply grid sizes in the order of one billion cells if reasonably resolved LES is to be applied. Taking into account very high Reynolds numbers, small time steps and long residence times it is of great importance to keep the computational expense within each time step as low as possible for this kind of simulations to be realistic. One way of reducing the computational cost is the usage of flamelet models, where the combustion is described using only a few key variables [13]. Using flamelet models in high Karlovitz number flames is a bit contradictory since the combustion regime, as indicated in the Borghi diagram [31], is thought to be outside of the flamelet regime in the thin reaction zone regime or broken reaction zone regime. However, recent experimental [119, 146, 147] and DNS studies [6, 20, 92, 139] of high Karlovitz flames ($Ka > 100$) gives the impression that a majority of the combustion process still takes place in thin layers separated from the turbulent eddies, which would justify the use a flamelet combustion model in that regime. The chemistry in this work is treated using flamelet models in all reactive flow simulations. The Lewis number is assumed to be unity in all reactive simulations, i.e. all species are assumed to have equal mass diffusivity. For methane combustion this assumption is normally valid but for hydrogen enriched combustion the uncertainty is larger since differential diffusion may play an important role in hydrogen combustion [75]. The effect of differential diffusion in highly turbulent flames is not well understood and the effect of differential diffusion is believed to decrease with an increasing Reynolds number [91]. There are methods to include differential diffusion effects within the flamelet theory [28, 107] but it includes uncertainties in terms of new unknowns and model coefficients which is why it is not investigated in this study where the Reynolds numbers are considered to be high.

4.2.1 Closure considerations

RAS

In RAS transport equations are solved for conservation of mass, momentum, turbulent kinetic energy and turbulent frequency in all cases. In the isothermal case an additional transport equation is solved for a passive scalar, representing the fuel and in the reactive cases four additional conservation equations are solved for the enthalpy, mixture fraction and its variance and the reaction progress variable. The turbulence is modelled through the use of the $k-\omega$ SST turbulence model, described in detail by Equation 3.26 and Equation 3.27. This model is selected as a typical model used for industrial gas

turbine relevant flows. An extension to the $k-\omega$ SST is the $k-\omega$ SAS-SST model where the local eddy viscosity is decreased if the mesh is fine enough to resolve some of the local larger flow scales, which is also used in the present study. The only difference between the two models is an additional production term, P_{SAS}, added to Equation 3.27. All model constants for the $k-\omega$ SST and SST-SAS model are summarised in Table 4.2. The potential advantage

C	2	α_1	5/9	β_1	0.0828
C_S	0.11	α_2	0.44	σ_Φ	2/3
c_μ	0.09	β_1	0.075	ζ_2	3.51

Table 4.2: Model constants used in the RANS models.

of the $k-\omega$ SAS-SST over LES is that the wall treatment is more robust and that, potentially, larger time steps may be used which would speed up the simulation. In the reactive case the mean reaction rate in the progress variable equation is closed by the use of Equation 3.40 where the dependence on the model constant C_R is further investigated with model values between $C_R = 1.0 - 2.6$. All scalar flux terms are closed using gradient diffusion type closure with a Schmidt number of 0.9.

LES

In the isothermal LES case transport equations are solved for the conservation of mass and momentum and in the reacting case additional equations are solved for enthalpy, mixture fraction and the reaction progress variable. The sub-grid residual stress tensor is closed by the Smagorinsky model, Equation 3.57, with a model constant value of $C_S = 0.1$. The filtered reaction rate in the progress variable equation is closed based on laminar reaction rates integrated across two presumed PDFs for mixture fraction and reaction progress variable, which are determined in advance. The PDF shape for the progress variable is further investigated in this study. The remaining terms that need closure are the scalar flux terms which are all closed based on a gradient diffusion type closure with a Schmidt number of 0.9.

4.2.2 Chemistry treatment

RAS

Here all species are assumed to have a linear dependence on the progress variable.

$$\widehat{Y}_\alpha = (1-\hat{c})\widehat{Y}_{\alpha,u} + \hat{c}\widehat{Y}_{\alpha,b} \tag{4.1}$$

which is justified by the flamelet assumption, where the local flame front is assumed to be thin. This assumption works well for major species but is not ideal for minor species, such as OH and CH where concentration across the flame is generally not linearly dependent on major species. The local species mass fractions are used when computing the local temperature from the energy equation and when computing the mass weighted transport properties of the gas composition. The effect of turbulence on the laminar flamelet comes in through $\widehat{Y}_{\alpha,b}$, which is calculated based on the presumed PDF of mixture fraction, where a Beta-shaped PDF is used in the PDF integration.

$$\widehat{Y}_{\alpha,b} = \int_0^1 \widehat{Y}_{\alpha}(Z, \hat{\varepsilon}_{Z_{st}}) P_{\hat{Z},\hat{Z}''^2}(Z) dZ \tag{4.2}$$

where the mixture fraction scalar dissipation rate, $\hat{\varepsilon}_{Z_{st}}$, is calculated through the empirical relation, $\hat{\varepsilon}_{Z_{st}} = 2.0\frac{\hat{\varepsilon}}{\hat{k}}\hat{Z}''^2$. The laminar flamelet data is calculated using CFX RIF v.14.5 combined with a built in C1-C4 chemical kinetics scheme.

LES

In this case, the flamelet generated manifold (FGM) approach [132, 133] is used to describe the laminar chemistry. In the FGM approach all species are tabulated based on laminar flame calculations as function of different control variables. Here the chemical kinetic scheme GRI Mech 3.0 [37] is used for calculation of the different laminar flames. The FGM control variables are the reaction progress variable, the mixture fraction, their variances and the local heat loss ratio. The reaction progress variable is described based on weighted linear combinations of mass fractions:

$$Y_c = \sum_{k=1}^{N} \alpha_k Y_k \tag{4.3}$$

Different combinations of species are proposed for defining the reaction progress variable [36, 41, 49, 50, 132]. In this study a progress variable definition optimized for methane/hydrogen mixtures [41] is used with the species weights summarized in Table 4.3. The normalized reaction progress variable is calcu-

α_{CO2}	1	α_{H20}	0.52	α_{C2H2}	0.16	α_H	-0.38
α_{CO}	0.91	α_{H2}	1	α_{OH}	-0.66	α_O	0.4

Table 4.3: Progress variable weight function

lated based on the local reaction progress variable, its unburnt and equilibrium value which are both a function of the local mixture fraction:

$$c = \frac{Y_c - Y_c^0(Z)}{Y_c^{eq}(Z) - Y_c^0(Z)} \tag{4.4}$$

The heat loss ratio is used to account for heat losses from the adiabatic state and is calculated based on the local enthalpy, the adiabatic enthalpy and the sensible enthalpy:

$$\gamma = \frac{h_{ad} - h}{h_{sens}} \tag{4.5}$$

where the local enthalpy comes from the conservation of energy equation and the adiabatic and sensible enthalpy are both functions of the mixture fraction. The final temperature is retrieved from the FGM table. The effect of turbulence on the reaction rate is accounted for by integrating the FGM tables across two presumed shape PDFs:

$$\tilde{\dot{\omega}}_{Y_c} = \int_0^1 \int_0^1 \dot{\omega}_{Y_c}\left(Z, Y_c, \bar{\gamma}\right) P_c\left(c|Z\right) P_Z(Z) dZ dc \tag{4.6}$$

where $\dot{\omega}_{Y_c}$ is the laminar reaction rate stored in the FGM table. $P_Z(Z)$ is a Beta shaped PDF that is parametrized by Z and Z''^2 and $P_c\left(c|Z\right)$ is a Beta shaped PDF parametrized by c and c''^2. The Beta shaped PDF for the conditional progress variable PDF, $P_c\left(Y_c|Z\right)$, is investigated in [48] and the model yields improved results compared to using a Delta function for the conditional PDF since higher order moments than the first moment cannot be accounted for using a Delta shaped PDF. Delta shaped conditional PDF has been used for the reaction progress variable [57,99], which implies that the SGS fluctuations of c (conditioned on Z) has minor effects on the filtered reaction rate. The impact of the conditional progress variable PDF shape is studied here by comparing the results from the Beta PDF and Delta PDF. Both the mixture fraction and reaction progress variable variances are calculated based on a gradient method, here shown for reaction progress variable:

$$\widetilde{Y_c''^2} = \alpha_{FGM} \Delta^2 \left(\frac{\partial \tilde{Y}_c}{\partial x} \right)^2 \tag{4.7}$$

Here Δ is the local filter size, in this case the local grid size, and α_{FGM} is a model constant with a value of $1/12$ for both mixture fraction and reaction progress variable variance, which is in-line with previous work [29].

4.2.3 Numerical procedure

Isothermal flows

In the isothermal flow case, the 3^{rd} generation DLE burner is fitted to a water rig with fluorescent dye seeded through the fuel system. The water rig is used to quantify the mixing capability of the 3^{rd} generation DLE burner. An acrylic burner is used in the experiments, providing optical access to measure the concentration upstream of the burner exit. The water flow rate used to simulate the air is 4 kg/s and the water tracer flow rate is scaled to have the same mass ratio as the fuel/air ratio in a real engine.

Here all simulations are carried out within the framework of CFX v.17.2 [2]. Different numerical treatments are applied dependent on the closure strategy. In the RAS case a high order numerical scheme is used which strives to be as close to second order as possible. In the SAS case a hybrid numerical scheme is used where central differences are used in regions where the SAS model is active (all mixing regions) and the high order scheme is used in regions where it is not. In the LES case a second order central difference scheme is applied for all terms. The temporal scheme is a second order backwards Euler scheme in all cases.

Three different grids are used to study the grid dependence where the grid-resolution in the swirler and mixing tube regions is halved between each grid. The coarse grid is a pure tetrahedra grid with 15 million cells, the middle and fine grids are mixed grids between tetrahedra and hexahedra cell with 6/16.5 million hexahedra/tetrahedra cells in the middle one and 13/55 million hexahedra/tetrahedra cells in the fine grid. The fine grid has a minimum cell size of 0.5mm in the swirler and mixing regions with cell sizes below 0.15mm in the fuel injection region. For the coarse and middle grid a time step of $1e^{-4}$ seconds is used and in the fine grid case a time step of $5e^{-5}$ seconds is used resulting in a RMS CFL number of 0.3 in all cases.

Reacting flows

In the reacting case the 3^{rd} generation DLE burner is fitted to an atmospheric combustion rig [70], schematically shown in Figure 4.2 with the computational domain for the different cases. The air is pre-heated to 697 K where the air mass flow and burner pressure drop are scaled to represent engine conditions. The flame temperature is selected as a typical flame temperature to DLE combustion. The Reynolds number based on the mass flow through the burner is approximately 100,000 in the atmospheric cases and 2,000,000 in the high

pressure cases. The base fuel used in the experiments is natural gas consisting of more than 90% methane in it and is modelled as pure methane in the simulations where the fuel mass flow is scaled based on the heating value. Hydrogen enrichment with 80%vol hydrogen to the base fuel is studied in addition to the methane flames. The flame temperature is maintained for all methane/hydrogen mixtures. The majority of the fuel, 97%, is injected through the main fuel system and 3% through the pilot fuel system in all cases. In addition to the atmospheric cases two high pressure cases are also simulated using the same geometry. The high pressure cases have a pressure level of 20 bar, which is representative of SGT-800 full load conditions. The fuel flow is scaled to represent the flame temperature at real engine conditions. At high pressure conditions a hydrogen enrichment of 30% is investigated where the flame temperature is kept constant. The 30% hydrogen enrichment is the maximum allowed hydrogen content in the SGT-800 with a 15ppm NO_x guarantee limit. All cases are initiated from RAS and simulated until the turbulence appear to be fully developed in the entire domain. The atmospheric cases are time averaged after the initialization for approximately 20 burner and flame-flow through times and the high pressure cases for approximately 10 burner and flame flow through times.

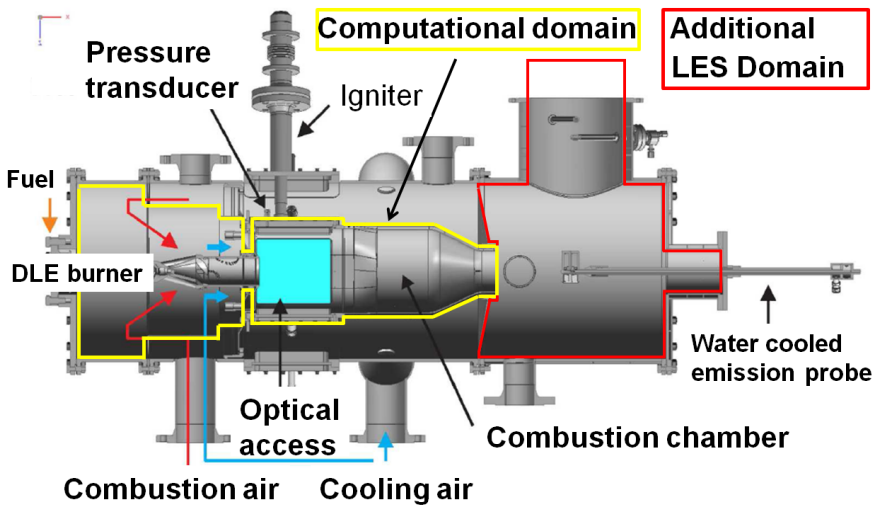

Figure 4.2: Atmospheric combustion rig.

The RAS cases are simulated within the framework of CFX v.14.5 [1] whereas the LES cases are simulated within the framework of StarCCM+ v. 12.02.010 [3]. In the RAS case a high order numerics scheme is applied which is a blended upwind scheme where the accuracy will be as close to second order as possible. In the RAS SAS case a mixed numerical scheme is used where

second order central differences are used in regions where the SAS model is active and the high resolution scheme is used in regions where it is not active. The LES uses a second order central difference scheme. The temporal scheme is second order accurate in all cases. Mass flows are specified at air and fuel inlet boundaries and pressure is specified at the outlet boundary. All walls are treated as no-slip adiabatic walls. Radiation effects are not included in this study. The computational domain is expanded in the LES case to ensure that the acoustic properties of the boundaries will not have an influence on the predictions.

Two pure tetrahedra grids are used for the RAS cases, one with 25 and one optimized with 32 million cells respectively. The main difference between the grids is the refinement level in mixing and reaction regions. The LES grids are pure polyhedral grids with a total of 16 and 28 million cells in grid 1 and 2 respectively. Prism layers are applied to all walls in the LES grids ensuring good wall refinement. Both the fine RAS grid and the LES grid 2 has a maximum cell size of 1 mm in the mixing and reaction region with refinements in areas where smaller scales are situated, such as in fuel injection points and pilot flame regions. The two coarser grids have a maximum cell size of 2 mm in all reaction and mixing regions. Although the local cell sizes are similar between the grids, the polyhedral grid has far more integration points and control surfaces in each cell which should increase the accuracy of the polyhedral grid compared to the tetrahedra grid.

4.3 Isothermal Flow Results

One key parameter in DLE combustion is the ability to efficiently mix fuel and air before entering the flame region. The mixture upstream the flame will determine the local flame temperature and thereby have a very strong impact on the NO_x production and potentially also on the thermoacoustic response. The mixing in the SGT-800 burner is studied by using a water rig. The water passing through the fuel system is seeded with a fluorescent dye and the concentration of the dye can be measured using a laser and a detector. The laser beam is formed into a sheet and the laser intensity is measured 1.2 D upstream the burner exit through the acrylic wall of the test burner used. The results presented here is a summary of **Paper III**. The experimental result, consisting of normalized laser intensity, along with the CFD predictions of mass fractions of a fuel tracer are presented in Figure 4.3. The unsteady RAS-SST predictions are not in good agreement with the experimental data, a concentration peak close to 1.4 is predicted at $r/D = 0.425$ which is not seen in the experiments where a peak is present close to $r/D = 0.275$ with a concentration of 1.15. A local minimum is predicted with the SST model

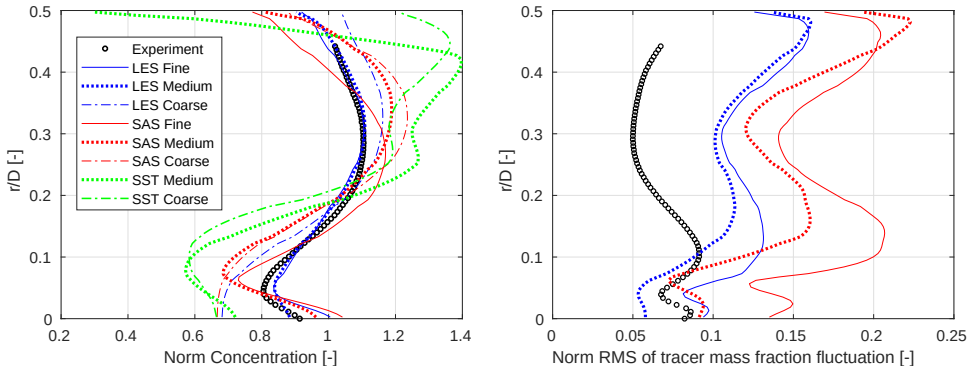

(a) Time averages (b) RMS of fluctuations

Figure 4.3: CFD mixing predictions compared with experimental data in a water rig [87].

close to $r/D = 0.1$ with a concentration below 0.6 which is too low compared to the experimental value. It is also observed that the concentration close to the wall is not well predicted and appears to be very grid dependent. The SST-SAS results are in better agreement with the experimental data than the SST predictions. There is a grid dependence present in the SAS case where the finest grid generally gives the best predictions. The predictions from all three grids show too high maximum concentration and too low minimum concentration which indicates that the mixing rate is under-predicted using the SAS turbulence model. The LES predictions using the two finer grids are in excellent agreement with the measured data, both in terms of maximum and minimum peak location and magnitude. The RMS of fluctuation is qualitatively similar between experiments, LES and SAS. The SAS mode generally predicts higher RMS values than the LES models, which is in line with the mean value predictions where the LES mixing is shown to be faster. In the SAS case the fuel is mixed at a slower pace, resulting in large pockets of fuel tracer present at $x/D = -1.2$ which will generate the high RMS values. It should be pointed out that the RMS values from the experiment is believed to be lower than the reality due to insufficient shutter speed of the camera used in the experiments, however, the mean values will be unaffected by the shutter speed. The slower mixing rate in the SAS model is believed to be caused by insufficient representation of the local turbulence, which play an important role in the mixing process [87]. The decrease in eddy viscosity in regions where local scales may be resolved in the SAS model appears to work well for the largest scales but not for the smaller scales, which are suppressed by the local eddy viscosity. In this flow configuration, LES provides a better representation of the flow and mixing characteristics, but it is possible that

the SAS model still has advantages in industrial wall bound flows, for example in diffusers or in cooling passages.

4.4 Reacting Flow Results

4.4.1 Atmospheric Cases

Methane and natural gas combustion

In this section atmospheric methane and natural gas flames are studied. The results are based on **Paper I**, **II** and **V**. An overview of the flow field is presented in Figure 4.4 where the axial velocity is shown on the bottom plane and the temperature on the back plane. The flow is accelerated when passing through the swirler with a high speed zone close to the centre line as a result. The axial velocity profile becomes more flat close to the burner exit due to radial pressure gradient present in the flow field. When the swirling flow is expanded into the combustion chamber a re-circulation zone known as a vortex break down (VBD) [79] occurs with low speed zones in the inner and outer shear layers. In the VBD a vortex structure may appear that is precessing around the burner centre axis, this is known as a precessing vortex core (PVC) [129]. The PVC is visualized in Figure 4.4 as a low pressure zone close to the burner exit using the iso-surface of $P/P_{outlet} = 0.99$. The local temperature distribution reveals that the flame is shaped like an M, stabilized in the low speed zones associated with the VBD. The local flame front is highly wrinkled by the surrounding flow structures and they are coupled through the thermal expansion across the flame and geometrical expansion into the combustion chamber. The pilot flames are situated at the burner exit rim and are seen as local high temperature zones in the outer part of the flame.

The time averaged reaction progress variable for the SAS and LES cases are presented in Figure 4.5 along with experimental OH-PLIF data for the present configuration. It is not straight forward to compare the laser intensity from OH-PLIF measurements with data from the CFD since the OH-PLIF experiments produces laser intensities and not actual mass fractions. In some cases where the surrounding is well known it is possible to relate the laser intensity to actual mass fractions, but the experimental data here are only qualitative. Here the gradient from the OH-PLIF data is used as a flame front marker and the PDF of the gradient is used for characterising the mean location, shape and movement of the flame front. The instantaneous reaction progress variable in the CFD prediction has most often got sharp gradient and the time average of the reaction progress variable can be compared to the PDF of the OH-PLIF gradient. The PDF of the OH-PLIF gradient show that the flame

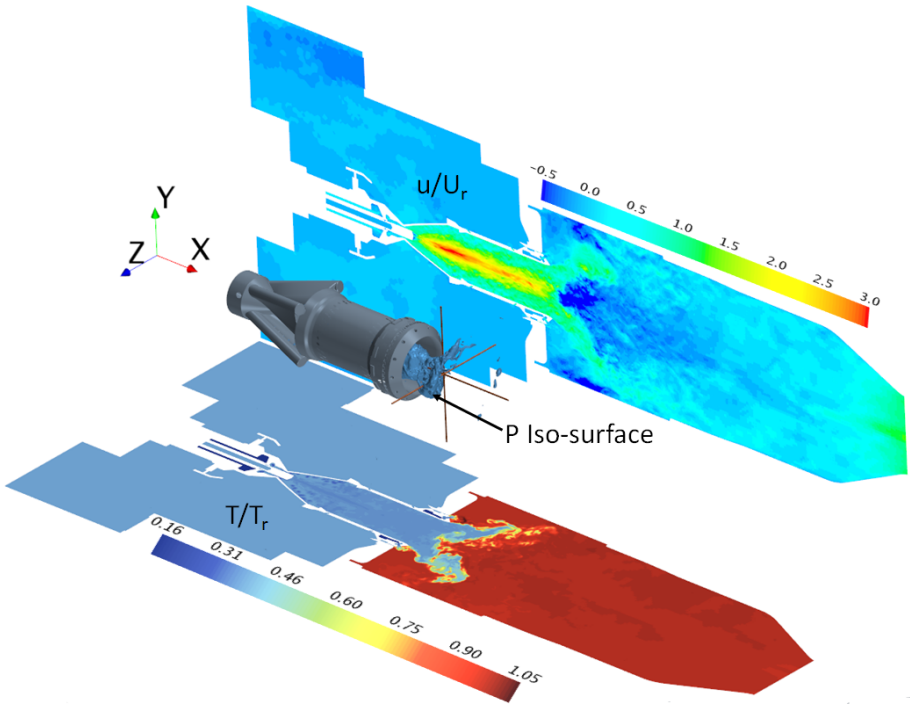

Figure 4.4: Overview of flow field.

has got an M shape on average, stabilized closed to $x/D = 0.3$ and might instantaneously be located between $0 < x/D < 0.75$, which is the width of the laser sheet. The impact of mesh is investigated for both the RAS, SAS and LES cases and the impact of the conditional progress variable PDF shape is investigated in the LES case. RAS combined with the fractal model for progress variable closure predicts a very thin flame on average without movements, with the appearance of an very stretched M. RAS also fails to predict flame shape movements due to changes in the reaction rate constant, making it un-suitable for predictions of hydrogen enrichment. The RAS results are presented in **Paper II** and will not be evaluated further here due to the poor representation of the flame. The coarse SAS grid did not result in any flame dynamics at all and the mean flame shape was not similar to the OH-PLIF measurement, and the results are not further evaluated. The SAS case with a C_R value of 2.6 gives a very compact flame situated close to the burner exit.

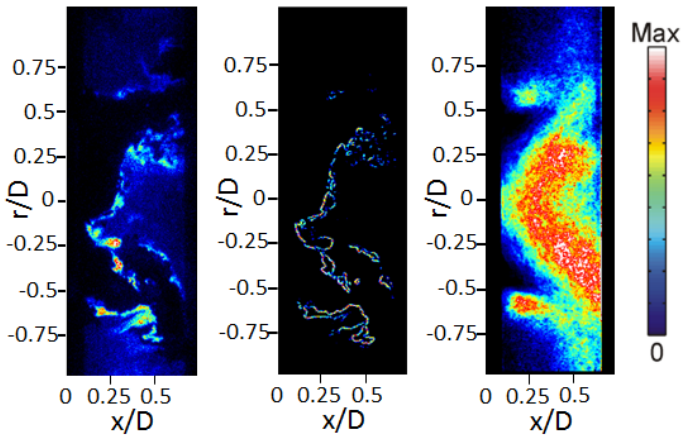

(a) OH-PLIF, instantaneous (left), instantaneous gradient (middle) and PDF of gradient (right)

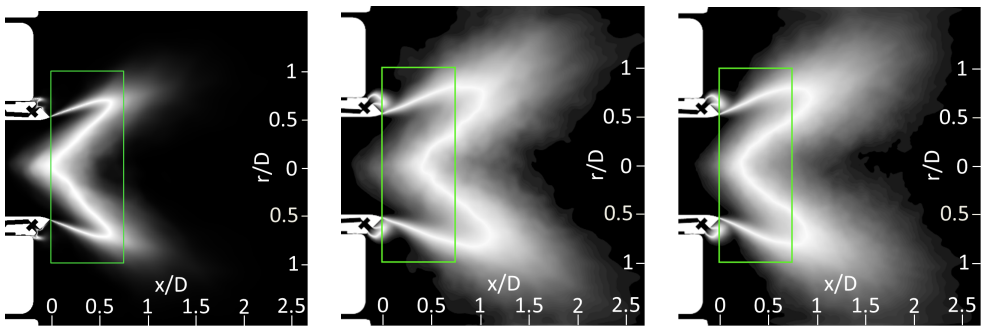

(b) SAS, $C_R = 2.6$ (c) LES, δ-PDF, Mesh 1 (d) LES, δ-PDF, Mesh 2

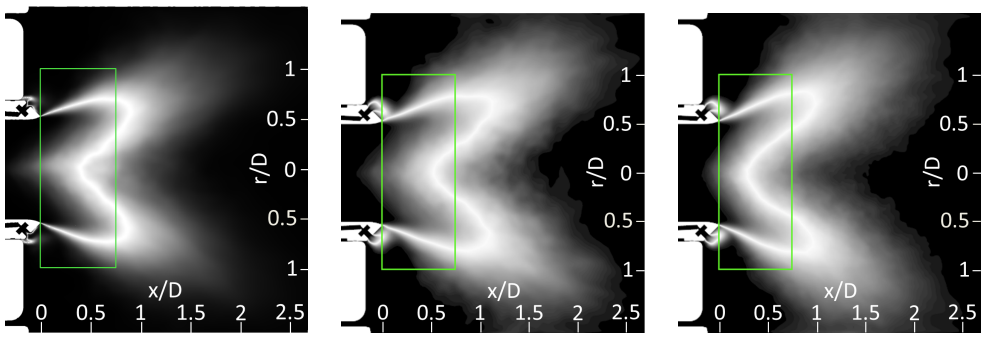

(e) SAS, $C_R = 1.0$ (f) LES, β-PDF, Mesh 1 (g) LES, β-PDF, Mesh 2

Figure 4.5: OH-PLIF data from **Paper V** and time averaged reaction progress variable.

Changing the C_R constant to 1.0 gives a less compact flame and a shift in mean position from $x/D \approx 0$ to $x/D \approx 0.45$, which is in better agreement with the OH-PLIF data. All LES results gives a similar flame shape. There is a clear difference between grid 1 and grid 2 where the mean flame position is moving towards the burner exit in grid 2 without changing its most upstream position. The shape of the conditional PDF for reaction progress variable is most pronounced on grid 1 where the β shaped PDF predicts a more downstream flame position than the δ PDF. The two predictions using grid 2 are very similar and only minor differences are seen. The best prediction is believed to be given by grid 2 combined with the β PDF due to the slightly thinner flame across the centre line. In general, the use of a β PDF instead of a δ PDF will decrease the integrated reaction rate, which is clearly seen in the grid 1 predictions, but not in the grid 2 predictions. On grid 1 the entire laminar flame thickness is believed to be smaller than the grid size, see Figure 2.1 for laminar flame thickness, whereas on grid 2 part of the flame thickness might be resolved. The conclusion from this is that it may be an advantage to use a δ shaped PDF in cases where the entire flame thickness is smaller than the grid and to use a β shaped PDF when the flame thickness might be resolved. One interesting difference between the SAS and LES prediction is the pilot flame shape. In the SAS predictions the pilot flames are M or V shaped and in the LES predictions the flames are more O shaped. The pilot flame shape is not directly measured so the corresponding experimental shape is not known. The shape difference between the two methods suggests that LES combined with FGM predicts a lower reaction rate in the pilot flame region than the SAS combined with a stationary flamelet. Figure 4.5 shows that both LES and SAS combined with a flamelet approach is capable of producing good predictions of the mean flame shape and position, all though the SAS case needed some calibration to give a reasonable flame shape.

The measured pressure fluctuations, at the location indicated in Figure 4.2, along with the computational results are presented in Figure 4.6. A fast Fourier transform (FFT) is presented alongside the measured and predicted time signal of pressure. The pressure fluctuations are normalized by a reference pressure and the time is normalized using the burner mixing tube diameter, D, and the burner reference velocity, u_r, so that $\tau = t*u_r/D$. The frequencies are normalized by the use of the Strouhal number, $St = f*D/u_r$. The time signal reveals that the measured signal and the LES prediction have a very similar appearance. At certain times a low frequent mode is dominant and at other times a middle frequency mode is the dominant one. The time signal from the SAS model have the appearance of a high pass filtered signal where only the lower frequencies are visible, indicating that higher frequency dynamics are dampened out. From the FFT of the time signals, three different regions with high power are seen, one at $St = 0.19$, one at $St = 0.67$ and one close to

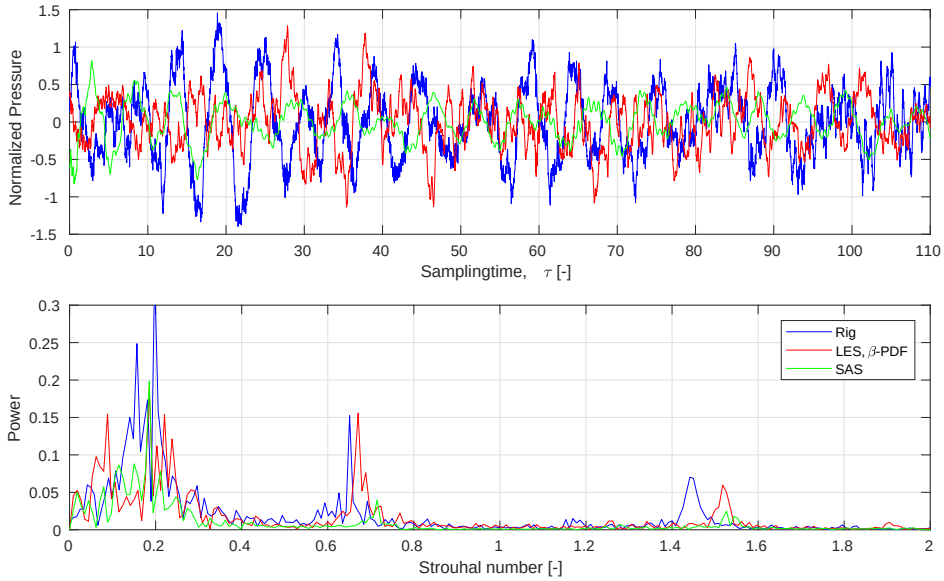

Figure 4.6: Pressure sampled at the pressure transducer location with data from **Paper II** and **Paper V**.

$St = 1.5$. The LES predict the first two regions well, both in terms of Strouhal number and power. The third peak is well predicted in terms of power but slightly over predicted in terms of Strouhal number. Here it should be pointed out that the CFD predictions are carried out using adiabatic wall whereas in the experiments quartz windows are used in the combustion chamber, with good visibility of the flame but high heat losses as a result. Decreasing the temperature close to the wall will locally decrease the speed of sound and therefore decrease the Strouhal number of the transversal eigenfrequencies in the combustion chamber. The SAS model predicts the first region fairly well but under-predicts the power of the two second regions and over-predicts the Strouhal number. A Helmholtz solver is used in **Paper V** to study the eigenfrequencies of the combustion rig and the result for the three regions seen in Figure 4.6 is shown in Figure 4.7. Here 0 represents the node and ± 1 represents the peak of a acoustic wave. The first eigenfrequency at $St = 0.18$ is an axial mode ranging from the inlet plenum to the exhaust duct with nodes located in the burner swirl cone and in the combustion chamber outlet. The second eigenfrequency at $St = 0.67$ is also an axial mode ranging from the burner to the combustion chamber contraction with a nodes in the middle of the combustion chamber, inlet plenum and exhaust duct. The third mode at $St = 1.57$ is a higher order azimuthal mode with a nodal-line along the diagonal of the combustion chamber square section close to the burner exit.

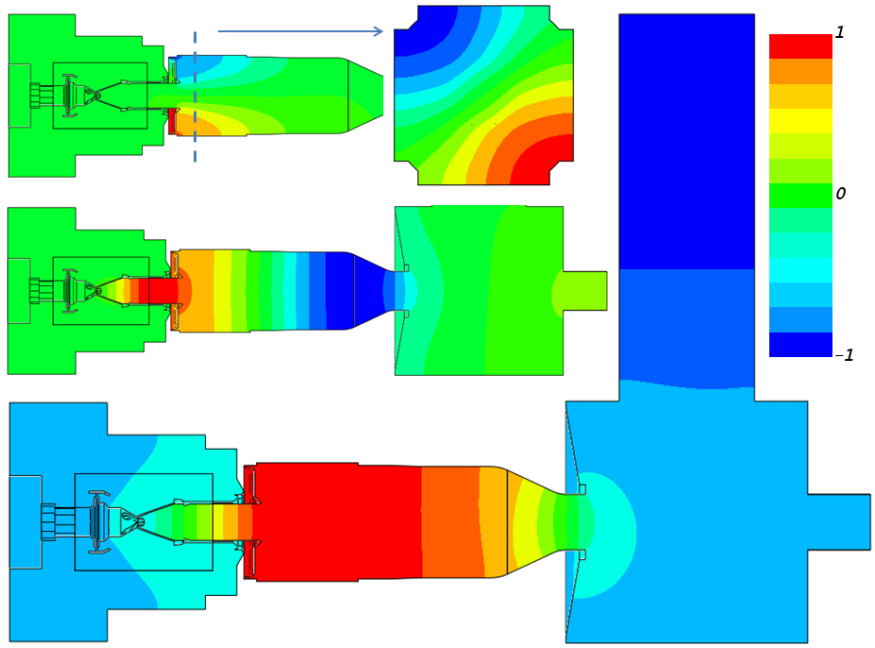

Figure 4.7: Acoustic eigenmodes for $St = 0.18$ (bottom), $St = 0.69$ (middle) and $St = 1.56$ (top) from Helmholtz solver, image from **Paper V**.

The flame and flow dynamics is studied through the temporal evolution of pressure, axial velocity, mixture fraction and flame front location (here represented by $\tilde{c} = 0.5$) on the burner centre line, Figure 4.8. The forward stagnation point (FSP), identified as the most upstream occurrence of zero axial velocity, is moving between $-0.5 < x/D < 0.75$ and the location of the flame front is most often located $\sim 0.25D$ downstream of the FSP location, which may appear strange at a first glance since the flame front it thought to stabilize upstream the FSP where the flow and flame speed are equal. However, the flame stabilization close to the centre line in this case is highly dependent on the local vortex structure and the flame tends to stabilize in the local vortex regions downstream of the FSP rather than in the most upstream location of zero axial velocity, which is how the FSP is defined. From the mixture fraction along the centre line it is obvious that the mixture fraction is fluctuating much more in the region upstream of the flame front and FSP than downstream. This is owing to that the mixture downstream the flame front and FSP are mainly hot combustion products that are recirculated from downstream, which has a long residence time and thus a more uniform mixture. The fluctuations in the mixture fraction upstream the flame arise from the fact that the fuel is injected through discrete injection points in the swirler into a highly turbulent flow field. From spectral analysis of pressure, axial ve-

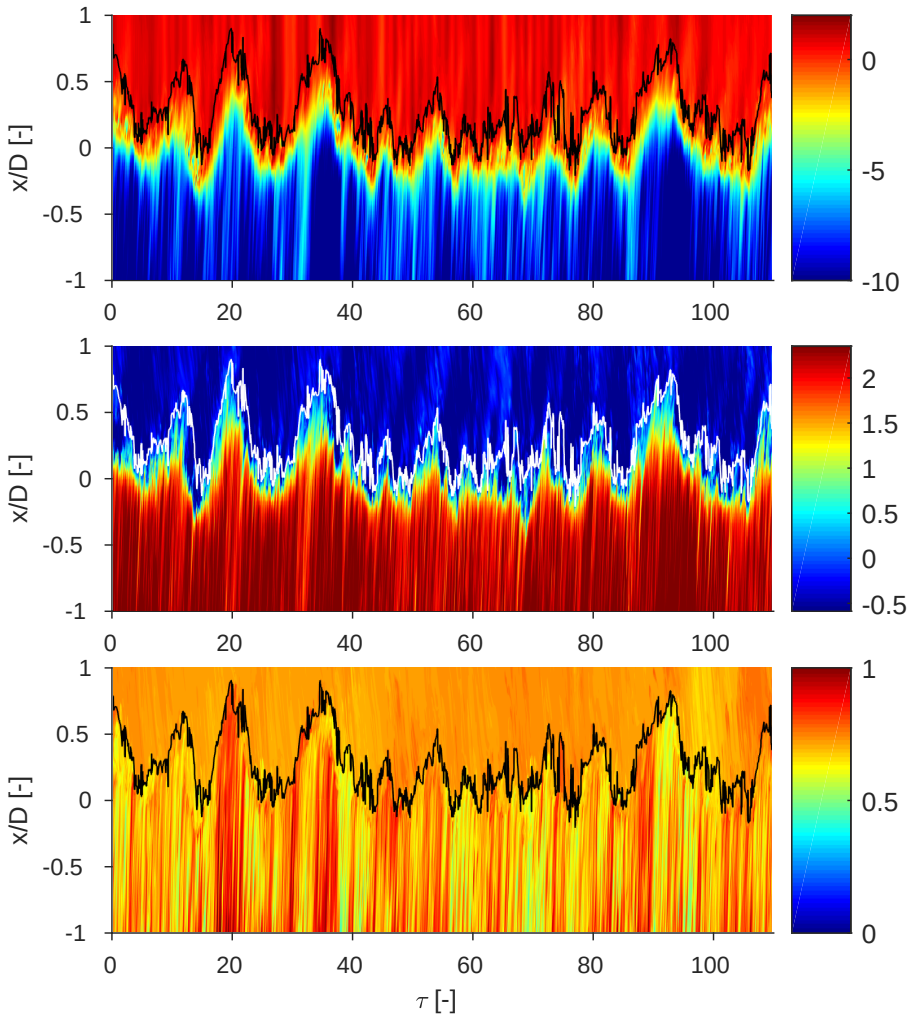

Figure 4.8: Pressure (top), axial velocity (middle) and mixture fraction (bottom) on the burner centre line over the simulation time, τ, combined with flame position represented by $\tilde{c} = 0.5$ (black or white line).

locity and location of FSP upstream the flame at $x/D = -0.5$ it is found that the frequency of fluctuations in pressure, velocity and FSP location coincides at two different St ($St \approx 0.1$ and $St \approx 0.19$) within the first dominant band of frequencies reported in Figure 4.6. This indicates that the coupling between axial velocity, pressure and FSP location provides the energy to the first dominant frequency band. To further analyse the dynamic motions of the flame, the swirl number, S, is introduced which measures the ratio of axial flux of

swirl momentum, G_ϕ, to the axial flux of the axial momentum, G_x [118]:

$$S = \frac{G_\phi}{RG_x} = \frac{\int_0^R \rho u_x u_t r^2 dr}{R \int_0^R \rho u_x^2 r dr} \tag{4.8}$$

The swirl number upstream the flame front at $x/D = -0.5$ is evaluated as a function of time along with the pressure drop over the flame and the location of the FSP and $\tilde{c} = 0.5$, Figure 4.9. The pressure drop is the difference be-

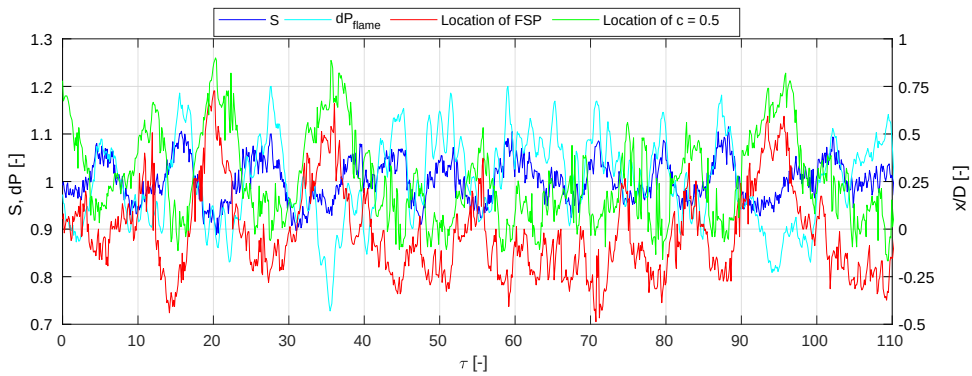

Figure 4.9: Temporal evolution of pressure, swirl number (left axis) and the axial location of FSP and $\tilde{c} = 0.5$ (right axis).

tween the area weighted pressure at $x/D = -0.5$ and the outlet pressure. The pressure drop over the flame and the swirl number are fluctuating perfectly in phase with each other whereas the location of the FSP and flame front are fluctuating with the same frequency but with a phase-shift of π compared to the pressure drop and swirl number. This shows a clear coupling between the fluctuating pressure field, the velocity field, the FSP and the flame location. The pressure drop is related to where the expansion (both thermal and geometrical) takes place relative to the burner exit. An expansion downstream of the burner exit results in lower pressure drop than an expansion upstream the burner exit. The local geometrical expansion and flame stabilization are associated with the local vortex structure. When the expansion reaches its most upstream position the pressure drop peaks and the flame cannot propagate further upstream due to a too high local flow speed, which will weaken the vortex break down due to less thermal expansion. The weaker vortex break down decreases the swirl number and the expansion and flame will propagate downstream. At the most downstream position the pressure drop and swirl number are low enough for the flame front to initiate a stronger interaction

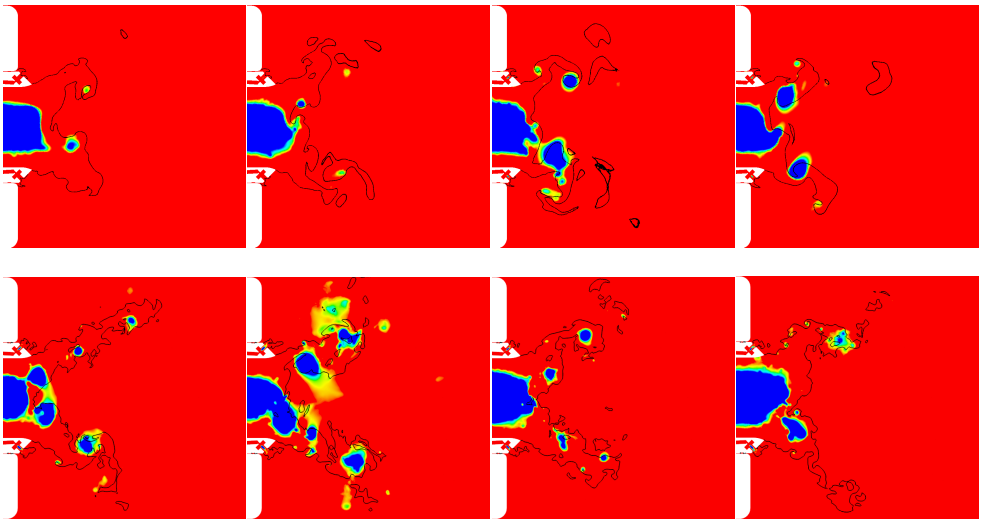

Figure 4.10: Pressure contour with iso-line of reaction progress variable of 0.5 for SAS (top) and LES (bottom).

with the vortex breakdown, with a movement of both the geometrical and thermal expansion towards the burner as a result.

The interaction between the PVC and the local flame front is investigated in **Paper II** and is shown in Figure 4.10 for both SAS and LES with a β PDF. The PVC is visualized as instantaneous low pressure zones and the flame is represented by an iso-line of reaction progress variable equal to 0.5. The local wrinkling of large flow scales, like the PVC, on the flame front is apparent in both the SAS and LES case whereas the local wrinkling of smaller flow scales are only seen in the LES, which is in line with **Paper III** where SAS is reported to dampen out much of the high frequency turbulence even though the grid and time step are identical. Both models show that the flame is stabilizing in the shear regions of the local vortex structures where the local flow velocity is equal to the local flame speed. Since the flame wrinkling is strongly connected to the PVC it is likely that the PVC may cause fluctuations in heat release with the same frequency as the precessing frequency of the PVC. The temporal evolution of the PVC in the LES β-PDF case is studied in **Paper V** where the pressure along two perpendicular lines, located at $x/D = 0.5$ in the combustion chamber, is visualized as a function of time Figure 4.11. The entire simulation time ($\tau = 0 - 110$) is shown to the left and a zoom in on ($\tau = 60 - 70$) is shown to the right. The PVC is seen as low pressure zones close to $y/D = 0.5$ and $z/D = 0.5$. It may be concluded that the time between them is not a fixed constant, i.e. the PVC is not rotating with a fixed

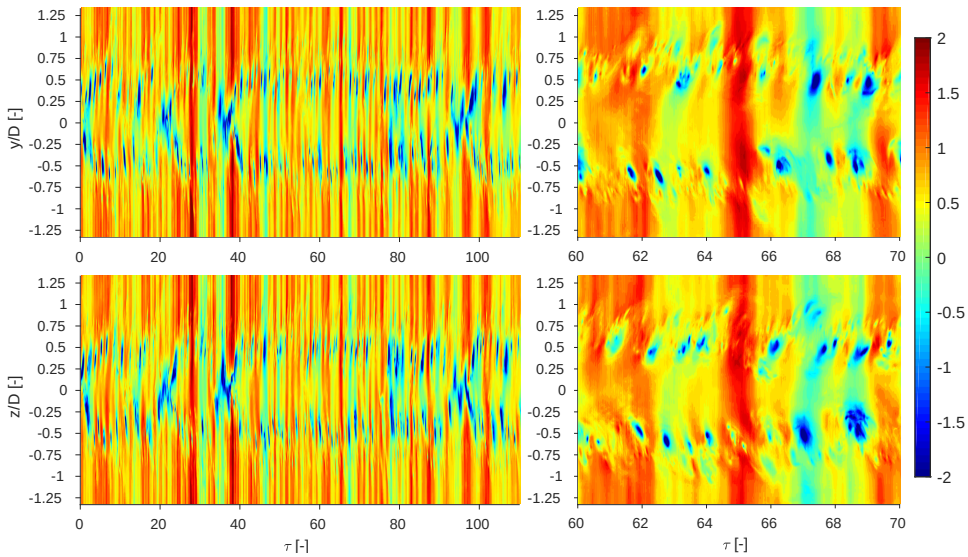

Figure 4.11: Pressure along two perpendicular radial lines, located at $x/D = 0.5$.

frequency, instead it is within a range of frequencies. In Figure 4.11 (right column) there are between 6-9 occurrences of PVC over a time span of 10τ corresponding to $0.6 < St < 0.9$, which coincides with the second dominant peak of pressure fluctuations in Figure 4.6. This gives a strong indication that the energy in the second dominant pressure mode is provided by the PVC into an acoustic mode that is within $0.62 < St < 0.71$. The first and second dominant pressure modes close to $St = 0.19$ and $St = 0.7$ shown in Figure 4.6 are visible from the vertical lines in Figure 4.11. The pressure fluctuation peaks occur simultaneously at all four tangential locations and have equal strength along the entire radial section. This shows that the first and second dominant pressure fluctuation bands are clearly axial modes where the pressure waves are moving in the direction of the burner centre axis, which is perfectly in line with the data presented in Figure 4.7. The first acoustic mode is triggered by the axial flame movement, Figure 4.9, whereas the second mode is triggered by the PVC. The third mode is not easily detected using this method due to its higher order nature, Figure 4.7, but it is likely that it is triggered by the general flame movements. To verify that the fluctuations reported in the LES are indeed interacting with the acoustics of the system, the RMS of pressure fluctuations on the combustion chamber wall are investigated in **Paper V** and shown here in Figure 4.12. The first dominant mode at $St \sim 0.19$ has its peak in the majority of the combustion chamber, Figure 4.7, which is seen in Figure 4.12 as pressure fluctuations close to 0.29 in the entire combustion chamber, with

the exclusion of the contraction. The second mode is clearly seen in Figure 4.12 with high pressure fluctuations in the most upstream and downstream part of the combustion chamber and low values in the middle. The third mode is also clearly seen in Figure 4.12 as high pressure fluctuations in two of the four most upstream corners of the combustion chamber, which is where the pressure fluctuation values reaches their maximum due to superposition of the three dominant modes. This clearly shows that the pressure fluctuations in the LES are indeed interactions between acoustics, flow and flame instabilities and not just flow and flame instabilities.

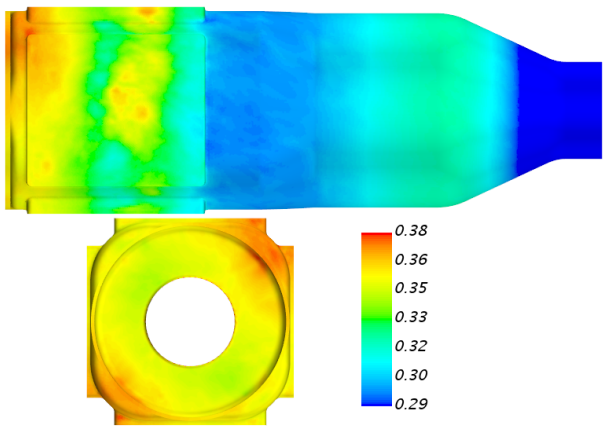

Figure 4.12: Fluctuation of pressure normalized by a reference pressure on combustion chamber walls.

Hydrogen enriched cases

In this section the effect of hydrogen enrichment is studied. An enrichment level of 80% by volume into methane is studied here. This part of the results is based on **Paper I**, **II** for the SAS cases and on un-published data for the hydrogen enriched LES cases. Increasing the amount of hydrogen in the methane/air mixture will increase the laminar flame speed and decrease the laminar flame thickness, Figure 2.1-2.2. The hydrogen enriched flame characteristics are shown in Figure 4.13 where OH-PLIF measurements are compared to numerical predictions using both SAS and LES. The OH-PLIF experiments are carried out with the same experimental set-up as in **Paper V**, keeping the same flame temperature and pilot flow split as in the methane case. OH-PLIF data reveals that the mean flame position is moving upstream towards the burner with a mean flame position on the centre line somewhere inside the burner.

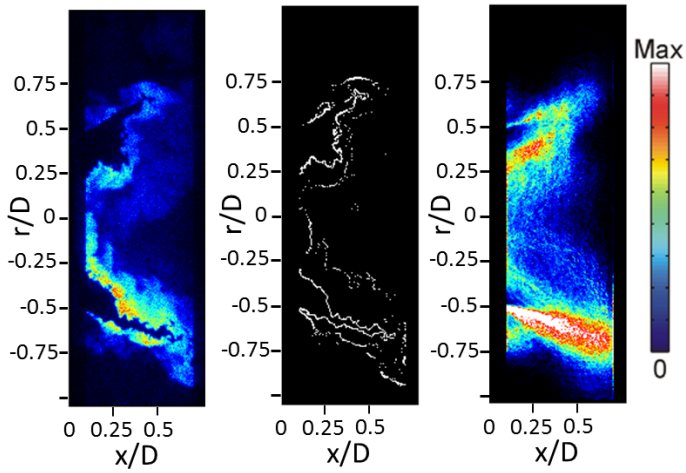

(a) OH-PLIF, instantaneous (left), instantaneous gradient (middle) and PDF of gradient (right)

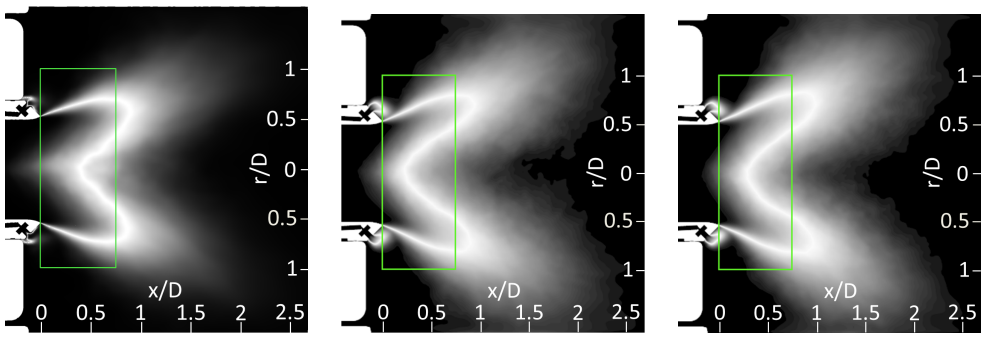

(b) SAS, 0%H2 (c) LES, δ-PDF, 0%H2 (d) LES, β-PDF, 0%H2

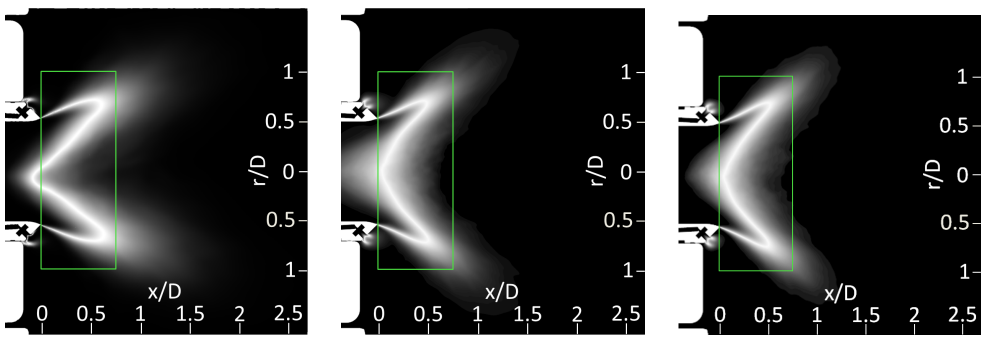

(e) SAS, 80%H2 (f) LES, δ-PDF, 80%H2 (g) LES, β-PDF, 80%H2

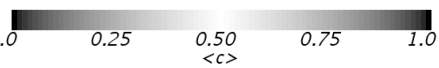

Figure 4.13: OH-PLIF data for 80% hydrogen enrichment and time averaged reaction progress variable for methane and 80% hydrogen enrichment.

It can also be interpreted from the PDF of the OH-PLIF gradient that it is not likely that the flame is moving downstream of $x/D = 0.5$. All numerical models predict a more compact flame, which is due to the increased reactivity of hydrogen. All three numerical models also predict a movement of the centre line stabilization point towards the burner exit, where the largest flame movement is predicted by the SAS-flamelet model. The most upstream flame location does not change significantly in the SAS predictions, instead only the flame width decreases whereas in the two LES cases the most upstream flame location is moving upstream into the burner. How far upstream the flame is stabilising in the experiments is very difficult to interpret since the laser sheet is downstream of the burner. However, instantaneous OH-PLIF frames indicated that the flame might be instantaneously stabilized very far upstream, judged from its appearance in the combustion chamber. The pilot shape in the LES cases is different with and without hydrogen enrichment. An O-shaped flame is found in the pure methane case, whereas an M-shaped flame is predicted in the hydrogen enriched cases. The same behaviour is observed regardless of the PDF shape used. The change in pilot flame shape is most likely an effect of the higher laminar flame speed associated with the hydrogen enrichment. This shows that the pilot flame shape is dependent on the local reaction rate and may change shape when the reaction rate is increased, which may be achieved either by changing the fuel or by increasing the pilot fuel ratio. From temperature predictions in the pilot flame region it is observed that the temperature is increasing with hydrogen enrichment, even though the pilot fuel split is the same. This may be related to the local pressure drop across the pilot flame, which is increasing when the flame stabilizes and even attaches close to the burner hardware. Increasing the pressure drop across the pilot flame will move air from the pilot to the main flame, which in turn will increase the local temperature. The predicted pressure drop from the inlet plenum to the combustion chamber for both the experiment and the CFD predictions are summarized in Figure 4.14. All pressure drops are normalized by the experimental pressure drop using pure natural gas. The SAS model predicts pressure drops close to the value obtained in the rig. The prediction on natural gas is very close and the hydrogen pressure drop is somewhat over predicted. The LES with a β-PDF consistently over-predicts the pressure drop by 2-3% in both the methane case and the hydrogen enriched case, showing that the effect of hydrogen is very well captured. The LES with a δ-PDF gives a too high pressure drop using methane and under-predicts the pressure drop using hydrogen enriched methane. The relative increase in pressure drop due to hydrogen enrichment in this case is under-predicted, which gives an indication that the β shaped PDF captures the physics better than the δ shaped PDF.

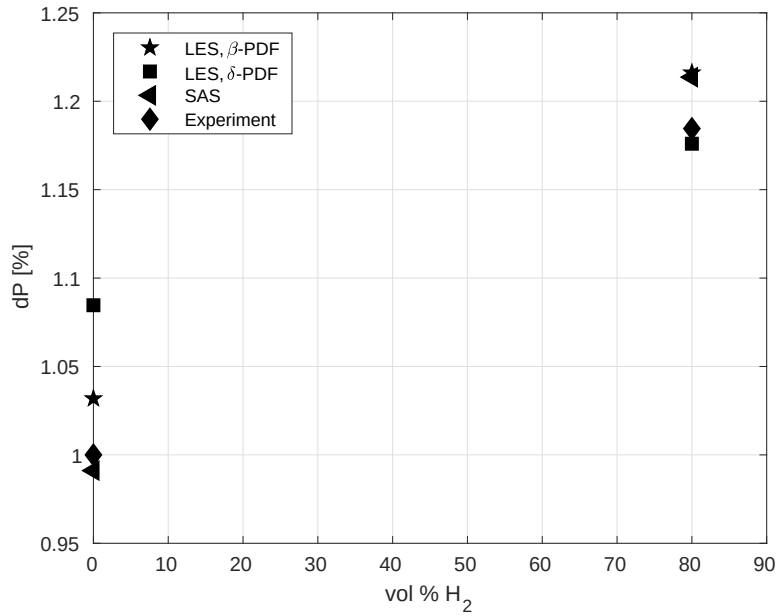

Figure 4.14: Pressure drop as function of hydrogen enrichment level.

4.4.2 High Pressure Cases

The effect of pressure and hydrogen enrichment at engine pressure is investigated in **Paper IV**. A qualitative overview of the three different flow cases is presented in Figure 4.15. Here the time average of axial velocity and temperature (upper half of figures) along with their time averaged fluctuations (lower part of figures) are shown in the burner centre plane. Quantitative data along the centre line is visualised in Figure 4.16. All three flow cases show a high axial velocity close to the burner centre line with the highest value just upstream the mixing tube close to $x/D = -2.4$ followed by a slow decay until $x/D \approx 0$ where the forward stagnation point is located on a time averaged basis. The decay in axial velocity along the centre line is due to radial pressure gradient present in the swirling flow. The increase in flow velocity for the hydrogen enriched case relative to the high pressure methane case is due to the increased volumetric fuel flow rate. All three cases also show a clear re-circulation zone featured by a negative axial velocity downstream of the burner exit at $x/D = 0$. The appearance of the re-circulation zone differs between the pure methane cases and the hydrogen diluted case. Both methane cases show a local minimum in axial velocity which is not seen in the hydrogen enriched case where the axial velocity is steadily decreasing from the start of

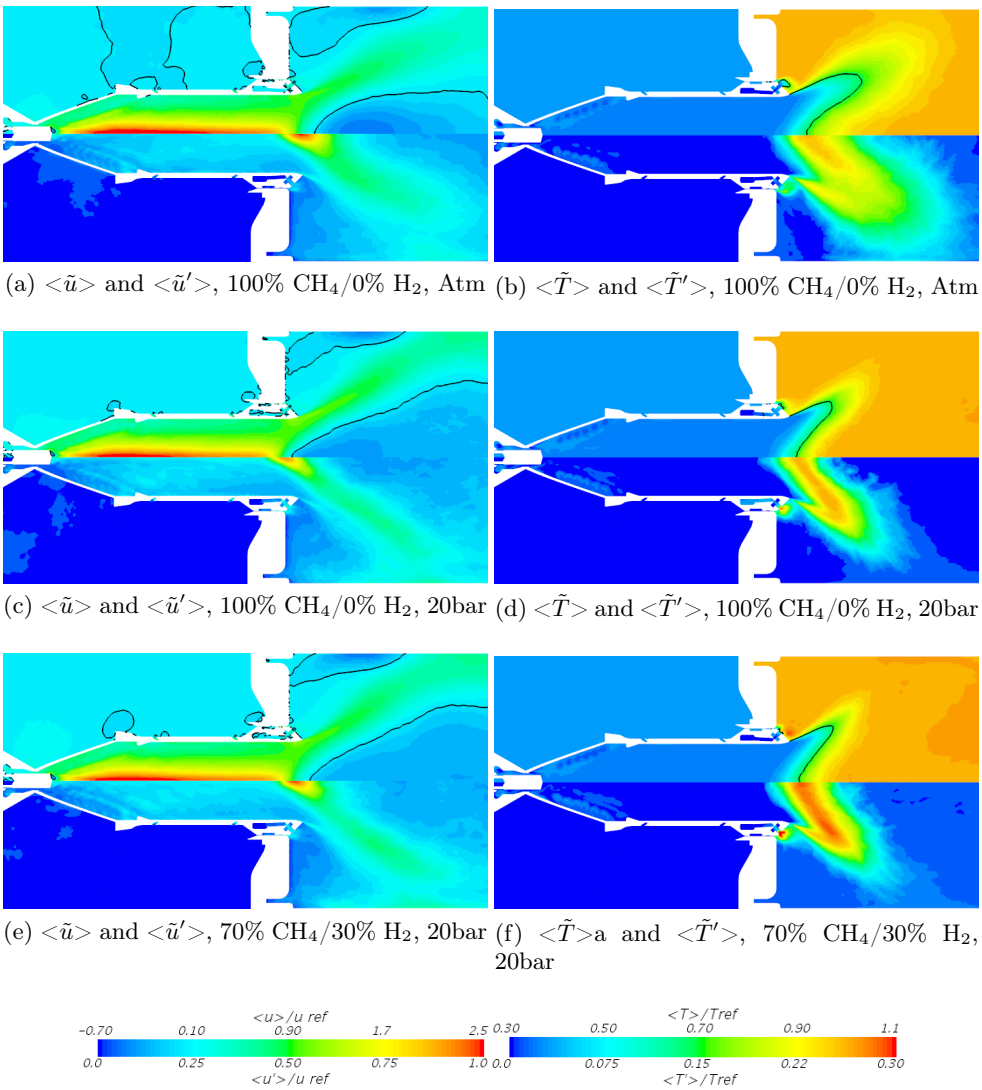

(a) $<\tilde{u}>$ and $<\tilde{u}'>$, 100% CH_4/0% H_2, Atm (b) $<\tilde{T}>$ and $<\tilde{T}'>$, 100% CH_4/0% H_2, Atm

(c) $<\tilde{u}>$ and $<\tilde{u}'>$, 100% CH_4/0% H_2, 20bar (d) $<\tilde{T}>$ and $<\tilde{T}'>$, 100% CH_4/0% H_2, 20bar

(e) $<\tilde{u}>$ and $<\tilde{u}'>$, 70% CH_4/30% H_2, 20bar (f) $<\tilde{T}>$a and $<\tilde{T}'>$, 70% CH_4/30% H_2, 20bar

Figure 4.15: Time average (upper half of figures) and RMS of fluctuation (lower half of figures) of axial velocity (left column) and temperature (right column) for all flow cases. Iso-line shows zero time averaged axial velocity (left column) and time averaged progress variable of 0.5 (right column).

the forward stagnation point at $x/D = 0$ and two burner diameters into the combustion chamber. The axial velocity RMS fluctuations are also similar between the three flow cases. The RMS fluctuations are generally low close to the swirler walls and rather even throughout the entire mixing tube with

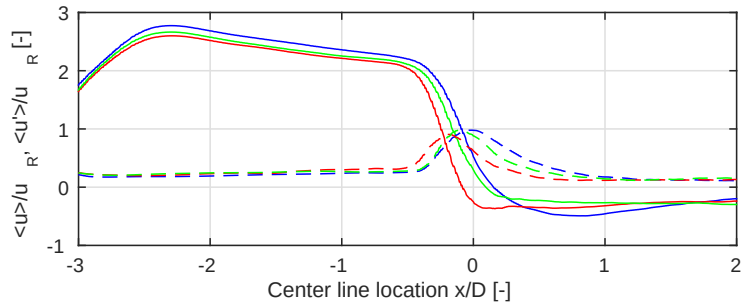

(a) Axial velocity

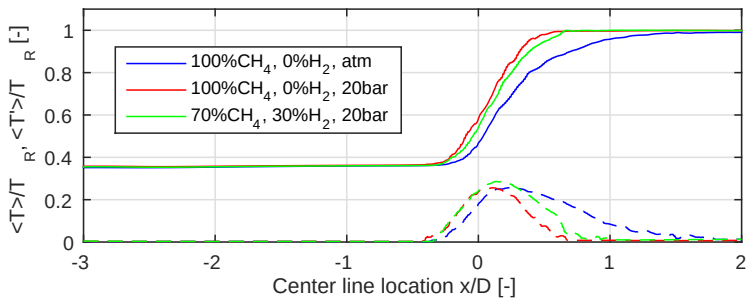

(b) Temperature

Figure 4.16: Normalized axial velocity and temperature along the burner centre line where solid lines are mean values and dashed lines are fluctuations.

a ground level of $< u' > /u_r = 0.25$ which is due to turbulent fluctuations. The time averaged temperature reveals that the main flame is M-shaped in all three cases, with an upstream stabilization point close to $x/D = -0.3$ in all three cases. The atmospheric case show a flame with a high volume whereas the two pressurized cases show more compact flames. The outer shear layer of the M-shaped flame is stabilized by the pilot flames, which provides heat to the outer re-circulation zone outside of the flame. In the hydrogen case, the pilot produces higher temperatures than the methane cases, even though the pilot fuel ratio is kept constant. This is a local effect of fuel air mixing in the pilot flame region where a part of the combustion air is injected to mix with the pilot fuel. One major difference between the atmospheric case and the pressurized cases is the time averaged shape of the pilot flame. From the isoline of $< \tilde{c} >= 0.5$ it is revealed that in the atmospheric case the pilot flame is O-shaped and in the high pressure cases it is M-shaped, which is very similar to observations in the hydrogen enriched atmospheric cases. This change in pilot flame shape will play an important role in the pilot flame stabilization and its interaction with the main flow, which will be discussed later. Studying the temperature field close to the swirler walls there are clear traces of the

discrete fuel injection points in the swirler where the cold fuel is injected into the pre-heated air stream. The RMS fluctuations of temperature show non-zero values close to the fuel injection region and close to the flame region. The non-zero values in the fuel injection region is due to the unsteady nature of the jet in cross-flow fuel injection arrangement [44,45]. The non-zero values in the flame region is due to the movements of the unsteady flame. The RMS of temperature fluctuations show that the flames are spatially stabilizing between $-0.4 < x/D < 0.75$ in the pressurized cases and between $-0.3 < x/D < 1.5$ in the atmospheric case. The shape of the RMS temperature in the flame region is very similar between the two high pressure cases but the peak value is higher in the hydrogen enriched case. The local flame stabilization point is dependent on the local flow speed and the local turbulent burning velocity. The laminar flame speed is decreasing with an increasing pressure at the same conditions (Figure 2.1) but the turbulent flame speed is increasing with an increasing pressure [141], which, combined with a higher power density in the high pressure cases, makes the high pressure flames stabilize further upstream than the atmospheric flame. In the hydrogen enriched case the flame stabilization point will be affected by both the increased flow velocity and velocity fluctuations upstream the flame as well as the increase in laminar flame speed associated with hydrogen enrichment of 30%. In **Paper IV** it is concluded that the difference in flame speed between methane and methane enriched by 30% hydrogen is much less pronounced at high pressures than at atmospheric conditions. This could be one reason for the lack of axial movement of the flame due to hydrogen enrichment.

The fluctuating pressure in the high pressure cases is monitored at the location of the pressure transducer, as shown in Figure 4.2 and is compared to the atmospheric case in Figure 4.17. In the pressure trace of the pressurized cases it is observed that the pressure peak values are in the order of 25-30 times higher than the atmospheric pressure peaks which is due to the factor of 20 increase of pressure and thermal power. The pressure peaks are found at the same dominant Strouhal numbers as in the atmospheric case. For the high pressure cases the mode at $St = 0.67$ is the most dominant one with a peak value 150 times higher than the maximum peak value from the atmospheric case. The time signal also reveals that both high pressure cases becomes unstable after approximately $\tau > 30$ with pressure peak values increasing at each instability cycle as a result. Transient data was analysed to find if the reason for this instability is interaction between flame and PVC or if other features of the system is involved. The PVC is still present in the high pressure cases but it does not seem to cause the change from stable to unstable combustion. Instead, it appears that the transition from stable combustion to unstable combustion is due to pilot flame interactions with the acoustic mode at $St = 0.67$. The pressure of the combustor centre plane during one $St = 0.67$

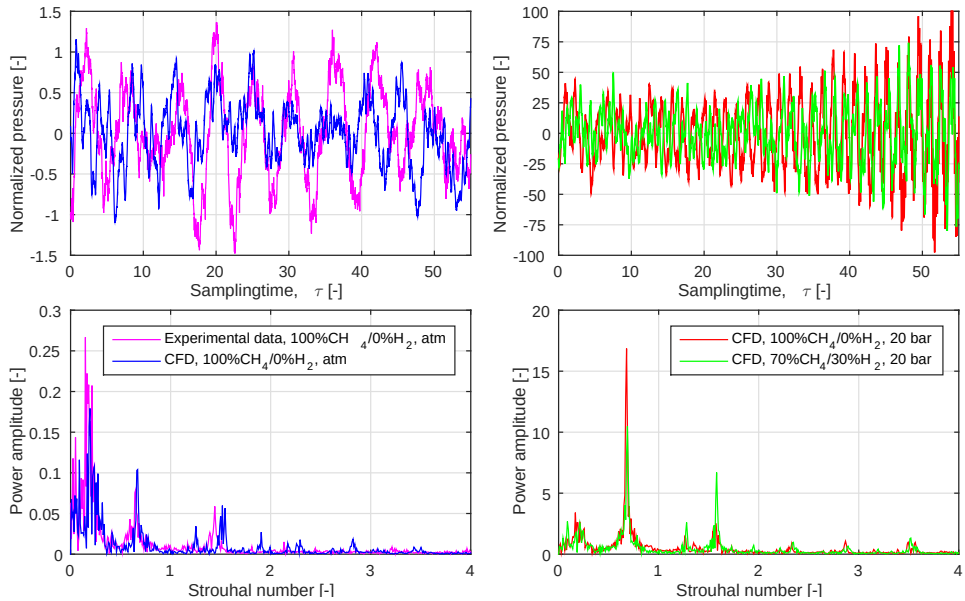

Figure 4.17: Pressure sampled at the pressure transducer location.

cycle is shown in Figure 4.18 along with iso-volumes of temperatures above $T/T_{ref} = 1.16$ and the time instance location on the pressure trace. The appearance of the pressure fluctuation is in very good agreement with the acoustic pressure mode close to $St = 0.67$ reported in Figure 4.7. Here it is clearly seen that when the pressure peak is located close to the upstream part of the combustion chamber, the pilot flames generate large zones of high temperatures. When the pressure peak is located close to the combustion chamber exit, no high temperature zones are seen close to the pilot flame region. This feedback cycle makes the pilot flames and thereby its heat release fluctuate in perfect phase with the acoustic fluctuations, which may generate the growth instability. This coupling might be due to the fact that the pilot flames are premixed. The pressure drop across the pilot air feed is the same as across the burner whereas the pilot fuel is feed separately. Fluctuations in pressure at the pilot outlet will lead to fluctuations in mixture fraction and thereby in heat release. The coupling between pilot flame fluctuations and acoustic instabilities are not observed for the first half of the simulation. The instabilities are most likely initiated from the PVC and flame interaction and becomes unstable when the pilot heat release starts to fluctuate in phase with the pressure.

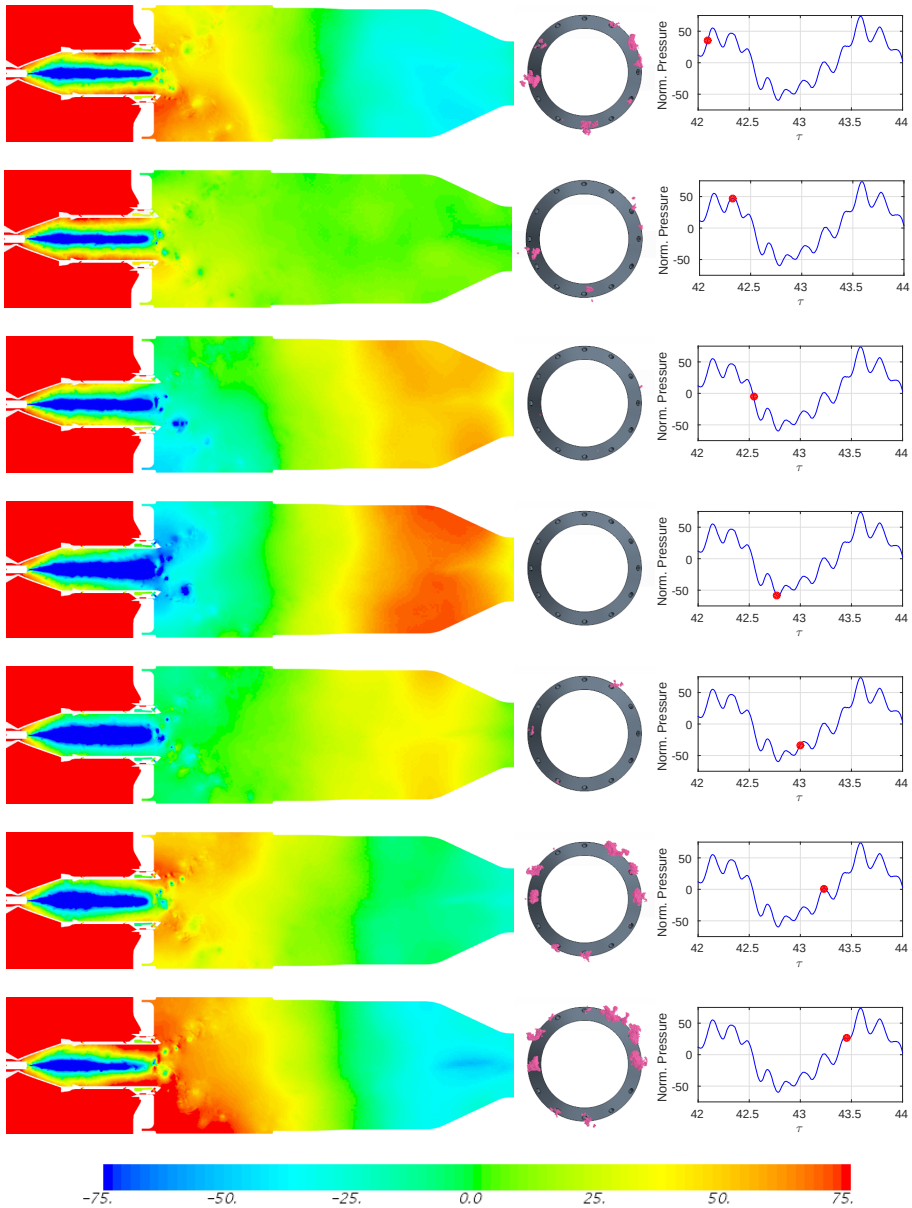

Figure 4.18: Time series of the $St = 0.67$ pressure mode in the pure methane 20 bar case with centre plane pressure normalized by a reference value (left column), burner tip surface combined with isovolume of $T/T_{ref} > 1.16$ (middle column), and instance of time combined with location on pressure trace at the location of the pressure transducer (right column).

5 | Summary of Publications

Paper I

The effects of hydrogen enrichment in the SGT-800 3^{rd} generation DLE burner fitted in an atmospheric combustion rig have been numerically investigated using three different levels of hydrogen enrichment. Reynolds Averaged Simulations (RAS) and Scale Adaptive Simulations (SAS) are applied with different mean reaction rate constant to the methane case where it is shown that no change in flame shape and position is observed using RAS, making it unsuitable for hydrogen enrichment predictions. The SAS model accurately predicts the flame movement and increase in pressure drop over the burner due to hydrogen enrichment.

The simulations were planned by the candidate and the co-authors. The candidate did all the simulations and post processing of the simulations. The candidate wrote the paper with input from the co-authors

Paper II

This paper presents a numerical study of the Siemens 3^{rd} generation DLE burner where both RAS and SAS combined with a flamelet model are used on different grids and with both methane and methane enriched by 80% hydrogen. The mean reaction rate is modelled through an algebraic fractal relationship. The work shows how the flame front is interacting with the local flow structure and that the SAS model is capable of predicting some part of the flame dynamics.

The simulations were planned by the candidate and the co-authors. The candidate did all the simulations and post processing of the simulations. The candidate wrote the paper with input from the co-authors

Paper III

In this paper the mixing capabilities of the Siemens 3^{rd} generation DLE burner is experimentally and numerically investigated. RAS, SAS and LES are applied on different grids and compared against experimental data and against each other. The RAS predictions generally fails to accurately capture the physics of the mixing. The scale resolving methods both predicts the mixing well, where the LES gives the best representation of the mixing since the SAS model is dampening out higher flow and mixing frequencies.

The simulations were planned by the candidate, D. lörstad and X.-S. Bai. The candidate did all the simulations and post processing of the simulations. The candidate co-supervised the student who did the experimental work and planned the experimental work with A. Lindholm and D. Lörstad. The experimental work was carried out by D. Christensen. The candidate wrote the paper with input from the co-authors

Paper IV

This paper explores the effect of high pressure and hydrogen enrichment at high pressure. LES is used combined with the Flamelet Generated Manifold (FGM) approach. The flame is more compact at high pressure due to the increased power density. Hydrogen addition by 30% at high pressure has only a marginal effect on the flame shape and position, which is partially due to the fact that different kinetics is dominant at atmospheric and high pressure. A dominant thermoacoustic frequency at Strouhal number of $St = 0.67$ is reported, which is an interaction between an acoustic combustion chamber mode and the pilot flames.

The simulations were planned by the candidate and the co-authors. The candidate did all the simulations and post processing of the simulations. The candidate wrote the paper with input from the co-authors

Paper V

This paper explored the flame dynamics and the thermoacoustic behaviour of the siemens 3^{rd} generation DLE burner. Experimental and numerical methods are used jointly to identify the dominant pressure fluctuation frequencies, their mode shape and why they are triggered. LES combined with FGM is fully capable of predicting the thermoacoustic behaviour of the combustion system without any model adjustments, making it suitable for deeper investigations of existing hardware and predictions of newly developed hardware where experimental data does not exist.

The CFD simulations were planned by the candidate, D. lörstad and X.-S. Bai. The candidate did all the CFD simulations and post processing of the simulations. The candidate planned the Helmholtz simulations together with K. Bengtsson and D. Lörstad. The helmholtz predictions were performed by K. Bengtsson and the experiments were performed by A. Lantz and A. Lindholm. The candidate wrote the paper with input from the co-authors

6 | Conclusions

In this thesis a real gas turbine burner has been studied using scale resolving turbulence models combined with flamelet type combustion models. Atmospheric and engine pressure methane/air and methane/hydrogen/air flames are investigated and compared against experimental data. The methods are validated and used for increasing the detailed understanding of the flame stabilization process in the Siemens 3^{rd} generation DLE burner. The main findings in this thesis are:

- Both the SAS and LES methodology are capable of predicting a good representation of the methane flame, both in terms of flame shape, position and movement. This shows that the flamelet type combustion models are applicable to flames with Ka numbers in the order of 100.

- Non-scale resolving methods are not capable of predicting a change in flame position when changing the reactivity of the fuel. Scale resolving methods does a good job in predicting the change in flame shape and position when hydrogen is added to the methane based fuel mixture.

- The SAS-flamelet model needed some adjustments of the reaction rate model constant, which is believed to be dependent on both the burner geometry an pressure level, which makes it less useful for predictions of new configurations but still useful for evaluation of known systems. The LES-FGM model did not need any model adjustments which makes it suitable for detailed analysis of both existing and new combustion systems. The SAS model also tends to dampen out more high frequency dynamics than the LES model on similar sized grids which has an effect on the fuel and air mixing predictions and most likely the interactions between flow and flame.

- The thermoacoustic instabilities in the system is well predicted using the LES-FGM model, both in terms of frequency and amplitude. This work also shows that the predicted fluctuations are indeed interaction between flow dynamics, flame dynamics and acoustics.

- Hydrogen enrichment by 80% at atmospheric conditions moves the flame upstream towards the burner and increases the burner pressure drop. Both the movement in flame stabilization position and the increased pressure drop is well captured by both the SAS and LES models. Hydrogen enrichment by 30% at high pressure conditions is less pronounced due to a change in reaction pathways when moving from atmospheric conditions to high pressure conditions.

It should be pointed out that only RAS models based on the Boussinesq assumptions for the turbulence and gradient diffusion type closures for for the scalar fluxes have been considered. There is a possibility that the usage of Reynolds stress models combined with second moment closures for the scalar fluxes would improve the predictive capabilities of the RAS models. It should also be pointed out that unity Lewis number is assumed throughout this thesis. Here it is assumed the differential diffusion effects are of minor importance in high Reynolds number and high Karlovitz number flows, but this statement is hard to prove due to lack of experimental data.

6.1 Future Work

- Adopt the methodology to an engine gas turbine combustion chamber with secondary air passages present.
- Study higher levels of hydrogen enrichment in high pressure flames to investigate flashback resistance and flashback mechanisms in the investigated burner.
- Investigate the possibility to include differential diffusion effects in the hydrogen enriched simulations.

Bibliography

[1] *CFX theory manual 14.5*. http://www.ansys.com.

[2] *CFX theory manual 17.2*. http://www.ansys.com.

[3] *StarCCM+ theory manual*. https://mdx.plm.automation.siemens.com/star-ccm-plus.

[4] Aluri, N. K., Muppala, S. P. R., and Dinkelacker, F. Substatiating a fractal-based algebraic reaction closure of premixed turbulente combustion for high pressure and the lewis number effects. *Combustion and Flame 145* (2006), 663–674.

[5] Ansari, N., Strakey, P. A., Goldin, G. M., and Givi, P. Filtered density function simulation of a realistic swirled combustor. *Proceedings of the Combustion Institute 35* (2015), 1433–1442.

[6] Aspden, A. J., Day, M. S., and Bell, J. B. Turbulence-flame interactions in lean premixed hydrogen: transition to the distributed burning regime. *Journal of Fluid Mechanics 680* (2011), 287–320.

[7] Bilger, R. W., Stårner, S. H., and Kee, R. J. On reduced mechanism for methane/air combustion in nonpremixed flames. *Combustion and Flame 80* (1990), 135–149.

[8] Boger, M., Veynante, D., Boughanem, H., and Trouvé, A. Direct numerical simulation analysis of flame surface density concept for large eddy simulation of turbulent premixed combustion. *Proceedings of the Combustion Institute 27* (1998), 917–925.

[9] Boudier, G., Gicquel, L. Y. M., Poinsot, T., Bissières, D., and Bérat, C. Comparison of LES, RANS and experiments in an aeronautical gas turbine combustion chamber. *Proceedings of the Combustion Institute 31* (2007), 3075–3082.

[10] Boudier, G., Gicquel, L. Y. M., and Poinsot, T. J. Effects of mesh resolution on large eddy simulation of reacting flows in complex geometry combustors. *Combustion and Flame 155* (2008), 196–214.

[11] Bradley, D. How fast can we burn. *Proceedings of the Combustion Institute 24* (1992), 247–262.

[12] Bradley, D., Lau, A. K. C., and Lawes, M. Flame stretch rate as a determination of turbulent burning velocity. *Philosophical Transactions of the Royal Society of London 338* (1992), 339–359.

[13] Bray, K. N. C. The interaction between turbulence and combustion. *Proceedings of the Combustion Institute 17* (1979), 223–233.

[14] Bray, K. N. C. Studies of the turbulent burning velocity. *Proceedings of the Royal Society of London 431* (1990), 315–335.

[15] Bray, K. N. C., Libby, P. A., and Moss, J. B. Unified modeling approach for premixed turbulent combustion-Part I: general formulation. *Combustion and Flame 61* (1985), 87–102.

[16] Bulat, G. *Large eddy simulations of reacting swirling flows in an industrial burner*. PhD thesis, Imperial College London, 2012.

[17] Bulat, G., Fedina, E., Fureby, C., Meier, W., and Stopper, U. Reacting flow in an industrial gas turbine combustor: LES and experimental analysis. *Proceedings of the Combustion Institute 35* (2014), 3175–3183.

[18] Bulat, G., Jones, W. P., and Marquis, A. J. Large Eddy Simulation of an industrial gas-turbine combustion chamber using the sub-grid PDF method. *Proceedings of the Combustion Institute 34*, 2 (2013), 3155–3164.

[19] Bulat, G., Jones, W. P., and Marquis, A. J. NO and CO formation in an industrial gas-turbine combustion chamber using LES with the eulerian sub-grid PDF method. *Combustion and Flame 161* (2014), 1804–1825.

[20] Carlsson, H. *Detailed numerical simulations of turbulent premixed flames at moderate and high karlovitz numbers*. PhD thesis, Lund University, 2014.

[21] Carlsson, H., Carlsson, C., Fuchs, L., and Bai, X. S. Large eddy simulation and extended dynamic mode decomposition of flow-flame interaction in a lean premixed low swirl burner. *Flow, Turbulence and Combustion 93* (2014), 505–519.

[22] Carlsson, H., Nordström, E., Bohlin, A., Petersson, P., Wu, Y., Collin, R., Aldén, M., Bengtsson, P., and Bai, X. S. Large eddy simulations and rotational CARS/PIV/PLIF measurements of a lean premixed low swirl stabilized flame. *Combustion and Flame 161* (2014), 2534–2551.

[23] Carlsson, H., Yu, R., and Bai, X.-S. Flame structure analysis for categorization of lean premixed CH4/air and H2/air flames at high Karlovitz numbers: Direct numerical simulation studies. *Proceedings of the Combustion Institute 35* (2015), 1425–1432.

[24] Charlette, F., Meneveau, C., and Veynante, D. A power-law flame wrinkling model for LES of premixed turbulent combustion Part I: non-dynamic formulationand initial tests. *Combustion and Flame 131* (2002), 159–180.

[25] Charlette, F., Meneveau, C., and Veynante, D. A power-law flame wrinkling model for LES of premixed turbulent combustion Part II: dynamic formulation. *Combustion and Flame 131* (2002), 181–197.

[26] Chen, Y., and Ihme, M. Large-eddy simulation of a pilotet premixed jet burner. *Combustion and Flame 160* (2013), 2896–2910.

[27] Colin, O., Ducros, F., Veynante, D., and Poinsot, T. A thickened flame model for large eddy simulation of turbulent premixed combustion. *Physics of Fluids 12* (2000), 1843–1863.

[28] Donini, A., Bastiaans, R. J. M., van Oijen, J. A., and de Goey, L. P. H. Differential diffusion effects inclusion with flamelet generated manifold for the modeling of stratified premixed cooled flames. *Proceedings of the Combustion Institute 35* (2015), 831–837.

[29] Donini, A., Bastiaans, R. J. M., van Oijen, J. A., and de Goey, L. P. H. A 5-d implementation of FGM for the large eddy simulation of a stratified swirled flame with heat loss in a gas turbine combustor. *Flow, Turbulence and Combustion 98* (2017), 887–922.

[30] Dopazo, C. Probability density function approach for a turbulent axisymmetric heated jet. centerline evolution. *The Physics of Fluids 18* (1975), 397–.

[31] Driscoll, J. F. Turbulent premxed combustion: Flamelet structure and its effect on turbuelnt burning velocities. *Progress in Energy and Combustion Science 34* (2008), 91–134.

[32] Elkady, A. M., Kalitan, D. M., Hebon, J., Leonard, G., Akula, R., Karim, H., and Hadley, M. Gas turbine emission characteristics in perfectly premixed combustion. In *GT2011-46470, ASME Turbo Expo* (2011).

[33] Ertesvåg, I. S., and Magnussen, B. F. The eddy dissipation turbulence energy cascade model. *Combustion Science and Technology 159* (2000), 213–236.

[34] Fairweather, M., Ormsby, M. P., Sheppard, C. G. W., and Woolley, R. Turbulent burning rates of methane and methane-hydrogen mixtures. *Combustion and Flame 156* (2009), 780–790.

[35] Fedina, E., Fureby, C., Bulat, G., and Meier, W. Assessment of finite rate chemistry large eddy simulation combustion models. *Flow, Turbulence and Combustion 99* (2017), 385–409.

[36] Fiorina, B., Vicquelin, R., Auzillon, P., Darabiha, N., Giquel, O., and Veynante, D. A filtered tabulated chemistry model for LES of premixed combustion. *Combustion and Flame 157* (2010), 465–475.

[37] Frenklach, F., Wang, H., Yu, C. L., Goldenberg, M., Bowman, C. T., Hanson, R. K., Davidson, D. F., Chang, E. J., Smith, G. P., Golden, D. M., Gardiner, W. C., and Lissianski, V. `http://www.me.berkely.edu/gri_mech`.

[38] Fric, T. F. Effects of fuel-air unmixedness on NO(x) emissions. *Journal of Propulsion and Power 9*, 5 (1993), 708–713.

[39] Fureby, C. A fractal flame-wrinkling large eddy simulation model for premixed turbulent combustion. *Proceedings of the Combustion Institute 30* (2005), 593–601.

[40] Gicquel, L. Y. M., Staffelbach, G., and Poinsot, T. Large eddy simulations of gaseous flames in gas turbine combustion chambers. *Progress in Energy and Combustion Science 38* (2012), 782–817.

[41] Goldin, G., and Zhang, Y. A generalized FGM progress variable weight optimization using heeds. In *GT2017-64446, ASME Turbo Expo* (2017).

[42] Goodwin, D. G., Moffat, H. K., and Speth, R. L. Cantera: An object-oriented software toolkit for chemical kinetics, thermodynamics, and transport processes. `http://www.cantera.org`, 2016. Version 2.2.1.

[43] Gouldin, F. C. An application of fractals to modeling premixed turbulent flames. *Combustion and Flame 68* (1987), 249–266.

[44] Grout, R. W., Gruber, A., Kolla, H., Bremer, P.-T., Bennett, J. C., Gyulassy, A., and Chen, J. H. A direct numerical simulation study of turbulence and flame structure in transverse jets analysed in jet-trajectory based coordinates. *Journal of Fluid Mechanics 706* (2012), 351–383.

[45] Grout, R. W., Gruber, A., Yoo, C. S., and Chen, J. H. Direct numerical simulation of flame stabilization downstream of a transverse fuel jet in cross-flow. *Proceedings of the Combustion Institute 33* (2011), 1629–1637.

[46] Haworth, D. C. Progress in probability density function methods for turbulent reacting flows. *Progress in Energy and Combustion Science 36* (2010), 168–259.

[47] Huang, Y., and Yang, V. Dynamics and stability of lean-premixed swirl-stabilized combustion. *Progress in Energy and Combustion Science 35* (2009), 293–364.

[48] Ihme, M., Cha, C. M., and Pitsch, H. Prediction of local extinction and re-ignition effects in non-premixed turbulent combumbustion using a flamelet/progress variable approach. *Proceedings of the Combustion Institute 30* (2005), 793–800.

[49] Ihme, M., and Pitsch, H. Prediction of extinction and reignition in nonpremixed turbulent flames using a flameley/progress variable model 1. a priori srudy and presumed PDFclosure. *Combustion and Flame 155* (2008), 70–89.

[50] Ihme, M., Shunn, L., and Zhang, J. Regularization of reaction progress variable for application to flamelet-based combustion models. *Journal of Computational Physics 231* (2012), 7715–7721.

[51] International Energy Agency. *Energy and Air Pollution*, 2016. `www.iea.org`.

[52] International Energy Agency. *World Energy Outlook*, 2017. `www.iea.org/weo2017`.

[53] Jangi, M., and Bai, X. S. Multidimensional chemistry coordinate mapping approach for combustion modelling with finite-rate chemistry. *Combustion Theory and Modelling 16* (2012), 1109–1132.

[54] Jangi, M., Yu, R., and Bai, X. S. A multi-zone chemistry mapping approach for direct numerical simulation of auto-ignition and flame propagation in a constant volume enclosure. *Combustion Theory and Modelling 16* (2012), 221–249.

[55] Jangi, M., Zhao, X., Haworth, D. C., and Bai, X.-S. Stabilization and liftoff length of a non-premixed methane/air jet flame discharging into a high-temperature environment: An accelerated transported pdf method. *Combustion and Flame 162* (2015), 408–419.

[56] Janicka, J., Kolbe, W., and Kollmann, W. Closure of the transport equation for the probability density function of turbulent scalar fields. *Journal of Non-Equilibrium Thermodynamics 4* (1977), 47–66.

[57] Janicka, J., and Kollmann, W. A two-variables formalism for the treatment of chemical reactions in turbulent H2-air diffusion flames. *Proceedings of the Combustion Institute 17* (1978), 421–430.

[58] Jones, W. P. *Models for turbulent flows with variable density and combustion.* VKI-Lecture Series, Hemisphere. 1980, ch. Predictive Methods for Turbulent Flows, pp. 379–421.

[59] Jones, W. P., and Launder, B. E. The prediction of laminarization with a two-equation model of turbulence. *International Journal of Heat and Mass Transfer 15* (1972), 301–314.

[60] Jones, W. P., Marquis, A. J., and Prasad, V. N. Les of a turbulent premixed swirl burner using eulerian stochastic field method. *Combustion and Flame 159* (2012), 3079–3095.

[61] Jones, W. P., Marquis, A. J., and Vogiatzaki, K. Large-eddy simulation of spray combustion in a gas turbine combustor. *Combustion and Flame 161* (2014), 222–239.

[62] Jones, W. P., and Pascau, A. Calculations of confined swirling flows with a second moment closure. *Journal of Fluids Engineering 111* (1989), 248–255.

[63] Kemenov, K. A., and Pope, S. B. Molecular diffusion effects in les of a piloted methane-air flame. *Combustion and Flame 158* (2011), 240–254.

[64] Kim, W., and Menon, S. A new dynamic one-equation subgrid-scale model for large eddy simulation. *In 33rd Aerospace Sciences Meeting and Exhibit, Reno, NV* (1995).

[65] Kim, W. W., and Menon, S. Numerical modeling of turbulent premixed flames in the thin-reaction-zone regime. *Combustion Science and Technology 160* (2000), 119–150.

[66] Kobayashi, H., Seyama, K., Hagiwara, H., and Ogami, Y. Burning velocity correlation of methane/air turbulent premixed flames at high pressure and high temperature. *Proceedings of the Combustion Institute 30* (2005), 827–834.

[67] Kolla, H., Rogerson, J. W., Chakraborty, N., and Swaminathan, N. Scalar dissipation rate modeling and its validation. *Combustion Science and Technology 181* (2009), 518–535.

[68] Kolmogorov, A. N. The local structure of turbulence in incompressible viscous fluid for very large Reynolds numbers. *Proceedings of the Royal Society of London 434* (1991), 9–13.

[69] Krisman, A., Tang, J. C. K., Hawkes, E. R., Lignell, D. O., and Chen, J. H. A DNS evaluation of mixing models for transported PDF modelling of turbulent nonpremixed flames. *Combustion and Flame 161* (2014), 2085–2106.

[70] Lantz, A., Collin, R., Aldén, M., Lindholm, A., Larfeldt, J., and Lörstad, D. Investigation of hydrogen enriched natural gas flames in a SGT700/800 burner using OH PLIF and chemiluminescence imaging. *Journal of Engineering and Gas Turbines Power 137* (2015), 031505–031505–8.

[71] Launder, B. E., Reece, G. J., and Rodi, W. Progress in the development of a Reynolds-stress turbulent closure. *Journal of Fluid Mechanics 68* (1975), 537–566.

[72] Lecocq, G., Richard, S., Colin, O., and Vervisch, L. Gradient and counter-gradient modeling in premixed flames: theoretical study and application to the LES od a lean premixed turbulent swirl-burner. *Combustion Science and Technology 2010* (2010), 465–479.

[73] Lee, J., Lee, G. G., and Huh, K. Y. Asymptotic expression for turbulent burning velocity at the leading edge of a premixed flame brush and their validation by published measurement data. *Physics of Fluids 26* (2014), 1–19.

[74] Lindstedt, R. P., and Váos, E. M. Modeling of premixed turbulent flames with second moment methods. *Combustion and Flame 116* (1999), 461–485.

[75] Lipatnikov, A. N., and Chomaik, J. Molecular transport effects on turbulent flame propagation and structure. *Progress in Energy and Combustion Science 31* (2005), 1–73.

[76] Lörstad, D., Lindholm, A., Barhagi, D., Bonaldo, A., Lantz, A., Collin, R., Aldén, M., Fedina, E., and Fureby, C. Measurements and LES of a SGT-800 burner in a combusion rig. In *GT2012-69936, ASME Turbo Expo* (2012).

[77] Lörstad, D., Lindholm, A., Fureby, C., Alin, N., Lantz, A., Collin, R., and Aldén, M. Experimental and LES investigation of a SGT-800 burner in a combustion rig. In *GT2010-22688, ASME Turbo Expo* (2010).

[78] Lu, L., and Pope, S. B. An improved algorithm for in situ adaptive tabulation. *Journal of Computational Physics 228* (2009), 361–386.

[79] Lucca-Negro, O., and O'Doherty, T. Vortex breakdown: a review. *Progress in Energy and Combustion Science 4* (2001), 431–481.

[80] Ma, T., Stein, O. T., Chakraborty, N., and Kempf, A. M. A posteriori testing of algebraic flame surface density models for LES. *Combustion Theory and Modelling 17*, 3 (2013), 431–482.

[81] Maas, U., and Pope, S. B. Simplifying chemical kinetics: Intrinsic low-dimensional manifolds in composition space. *Combustion and Flame 88* (1992), 239–264.

[82] Magnussen, B. F. On the structure of turbulence and a generalised eddy dissipation concept for chemical reactions in turbulent flow. *in: 19th AIAA Sc. meeting, St Louis, USA* (1981).

[83] Menter, F. R. Zonal two-equation k-omega turbulence models for aerodynamis flows. *AIAA Paper* (1993). 93-2906.

[84] Menter, F. R. Two-equation eddy viscosity turbulence models for engineering applications. *AIAA Journal 32* (1994), 1598–1605.

[85] Menter, F. R., and Egorov, Y. A scale-adaptive simulation model using two-equation models. *AIAA Paper* (2005). 2005-1095.

[86] Menter, F. R., Kuntz, M., and Bender, R. A scale-adaptive simulation model for turbulent flow prediction. *AIAA Paper* (2003). 2003-0767.

[87] Moëll, D., Lörstad, D., and Bai, X.-S. Numerical and experimental investigations of the Siemens SGT-800 burner fitted to a water rig. In *GT2017-64129, ASME Turbo Expo* (2017).

[88] Mueller, C. M. *Numerische simulation instationaerer, turbulenter freistrahlduffusionsflammem mit dem flamelet-modell.* PhD thesis, Technische Hochschule Aachan, 1994.

[89] Mueller, C. M., Breitbach, H., and Peters, N. Partially premixed turbulent flame propagation in jet flames. *Proceedings of the Combustion Institute 25* (1994), 1099–1106.

[90] Muppala, S. P. R., Aluri, N. K., Dinkelacker, F., and Leipertz, A. Development of an algebraic reaction rate closure for the numerical calculation of turbulent premixed methane, ethylene, and propane/air flames for pressures up to 1.0 mpa. *Combustion and Flame 140* (2005), 257–266.

[91] Nilsen, V., and Kosály, G. Differential diffusion in turbulent reactive flows. *Combustion and Flame 117* (1999), 493–513.

[92] Nilsson, T., Carlsson, H., Yu, R., and Bai, X. S. Structures of turbulent premixed flames in the high Karlovitz number regime - DNS analysis. *Fuel 216* (2018), 627–638.

[93] Nogenmyr, K. J., Fureby, C., Bai, X. S., Petersson, P., Collin, R., and Linne, M. Large eddy simulation and laser diagnostic studies on a low swirl stratified premixed flame. *Combustion and Flame 156* (2009), 25–36.

[94] Nogenmyr, K. J., Petersson, P., Bai, X. S., Fureby, C., Collin, R., Lantz, A., Linne, M., and Aldén, M. Structure and stabilization mechanism of a stratified premixed low swirl flame. *Proceedings of the Combustion Institute 33* (2011), 1567–1574.

[95] Nogenmyr, K. J., Petersson, P., Bai, X. S., Nauert, A., Olofsson, J., Brackman, C., Seyfried, H., Zetterberg, J., Li, Z. S., Richter, M., Dreizler, A., Linne, M., and Aldén, M. Large eddy simulation and experiments of stratified lean premixed methane/air turbulent flames. *Proceedings of the Combustion Institute 31* (2007), 1467–1475.

[96] O'Connor, J., Acharya, V., and Lieuwen, T. Transverse combustion instabilities: Acoustic, fluid mechanic, and flame processes. *Progress in Energy and Combustion Science 49* (2015), 1–39.

[97] Persson, M. *Presumed and Transported PDF Methods Applied to Turbulent Premixed Flames*. PhD thesis, Imperial College London, 2011.

[98] Peters, N. *Turbulent Combustion*. Cambridge University Press, 2000.

[99] Pierce, C. D., and Moin, P. Progress-variable approach for large-eddy simulation of non-premixed turbulent combustion. *Journal of Fluid Mechanics 504* (2004), 73–97.

[100] Pitsch, H., and Duchamp, L. Large-eddy simulation of premixed turbulent combustion using a level-set approach. *Proceedings of the Combustion Institute 29* (2002), 2001–2008.

[101] Poinsot, T. Prediction and control of combustion instabilities in real engines. *Proceedings of the Combustion Institute 36* (2017), 1–28.

[102] Poinsot, T., and Vaynante, D. *Theoretical and numerical combustion*, 2 ed. R. T. Edwards Incorporated, 2005.

[103] Pope, S. B. Pdf methods for turbulent reactive flows. *Progress in Energy and Combustion Science 11* (1985), 119–192.

[104] Pope, S. B. On the relationship between stochastic lagrangian models of turbulencs and second-moment closure. *Physics of Fluids 6* (1994), 973–985.

[105] Pope, S. B. Computationally efficient implementation of combustion chemistry using in situ adaptive tabulation. *Combustion Theory and Modelling 1* (1997), 41–63.

[106] Pope, S. B. *Turbulent flows*. Cambridge University Press, 2000.

[107] Regele, J. D., Knudsen, E., Pitsch, H., and Blanquart, G. A two-equation model for non-unity lewis number differential diffusion in lean premixed laminar flames. *Combustion and Flame 160* (2013), 240–250.

[108] Richard, S., Colin, O., Vermorel, O., Benkenida, A., Angelberger, C., and Veynante, D. Towards large eddy simulation of combustion in spark ignition engines. *Proceedings of the Combustion Institute 31* (2007), 3059–3066.

[109] Rowinski, D. H., and Pope, S. B. PDF calculations of piloted premixed jet flames. *Combustion Theory and Modelling 15* (2011), 245–266.

[110] Sabelnikov, V., and Fureby, C. LES combustion modeling for high Re flames using multi-phase analogy. *Combustion and Flame 160* (2013), 83–96.

[111] Sadasivuni, S. K., Sanderson, V., Bonaldo, A., Bulat, G., and Swaminathan, N. Application of scalar dissipation rate modelling to industrial burner in partially premixed regions. *Proceedings of the European Combustion Meeting* (2011).

[112] Sankaran, V., and Menon, S. Subgrid combustion modeling of 3-D premixed flames in the thin-reaction-zone regime. *Proceedings of the Combustion Institute 30* (2005), 575–582.

[113] Sankaran, V., Porumbel, I., and Menon, S. Large eddy simulation of a single-cup gas-turbine combustor flows. In *AIAA 2003-5083, 39th Joint Propulsion Conference and Exhibit* (2003).

[114] Schmitt, F. G. About boussinesq's turbulent eddy viscosity hypothesis: historical remarks and a direct evaluation of its validity. *Comptes Rendus MÃľcanique 335* (2007), 617–627.

[115] See, Y. C., and Ihme, M. Large eddy simulation of a partially-premixed gas turbine model combustor. *Proceedings of the Combustion Institute 35* (2015), 1225–1234.

[116] Selle, L., Benoit, L., Nicoud, T. P. F., and Krebs, W. Joint use of compressible large-eddy simulation and Helmholtz solvers for the analysis of rotating modes in an industrial swirled burner. *Combustion and Flame 145* (2006), 194–205.

[117] Selle, L., Lartigue, G., Poinsot, T., Koch, R., Schildmacher, K. U., Krebs, W., Prade, B., Kaufmann, P., and Veynante, D. Compressible large eddy simulation of turbulent combustion in complex geometry on unstructured meshes. *Combustion and Flame 137* (2004), 489–505.

[118] Sheen, H. I., Chen, W. J., Jeng, S. Y., and Huang, T. L. Correlation of swirl number for a radial-type swirl generator. *Experimental Thermal and Fluid Science 12* (1996), 444–451.

[119] Skiba, A. W., Wabel, T. M., Carter, C. D., Hammack, S. D., Temme, J. E., Lee, T., and Driscoll, J. F. Reaction layer visualization: A comparison of two PLIF techniques and advantages of kHz-imaging. *Proceedings of the Combustion Institute 36* (2017), 4593–4601.

[120] Smagorinsky, J. General circulation experiments with the primitive equations, I. the basic experiment. *Monthly Weather Review 91* (1963), 99–164.

[121] Spalding, D. B. Mixing and chemical reaction in steady confined turbulent flames. *Proceedings of the Combustion Institute 13* (1971), 649–657.

[122] Spalding, D. B. Development of the Eddy-Break-Up model of turbulent combustion. *Proceedings of the Combustion Institute 16* (1976), 1657–1663.

[123] Speziale, C. G., Sarkar, S., and Gatski, T. B. Modelling the pressure-strain correlation of turbulence: an invariant dynamic systems approach. *Journal of Fluid Mechanics 227* (1991), 245–272.

[124] Staffelbach, G., Gicquel, L. Y. M., Boudier, G., and Poinsot, T. Large eddy simulation of self excited azimuthal modes in annular combustors. *Proceedings of the Combustion Institute 32* (2009), 2909–2916.

[125] Stockfelt, L., Andersson, E. M., Molnár, P., Rosengren, A., Wilhelmsen, L., Sallsten, G., and Barregard, L. Long term effects of residential NOx exposure on total and cause-specific mortality and incidence on myocardial infarction in a Swedish cohort. *Environmental Research 142* (2015), 197–206.

[126] Stöllinger, M., and Heinz, S. Evaluation of scalar mixing and time scale model in pfd simulation of a turbulent premixed flame. *Combustion and Flame 157* (2010), 1671–1685.

[127] Subramaniam, S., and Pope, S. B. A mixing model for turbulent reactive flows based on euclidean minimum spanning trees. *Combustion and Flame 115* (1998), 487–514.

[128] Subramaniam, S., and Pope, S. B. Comparison of mixing model performance for nonpremixed turbulent reactive flow. *Combustion and Flame 117* (1999), 732–754.

[129] Syred, N. A reviev of oscillation mechanisms and the role of the precessing vortex core (pvc) in swirl combustion systems. *Progress in Energy and Combustion Science 32* (2006), 93–161.

[130] U. S. Energy Information Administration. *Carbon Dioxide Emissions Coefficients*, 2016. `https://www.eia.gov/environment/emissions/co2_vol_mass.php`.

[131] Valiño, L. A field monte carlo formulation for calculating the probability density function of a single scalar in a turbulent flow. *Flow, Turbulence and Combustion 60* (1998), 157–172.

[132] van Oijen, J. A., and de Goey, L. P. H. Modelling of premixed laminar flames using flamelet-generated manifolds. *Combustion Science and Technology 161* (2000), 11–137.

[133] van Oijen, J. A., Donini, A., Bastiaans, R. J. M., ten Boonkkamp, J. H. M., and de Goey, L. P. H. State-of-the-art inpremixed combustion modeling using flamelet generated manifolds. *Progress in Energy and Combustion Science 57* (2016), 30–74.

[134] Venkateswaran, P., Marshall, A., Seitzman, J., and Lieuwen, T. Scaling turbulent flame speeds of negative Markstein length fuel blends using leading points concepts. *Combustion and Flame 162* (2015), 375–387.

[135] Venkateswaran, P., Marshall, A. D., Seitzman, J. M., and Lieuwen, T. C. Turbulent consumption speeds of high hydrogen content fuels from 1-20 atm. *Journal of Engineering for Gas Turbines and Power 136* (2014), 011504–1–011504–8.

[136] Veynante, D., Trouvé, A., Bray, K. N. C., and Mantel, T. Gradient and counter-gradient scalar transport in turbulent premixed flames. *Journal of Fluid Mechanics 332* (1997), 263–293.

[137] Wabel, T. M., Skiba, A. W., and Driscoll, J. F. Turbulent burning velocity measurements: Extended to extreme levels of turbulence. *Proceedings of the Combustion Institute 36* (2017), 1801–1808.

[138] Wabel, T. M., Skiba, A. W., Temme, J. E., and Driscoll, J. F. Measurements to determine the regimes of premixed flames in extreme turbulence. *Proceedings of the Combustion Institute 36* (2017), 1809–1816.

[139] Wang, H., Hawkes, E. R., Chen, J. H., Zhou, B., Li, Z., and Aldén, M. Direct numerical simulation of a high karlovitz number laboratory premixed jet flame - an analysis of flame stretch and flame thickening. *Journal of Fluid Mechanics 815* (2017), 511–536.

[140] Wang, H., Juddoo, M., Starner, S. H., Masri, A. R., and Pope, S. B. A novel transient jet flame for studying turbulent combustion. *Proceedings of the Combustion Institute 34* (2013), 1251–1259.

[141] Wang, J., Yu, S., Zhang, M., Jin, W., Huang, Z., Chen, S., and Kobayashi, H. Burning velocity and statistical flame front structure of turbulent premixed flames at high pressure up to 1.0 MPa. *Experimental Thermal and Fluid Science 68* (2015).

[142] Wang, P., and Bai, X. S. Large eddy simulation of turbulent premixed flames using level-set G-equation. *Proceedings of the Combustion Institute 30* (2005), 583–591.

[143] Warnatz, J., Maas, U., and Dibble, R. W. *Combustion - Physical and Chemical fundamentals, modeling and simulation, experiments, pollutant formulation*, 4 ed. Springer, 2006.

[144] Wilcox, D. C. Re-assessment of the scale-determining equation for advanced turbulence models. *AIAA Journal 11* (1988), 1299–1310.

[145] Zhou, B., Brackmann, C., Li, Q., Wang, Z., Petersson, P., Li, Z., Aldén, M., and Bai, X.-S. Distributed reactions in highly turbulent premixed methane/air flames Part i. Flame structure characterization. *Combustion and Flame 162* (2015), 2937–2953.

[146] Zhou, B., Brackmann, C., Li, Z., Aldén, M., and Bai, X.-S. Simultaneous multi-species and temperature visualization of premixed flames in the distributed reaction zone regime. *Proceedings of the Combustion Institute 35* (2015), 1409–1416.

[147] Zhou, B., Brackmann, C., Wang, Z., Li, Z., Richter, M., Aldén, M., and Bai, X.-S. Thin reaction zone and distributed reaction zone regimes in turbulent premixed methane/air flames: Scalar

distributions and correlations. *Combustion and Flame 175* (2017), 220–236.

[148] Zimont, W., Polifke, W., Bettelini, M., and Weisenstein, W. An efficient computational model for premixed turbulent combustion at high reynolds numbers based on a turbulent flame speed closure. In *International Gas Turbine & Aeroengine Congress & Exhibition* (1997).